UNIVERSITY OF SOUTHAMPTON
DEPARTMENT OF ELECTRONICS & COMPUTER SCIENCE

DIODE-PUMPED ACTIVE FIBRE DEVICES

by

IAN MICHAEL JAUNCEY

A Thesis Submitted for the Degree of
Doctor of Philosophy
February 1989

LIST OF CONTENTS

CHAPTER 1 : INTRODUCTION

CHAPTER 2 : DIODE LASERS AS PUMP SOURCES

CHAPTER 3 : FIBRE AMPLIFIERS

CHAPTER 4 : CW LASERS

CHAPTER 5 : Q-SWITCHING

CHAPTER 6 : GRATING DEVICES

CHAPTER 7 : CONCLUSIONS

List of References

List of Figures

Figures

UNIVERSITY OF SOUTHAMPTON

ABSTRACT

FACULTY OF ENGINEERING AND APPLIED SCIENCE
ELECTRONICS AND COMPUTER SCIENCE

Doctor of Philosophy

DIODE-PUMPED ACTIVE FIBRE DEVICES

by Ian Michael Jauncey

Single-mode optical fibres have made significant contributions to the growth in telecommunications and solid-state sensors and detectors. The development of methods for incorporating rare-earth elements into such fibres has stimulated considerable interest in producing novel active fibre devices.

This thesis reports the experimental and theoretical investigation of various diode-laser pumped active fibre devices.

Various schemes for launching pump energy from single strip diode-lasers into single-mode fibres are outlined and optimum launch configurations devised. A simple analytical theory of launch efficiency is presented.

The investigation of the characteristics of diode-laser pumped amplifiers and CW and Q-switched fibre lasers is described in detail. A number of new, efficient devices are reported, including diode-laser pumped fibre lasers operating at 935nm, 1088nm and 1560nm.

Existing analytical theories of active fibre behaviour are developed and the results compared to experimental measurements. It is found that approximations included in the theory are invalid and that agreement with experiment is poor. A computer based, numerical model is described which attempts to overcome some of the drawbacks of the analytical theory. The numerical model is shown to be highly successful in predicting active fibre device characteristics.

Finally, the use of fibre Bragg reflectors in fibre lasers and the construction of a number of useful narrow-linewidth fibre lasers are described, including a device operating on a single longitudinal mode. Novel techniques for rapidly fabricating very narrow-bandwidth fibre gratings are outlined and successful devices characterised.

ACKNOWLEDGEMENTS

I would like to gratefully acknowledge the contribution made by many members of the Optical Fibre Group in assisting the production of this thesis.

In particular I would like to thank Professor Alec Gambling for providing advice and encouragement and Dr David Payne for generating an innovative and stimulating atmosphere in which to work.

In the laboratory, Dr Bill Barnes, Mr Laurence Reekie and others have contributed greatly to the understanding of active fibre devices and have given support and help in many of the experiments. In addition, fabrication expertise has been provided by Dr Simon Poole, Miss Janet Townsend and other members of the Group.

I am indebted to Plessey Research Caswell Ltd for their constant financial and technical support during my studies and in particular to Mr D.C.J. Reid and Mr C. Rowe, without whom none of the fibre grating work would have been possible.

Finally, I owe a great deal to those who aided me in the production of this thesis, especially Miss Nicki Pink for her unfailing help. In addition, Mr Chris Nash and Mr Peter Harris have provided vital technical support.

LIST OF FIGURES

CHAPTER 1 : INTRODUCTION

1.1 Introduction

Optical fibres [1] have provided, in recent years, the main thrust of development not only in telecommunications but also in a wide range of sensor and detection applications. Single-mode fibres have been employed to transmit laser light over long distances, their mechanically flexible nature obviating the line-of-sight requirements of previous optical communications systems. If a fibre guide can also be made into a gain medium, a non-rigid fibre laser can be fabricated which is directly compatible with standard telecommunication fibres and devices. Further, if a cheap and compact pump scheme is employed, then a new class of useful devices can be constructed. The work presented in this thesis describes the fabrication and characterisation of various such active fibre devices.

The author certifies that the work described in this thesis is his own, except in the instances specifically stated in the text.

1.2 Background

Solid-state, rare-earth-doped lasers hosted in a glass matrix have been extensively investigated previously [2]. In a typical configuration, a rod of doped glass was optically pumped using, for instance, a flash lamp or high pressure arc lamp. In order to achieve population inversion high pump intensities and efficient optical coupling schemes were required [3]. The glass host afforded considerable flexibility in terms of the size and shape of the gain medium, but had a low thermal conductivity. As a result, the main drawback with previous devices was the containment of the thermal stress induced by the pump energy. One approach was to limit the cross-section of the glass rod [4]. In this device a multimode cladded glass fibre was employed. Further reduction of the thermal stress was achieved through a longitudinal pump arrangement and by ensuring a small pump beam spot size [5]. As a result laser action was obtained with a diode laser as the pump source [6].

The ultimate in reduction of guide cross-section produced a single-mode fibre. The development of a process for incorporation of various rare-earth dopants into single-mode fibres without compromising the low-loss transmission bands [7] led to the first demonstration of active single-mode fibre devices [8].

With single-mode fibres both the launched pump light and the signal light are confined to the active core region, thus realising an extremely efficient pump coupling scheme. Further, due to the reduced size of the core, typically a few microns across, the pump intensity is correspondingly high for relatively modest pump powers. Hence the total pump power required to reach population inversion is also relatively small when compared to bulk glass lasers. In addition, the reduced pumped volume ensures that the thermal stress problems which have plagued previous glass lasers are eliminated.

The incorporation of feedback in an active fibre with optical gain enables oscillation to be achieved, thus producing a laser. Optical feedback can be conveniently provided by butting the ends of the fibre to suitable mirrors or other fibre feedback devices. The reflectors do not have to be aligned with respect to each other, unlike other laser systems, as demonstrated in the first construction of a diode pumped single-mode fibre laser [8]. Also, ring configurations employing all-fibre optical splitters can be fabricated [9]. The flexible nature of the fibre guide allows the construction of some very long lasers. A 300m laser has already been demonstrated [9], and cavity lengths greater than of over 1km are possible. Such devices, with possible application as distributed sensors, are not feasible with other solid state technology.

With such techniques a number of novel lasers have been fabricated [10], including widely tunable fibre lasers [9], CW visible glass lasers [11] and lasers operating on transitions not previously reported in glass [12].

1.3 Fabrication of Rare-Earth-Doped Fibres

The fabrication techniques employed to produce high quality rare-earth-doped fibres have been described by others in detail elsewhere. Here brief summaries of the techniques are given.

1.3.1 MCVD

The modified MCVD technique [13,7] was the first to be developed and was closely aligned to the conventional MCVD process employed in telecoms fibre fabrication [14]. Preforms fabricated with the modified MCVD technique incorporated a dopant carrier chamber upstream of the main chamber. The dopant was introduced as the halide crystals (eg $NdCl_3.6H_2O$) into the chamber where it was dehydrated under a chlorine atmosphere and fused to the chamber wall, thus preventing downstream contamination. The inside of the deposition tube was then cleaned by gas-phase etching employing SF_6 and the cladding glass was deposited in the conventional manner. To introduce the dopant during core deposition, the secondary carrier was heated to 1000°C to produce small quantities of $NdCl_3$ vapour which was carried downstream. In the deposition chamber the vapour was oxidised to Nd_2O_3 in the hot zone and incorporated into the core. In order to achieve sufficient dehydration it was necessary to deposit the $NdCl_3$ unfused at a low temperature. The porous core layers could then be dried by heating in a chlorine atmosphere and were subsequently fused. The deposition tube was then collapsed to form a solid preform rod and pulled into a fibre in a conventional drawing tower.

The modified MCVD technique produced reproducible fibres, both in terms of refractive index profile and dopant concentration. However, the dopant concentration was limited to a few hundred parts per million (ppm).

1.3.2 Solution doping

In order to achieve higher dopant concentrations a modified technique, in which the dopant ions were deposited from a solution rather than from the vapour phase, was developed [15]. Firstly a conventional cladding was deposited (typically a $SiO_2/P_2O_5/F$ glass) and the core layers deposited at a reduced temperature, to form an unsintered porous soot. The preform was then filled at room temperature with an aqueous solution of the required dopant and left for periods up to 1 hour. After subsequent rinsing with acetone the perform was then dried and fused as for the MCVD process.

The solution doping technique enabled dopant concentrations up to a few thousand ppm to be achieved. In addition co-doping (such as Yb and Er to provide additional pump bands) could be accomplished. However, it was found that at high dopant concentrations significant clustering of the dopant ions occurred [16]. This caused fast cross-relaxations between the excited ions and thus reduced the available gain.

1.3.3 Fibres co-doped with Al_2O_3

The addition of a Al_2O_3 co-dopant was found to be an effective means of reducing the clustering in rare-earth doped fibres. In the fabrication technique [17,18], the solution doping method described above was followed. However an aqueous solution of $AlCl_3$ to allow co-doping with the rare-earth ion was employed. It was found that rinsing with acetone also removed the $AlCl_3$ and so dehydration in an O_2/Cl_2 flow prior to the normal gas phase drying was employed.

In addition, P_2O_5 was incorporated into the unfused core layers to enable high alumina concentrations to be achieved.

The alumina codoping method enable fibres containing up to 2% rare-earth dopant levels to be fabricated with no evidence of clustering.

1.4 Ionic Transitions

The transmission characteristics of single-mode fibres fabricated by the above processes are radically affected by the incorporation of the rare-earth dopants. A typical spectral attenuation plot for an Nd^{3+}-doped fibre, as shown in Figure 1, reveals bands of extremely high loss caused by electronic excitation of the dopant ions. The transmission at other wavelengths is not greatly compromised and this feature has been exploited in fibre filters. Figure 2 shows the energy levels in the Nd^{3+}-ion, with excitation and fluorescence transitions marked. The decay times of the energy levels are short, caused by phonon induced non-radiative relaxations. However, some levels are metastable and relaxation usually involves a slower photon decay. In Nd^{3+} such a metastable is the ${}^4F_{3/2}$ level and the fluorescence transitions from this level are those shown in Figure 2. Since the absorption bands are caused by excitations from the ground state, the wavelength of any de-excitation fluorescence which does not involve decay to the ground state is usually within one of the low-loss windows. The fluorescence spectrum for Nd^{3+}-ions in GeO_2/silica, Figure 3, shows that at the longer fluorescence wavelengths the fibre represents as low-loss guide.

Figures 4 and 5 show the absorption and fluorescence spectra respectively for Er^{3+}-doped germania/silica fibres. For Er^{3+} the metastable is also the first excited level and so the fluorescence is centred on an absorption band. However, if the ground state population can be depleted by over 50% then gain on this transition is possible. A similar situation occurs for the ${}^4F_{3/2}$-${}^4I_{9/2}$ transition in Nd^{3+}.

Exciting the dopant ions by launching light into the fibre at one of the absorption wavelengths and employing a signal at one of the fluorescence wavelengths enables optical gain to be achieved. This optical amplification was previously demonstrated in a multimode fibre with a pulsed flashlamp pump [19]. As explained above, CW pumping of single-mode doped fibres enables high gain CW amplifiers to be constructed [20].

The absorption and fluorescence bands show considerable broadening due to both homogeneous and inhomogeneous processes [21]. In the former, each ion is broadened by the same amount, and the ions are thus indistinguishable. In inhomogeneous broadening, each ion experiences different environments and the ensemble of ions produces a broad transition linewidth. In glass the pseudo random nature of the glass host entails that each dopant ion experiences different crystal fields and so the inhomogeneous contribution is significant. In addition, the glass host removes some of the degeneracy in the energy levels causing Stark splitting of some of the levels. This also broadens the transition and, combined with the homogeneous and inhomogeneous broadening, produces wide absorption and fluorescence bands [22].

1.5 Synopsis

The objective of the work described in this thesis was to further investigate, characterise and develop active rare-earth doped single-mode fibre devices. In addition, pursuit of optimum performance, coupled with convenient diode laser pumping was emphasised.

A number of notable results have been achieved; for example efficient diode laser pumped CW operation on a number of wavelengths [23,24] including 1.55μm [25]. Q-switching has produced sources capable of emitting over 100W peak power pulses [26] while the combination of fibre grating and active fibre techniques has produced extremely narrow linewidth lasers [27,28,29] suitable for WDM and coherent applications.

Alongside the experimental work a numerical model was developed which attempted to address some of the drawbacks of previous analytical approaches. The results of the model indicated the presence of gain saturation features and successfully predicted the noise spikes subsequently observed within Q-switched pulses.

CHAPTER 2 : DIODE LASERS AS PUMP SOURCES

2.1 Introduction

Previous fibre lasers have, for the most part, relied on conventional ion, or dye lasers to provide the pump energy, whilst for practical applications it is desirable to employ more convenient sources. Semiconductor diode lasers are cheap, reliable and easy to operate. Their small size renders them suitable for incorporation in compact devices. The success of miniature diode pumped crystal lasers [30] provides ample evidence for the desirability of employing diode lasers. Effort in this field has concentrated on fabrication of high power phased array diodes for pumping bulk crystals. For single-mode fibres it is necessary to employ single stripe diode lasers. The maximum power currently available from such device is limited to 40mW. Hence it is necessary to launch the pump light into the single-mode fibre with the utmost efficiency.

2.2 Electrical

In order for the dopant ions to absorb pump energy it is necessary that the pump wavelength coincides with one of the absorption bands of the dopant ion, shown in Figures 1 and 4. High-power CW diode lasers are currently available with a relatively small range of wavelengths and diode laser pumping has so far been limited to the GaAlAs diode laser range at approximately 810nm. As described in Section 1.4 the broad absorption widths compared to a crystal host relaxes the tolerance on diode laser wavelength. In miniature crystal lasers the pump diodes are mounted on temperature controlled surfaces to tune the output wavelength and increase diode life. The maximum output power of a typical diode laser is limited by the internal optical power. Excessive power causes catastrophic damage at the output facet. However, operation at a reduced temperature slows defect migration and increases life expectancy. Further, due to other competing processes, such as excited state absorption of the pump energy, tuning of the diode output wavelength to within 1nm was desirable. Consequently, temperature control of the diode lasers was investigated. An electronic temperature control circuit was devised and constructed. The circuit was able to maintain diode laser temperature to within 0.5°C.

Due to the limited output power available, it was often necessary to operate the diode-lasers close to the catastrophic damage threshold. Unfortunately the diode lasers were extremely sensitive to supply spikes. They had a large response bandwidth and were thus vulnerable to supply interference, particularly when operated close to the CW limit. It was found that no suitable drive circuits were commercially available. To overcome the drawbacks of the commercial drivers an alternative circuit was devised and developed. The circuit was completely isolated from the mains, with the power provided by a 10Ah 12V battery. With a driver current consumption of 100-250mA a charged battery operated the circuit for up to 40 hours. The battery could then be disconnected from the driver before connection to a mains powered recharger. The switch provided shorting of the diode supply pins when not in operation and a slow start feature prevented transients reaching the diode during switch on. The driver operated the diode on "current" mode.

2.3 Theory of Launch Efficiency

The initial design for the optical launch system, Figure 6, was similar to that employed for the first diode laser pumped fibre laser experiments. An approximate theoretical value for the launch efficiency of the system can be calculated by assuming that the input mode has a circularly symmetric Gaussian profile incident on the fibre core. If the lenses were chosen to match the numerical apertures (N.A.'s) of the diode laser and fibre, the launch efficiency can be taken as the overlap of the pump spot and the fibre mode. Obviously the analysis is only valid for a fibre which is single-mode at the pump wavelength.

The fibre launch lens was typically a X10 objective, with an N.A. of 0.25 to match that of the doped fibres.

The diffraction limited spot size can be calculated from

$$r_o = \frac{\lambda f}{\pi R} \tag{2.3.1}$$

r_o = field 1/e point radius
λ = pump wavelength
$f/2R$ = f - number of launch lens

For λ = 826nm and $f/R = 3.87$ then $r_o = 1.02\mu m$. A single-mode fibre with Gaussian index profile has a spot size given by

$$w_o = \frac{\rho}{\sqrt{(V-1)}} \tag{2.3.2}$$

w_o = field 1/e point radius
ρ = index profile radius
V = V-value of fibre at pump wavelength

For a typical fibre (type 490-04, Table 1) Equation 2.3.2 gives $w_o \approx 1.11\mu m$ at 826nm. As both spot profiles are circularly-symmetric the overlap integral can now be calculated:

$$\eta = \frac{\int_0^\infty \exp - (r/r_0)^2 \ \exp - (r/\omega_0)^2 \, dr}{\int_0^\infty \left[\exp - (r/r_0)^2\right]^2 dr} \qquad (2.3.3)$$

η = theoretical launch efficiency

Employing the definitive integral

$$\int_0^\infty e^{-ax^2} dx = \frac{1}{2} \sqrt{\left(\frac{\pi}{a}\right)}$$

allows (2.3.3) to be evaluated:

$$\eta = \sqrt{2} \, \frac{\omega_0}{(r_0^2 + \omega_0^2)^{\frac{1}{2}}} \qquad (2.3.4)$$

It can be seen that if $\omega_0 = r_0$ then the efficiency tends to 1 as expected. Similarly if $r_0 \rightarrow \infty$ then the efficiency tends to zero.

The experimental launch efficiency for a range of fibres with different cutoff wavelengths but the same N.A. was investigated with the apparatus shown in Figure 6. The results are shown in Figure 7, together with the theoretical plots for the estimated pump spot size and for an infinite spot size. It can be seen that the agreement was poor. A range of lenses revealed different launch efficiencies which appeared more dependent on the quality of the lens than its bulk characteristics such as

N.A. The reason for this was probably phase front distortion of the pump beam. It was considered that particle scatter and wider phase front distortion reduced the launch efficiency. Also it was found that different diode lasers required different lenses for optimal coupling.

2.4 Experimental Launch Efficiency

In order to characterise experimental launch efficiencies a number of diode lasers, optical launch systems and fibres were employed. It was found that the optimum launch systems and efficiencies were strongly dependent on the particular diode lasers used in the experiments.

The largest launch efficiency was measured to be 52%, achieved with a Sony SLD204V diode laser and a Newport FL40 collecting lens and a Nikon X10 microscope objective launch lens as shown in Figure 6. Some Sony diode lasers (such as the SLD202V devices) proved to have highly astigmatic output beams. For these devices a cylindrical lens was introduced as shown in Figure 8. Note that if the beam was collimated an extremely weak cylindrical lens would be required. However, by placing the lens slightly offset from the beam focus, a more conventional lens could be employed. The measured launch efficiency for this configuration was 43% . Sharp LT015MD diode lasers were found to have less astigmatic but more elliptical output beams. For these devices the launch system incorporated an anamorphic prism pair to compensate for the beam ellipticity, as shown in Figure 9. The launch efficiency was measured to be 42%.

It was found that any extra optical components introduced into the launch system possessed significant insertion loss, despite the precision optical AR coated specifications. Thus, the Sony SLD204V diode lasers, with an elliptical and astigmatic output beam, had the largest launch efficiency without any compensating elements.

One of the characteristics of an efficient launch system was the presence of optical feedback from the active fibre into the diode laser. The feedback often resulted in an instability of the diode laser output, a drop in threshold current and possible change in diode laser wavelength. Figure 10 shows the diode laser output spectrum in free space and in an optical launch system. Careful note of any change in threshold and wavelength of operation reduced the need for optical isolation. In experiments where pump stability was important, such as measurement of launch efficiency, a quarter-wave plate and analyser was included. Inevitably these elements reduced the launch efficiency and were not employed unless necessary. It should be noted that feedback into the diode or dye pump laser was a recurrent problem and, unless great care was taken, under-estimation the actual pump power launched was possible, leading to a larger than normal slope efficiency.

For applications requiring the largest pump power it was possible to employ two diode lasers, mounted with orthogonal polarisation, as shown in Figure 11. Although the launch efficiency of each diode laser was reduced, this configuration was able to launch most power (over 25mW) into a typical doped fibre.

2.5 **Summary**

The motivation for employing diode lasers as optical pump sources has been outlined. A simple analytical theory of expected launch efficiency has been presented but the results only gave poor agreement with experimental results. Extensive work revealed that high launch efficiencies, greater than 50%, are achievable from single-stripe diode lasers into single-mode fibres. It was found that the optimum launch system and efficiency were strongly dependent on the particular diode laser employed. In addition, the presence of optical feedback into the diode laser was found to induce considerable variations in laser performance.

CHAPTER 3 : AMPLIFIERS

3.1 Introduction

In line with the growing interest in many optical systems, there is increasing emphasis in direct optical amplification [31]. The prominent area of application is in telecommunications where ever increasing bit rates and systems requirements are pushing conventional microwave technology to the limit. In addition to this, high bandwidth photon preamplifiers are key elements in many low light intensity applications. Further, power amplifiers, both for telecoms and for sensor sources, are in great demand.

Long-haul telecommunications systems currently employ microwave repeaters with attendant reliability, power feeding and light-to-electricity-to-light conversion problems. In the field demonstration stage considerable success has been achieved with semiconductor diode amplifiers for use as repeaters [32]. Optically-pumped fibre amplifiers operating at 1.55μm [33] find direct application as source power amplifiers and detector preamplifiers. Fibre to fibre gains comparable to or larger than diode amplifiers and ease of direct splice compatibility make these fibre amplifiers attractive alternatives.

In addition, a wide bandwidth incoherent source, for instance an amplifier with an output composed entirely of spontaneous noise, would find immediate application as a convenient source for fibre ring gyros.

Further, there are an increasing number of sensor applications where the environmental ruggedness and inherent isolation properties of fibres are being exploited. In many of these applications the lengths of fibres employed are relatively short and so the wavelength of operation is not confined to the low-loss windows. Indeed, in applications where there may be many sensors minimum cost is the overriding factor. Consequently, there is considerable interest in devices operating, for instance, at 900nm, on the peak of silicon detector responsivity; at 1064nm due to the abundance of power diode pumped Nd:YAG sources and possibly at 1.3μm for local area network applications.

In each case there is a requirement to investigate the performance and characteristics of optical amplifiers.

3.2. Analytical Theory

In this section an analytical theory of the optical amplifier is presented. Much of the analysis follows the lines of previous work [34,35].

The conventional rate equations for a four-level system can be written as:

$$\frac{dN_1}{dt} = -\eta\ N_1\ \phi_p\ B_{14} + N_3\ B_{32}\ \phi_L + \frac{N_3}{\tau_{FL}}$$

$$\frac{dN_3}{dt} = \frac{-dN_1}{dt} \tag{3.2.1}$$

$$\frac{d\phi_p}{dt} = R - N_1\ \phi_p\ B_{14}\ \frac{h\nu_p}{vol}$$

$$\frac{d\phi_L}{dt} = N_3\ \phi_L\ B_{32}\ \frac{h\nu_L}{vol} - \frac{\phi_L}{\tau_c} + \frac{N_3}{\tau_{FL}}\ \frac{h\nu_L}{vol}$$

$$N_2 = N_4 = 0$$

$$N_T = N_1 + N_3$$

N = total ion populations in levels 1, 2, 3, 4
R = Pump rate
ϕ_p = Pump field energy density
ϕ_L = Signal field energy density
η = Fractional pump excitation efficiency
B = Einstein coefficients
τ_{FL} = Fluorescence decay time from level 3
$h\nu$ = Photon energy
τ_c = Cavity decay time
vol = Active volume

In multimode case population densities can be used:

$$\int_{vol} n(xyz)dv = N$$

and the total photon energy in mode

$$\int_{vol} \phi_j(xyz) = \Phi_j$$

Equations (3.2.1) become

$$\frac{dn_3}{dt} = \eta \sum_{i=1}^{M} \phi_{pi}\,(xyz)B_{14}\,n_1 - n_3 B_{32} \sum_{j=1}^{M} \phi_{Lj} - \frac{n_3}{\tau_{FL}}$$

$$\frac{d\Phi_{pj}}{dt} = R_j - B_{14}\,h\nu_p \int_{vol} n_1(xyz)\phi_{pj}\,dv \qquad (3.2.2)$$

$$\frac{d\Phi_{Lj}}{dt} = B_{32}h\nu_L \int_{vol} n_3(xyz)\phi_{Lj}(xyz)dv - \frac{\Phi_{Lj}}{\tau_c} + \frac{h\nu_L}{\tau_{FL}} \int n_3(xyz)dv$$

For the single-mode fibre Equations (3.2.2) become

$$\frac{dn_3}{dt} = \eta \varnothing_p B_{14} n_1 - n_3 B_{32} \varnothing_L - \frac{n_3}{\tau_{FL}}$$

$$\frac{d\Phi_p}{dt} = R_p - B_{14} h\nu_p \int_{vol} n_1 \varnothing_p dv \qquad (3.2.3)$$

$$\frac{d\Phi_L}{dt} = B_{32} h\nu_L \int_{vol} n_3 \varnothing_L dv - \frac{\Phi_L}{\tau_c} + \frac{h\nu_L}{\tau_{FL}} \int_{vol} n_3 dv$$

The attenuation of the single-mode fibre can now be evaluated from:

$$\alpha = \frac{1}{\Phi_p} \frac{d\Phi_p}{dz} = \frac{\mu}{c} \frac{d\Phi_p}{dt} \qquad (3.2.4)$$

and by dropping the R_p term as end pumping is assumed. From (3.2.3)

$$\frac{d\Phi_p}{dz} = \frac{\mu}{c} B_{14} h\nu_p \int_{vol} n_1 \varnothing_p dv \qquad (3.2.5)$$

In the single-mode case we can assume the Gaussian distribution and represent $\varnothing(xyz) = \varnothing(z) S(r)$ where $S(r)$ is the radial distribution function:

$$S(r) = \frac{e^{-(r/w_0)^2}}{\pi w_0^2} \qquad (3.2.6)$$

w_0 = field 1/e point radius

S(r) is normalised such that:

$$\int_0^\infty S(r) 2\pi dr = 1 \qquad (3.2.7)$$

Substituting (3.2.6) into (3.2.5):

$$\frac{d\Phi_p}{dz} = \frac{\mu B_{14} h\nu_p}{c} \int_{vol} \phi(z) n_1(r,z,\theta)\ S(r)\ 2\pi r\ dr\ dz \tag{3.2.8}$$

Assuming a rectangular "top hat" distribution of the dopant ions and negligible pump excitation

$$\begin{aligned} n_1(r,z,\theta) &= n_T & r &\leq a \\ &= 0 & r &> a \end{aligned}$$

enables the integral in (3.2.8) to be calculated:

$$\frac{d\Phi_p}{dz} = \frac{\mu B_{14} h\nu_p}{c} \quad \Phi(z) n_T \int_0^a e^{-r^2/\omega_o^2} \frac{2r}{\omega_o^2} dr$$

$$= \frac{\mu B_{14} h\nu_p}{c} \quad \Phi(z) n_T \left[1 - e^{-a^2/\omega_o^2} \right] \tag{3.2.9}$$

Substituting from (2.3.2) with ρ=a yields the attenuation coefficient, α:

$$\alpha = \frac{\mu B_{14} h\nu_p}{c} \quad n_T \left[1 - \exp(1 - V_p) \right] \tag{3.2.10}$$

$$\text{with } B = \frac{c\sigma_p}{\mu h\nu_p}$$

$$\alpha = \sigma_p \left[1 - \exp(1 - V_p) \right] \tag{3.2.11}$$

One of the predictions of the theory is the fractional pump power propagating in the core of the fibre. From (3.2.11)

$$\text{fractional power} = 1 - \exp(1 - V_p) \tag{3.2.12}$$

Since all the dopant is located in the core it can be expected that the attenuation changes as various parameters are altered. In practice the most accessible parameter is the pulling diameter and hence the fibre second-mode cutoff. The small signal attenuation of a fibre with various diameters has been measured and is shown in Figure 12. Also plotted are the analytical results and the computer model results developed in later sections. Note that as the fibre cutoff is reduced less power travels in the core and so the attenuation decreases. Agreement can be seen to be good. For V-values greater than 2.4 the fibre is multimode at the signal wavelength and so the Gaussian single mode approximation employed above breaks down. In the multimode regime, the mode distribution is greatly influenced by local stress, bend radius and so the attenuation becomes noisy and unpredictable. For heavily multimode fibres, however, the large number of modes confines almost all the light to the core and so the attenuation can once more be predicted

The concept of incomplete mode overlap in the core can be expressed in terms of an effective area or volume. In this approach the fraction of the mode power propagating in the core is found from (3.2.12)

$$[1 - \exp\ (1-V_p)] = \frac{A_{eff}}{A_o} = \frac{vol_{eff}}{vol_o} \qquad (3.2.13)$$

where $A_o = \pi a^2$

3.3 Breakdown of Analytical Model

Equations (3.2.3) can be written explicitly expressing the axial dependencies

$$\frac{dn(z)}{dt} = \eta\ \varnothing_p(z)\ B_{14}(n_T - n_3(z)) - n_3(z)\ B_{32}\ \varnothing_L - \frac{n_3(z)}{\tau_{FL}}$$

$$\frac{d\Phi_p(z)}{dt}\ R_p(z) - B_{14}\ h\nu_p \int_{vol} n_T - n_3(z))\varnothing_p(z)dv$$

(3.3.1)

$$\frac{d\Phi_L(z)}{dt} = B_{32}\, h\nu_p \int_{vol} n_3(z)\phi_L(z)dv - \frac{\Phi_L(z)}{\tau_c} + \frac{h\nu_L}{\tau_{FL}} \int_{vol} n_3(z)dv$$

Unfortunately Equations (3.3.1) cannot be solved analytically. Previous authors proceeded to reduce the problem by assuming that the population depletion of the ground state was small, as in Section 3.2. The axial pump field is then given by an exponential decay

$$\Phi(z) = \Phi_o\ (-\alpha z) \qquad (3.3.2)$$

where α can be evaluated from Equation (3.2.11)

The validity of the assumption in the case of a single-mode fibre can be estimated by calculating the approximate degree of conversion in a typical situation. Consider a fibre pumped at z=0 and assume that the signal field, ϕ_L, is negligible. From (3.3.1)

$$\eta\ \phi_p(0)\ B_{14}(n_T - n_3(0)) - \frac{n_3(0)}{\tau_{FL}} = 0 \qquad (3.3.3)$$

Thus

$$\frac{n_3(0)}{n_T - n_3(0)} = \eta\ \phi_p(0)\ B_{14}\ \tau_{FL} \qquad (3.3.4)$$

Now

$$\phi_p(0) \approx \frac{P_o \mu}{A_{eff}\ c} \qquad (3.3.5)$$

P_o = pump power launched = 2.5×10^{-2} W
μ = refractive index = 1.47
A_{eff} = effective core area ≈ 9×10^{-12} m^2
c = 3×10^8 ms^{-1}

Thus $\phi_p(0) = 13.6\ \mathrm{Jm^{-3}}$

Also

$$B_{14} = \frac{c\sigma_p}{h\nu_p\mu}$$

$c = 3 \times 10^8\ \mathrm{ms^{-1}}$
σ_p = pump cross section $\approx 1 \times 10^{-24}\ \mathrm{m^2}$
$h\nu_p$ = energy per pump photon $= 2.4 \times 10^{-19}$ J
μ = refractive index = 1.47

Thus $B_{14} = 850.3\ \mathrm{m^3\ s^{-1}\ J^{-1}}$

In addition $\eta \approx 0.52$ and $\tau_{FL} = 450 \times 10^{-6}$ s. Substituting these values into (3.3.4) yields

$$\frac{n_3(0)}{n_T - n_3(0)} = 2.7$$

Thus

$$\frac{n_3(0)}{n_T} = 0.73$$

Thus population depletion or pump saturation cannot be ignored. Previous workers have been unable to rigorously check the theory against experiment and so such approximations have remained.

Other approximations have occurred, for instance Snitzer's method [36] of calculating amplified spontaneous emission (A.S.E.) output power assumes zero pump saturation, as above, and zero signal (or gain) saturation.

To evaluate the steady-state small-signal gain analytically it is necessary to ignore the stimulated emission and pump saturation terms. Equations (3.3.1) can thus be rewritten, employing total ion populations and incorporating the concept of effective volume

$$\frac{dN_3(z)}{dz} = \eta\ \phi_p(z)\ B_{14}\ N_T - \frac{N_3(z)}{\tau_{FL}} = 0 \qquad (3.3.6)$$

$$\frac{d\phi_L(z)}{dt} = B_{32}\ \frac{h\nu_L}{vol_L}\ N_3(z)\ \phi_L(z)$$

Thus $N_3(z) = \tau_{FL}\ \eta\ \phi_p(z)\ B_{14}\ N_T$

From (3.2.4)

$$\frac{d\phi_L(z)}{dt} = \frac{\mu}{c}\ B_{32}\ \frac{h\nu_L}{vol_L}\ \tau_{FL}\ \eta\ \phi_p(z)\ B_{14}\ N_T\ \phi_L(z) \qquad (3.3.7)$$

Hence, incorporating Equation (3.3.2)

$$\int_{\phi_{Li}}^{\phi_{Lf}} \frac{d\phi_L(z)}{\phi_L(z)} = \frac{\mu}{c}\ B_{32}\ \frac{h\nu_L}{vol_L}\ \tau_{FL}\ \eta\ B_{14}\ N_T\ \phi_p(0) \int_{o}^{l} e^{-\alpha x}\ dx \qquad (3.3.8)$$

$$\therefore \ln \left\{\frac{\phi_{Lf}}{\phi_{Li}}\right\} = \frac{\mu}{c}\ B_{32}\ \frac{h\nu_L}{vol_L}\ \tau_{FL}\ \eta\ B_{14}\ N_T\ \frac{\phi_p(0)}{\alpha}\ [1-e^{-\alpha l}] \qquad (3.3.9)$$

Substituting from (3.2.10) and rearranging gives

$$\ln \left\{\frac{\phi_{Lf}}{\phi_{Li}}\right\} = \frac{P_o}{A_o}\ \frac{\eta\ \sigma_L\ \tau_{FL}}{h\nu_p}\ \frac{[1-\exp(1-V_L)]\ [1-e^{-\alpha l}]}{[1-\exp(1-V_p)]} \qquad (3.3.10)$$

Thus the small gain coefficient, γ, is given by

$$\gamma = \frac{\eta\ \sigma_L\ \tau_{FL}\ [1-\exp(1-V_L)]}{A_o\ \ h\nu_p\ \ [1-\exp(1-V_p)]} \qquad (3.3.11)$$

In order to provide a model which overcomes some of the difficulties outlined above, a more numerical approach was developed. Some motivation for this can be seen from Equation (3.3.1) which requires a numerical solution. It can be considered that the computing time required to provide the inversion was similar to the time required to compute a fully numerically model.

3.4. Introduction to Computer Model

In the previous section the motivation for developing a numerical model of active fibre optical amplification was outlined. It was considered that any model produced should be able to predict, with acceptable accuracy, fibre amplifier performance, provide insight into characteristics possibly not directly available by experimentation and be versatile, so that minor modification would be required to incorporate further active fibre configurations, such as CW or Q-switched lasers.

The basis for the model are the rate equations developed in Section 3.3 with some modification:

$$\frac{dN_1}{dt} = - \phi_p B_p N_1 \eta + \phi_{L+} B_L N_3 + \phi_{L-} B_L N_3 + \text{ratio} (\phi_{A+} B_A N_3 + \phi_{A-} B_A N_3) + \frac{N_3}{\tau_{FL}}$$

$$\frac{dN_3}{dt} = \frac{-dN_1}{dt} \qquad (3.4.1)$$

$$\frac{d\phi_p}{dt} = -\phi_p\ B_p\ N_1\ \frac{h\nu_p}{vol_p}$$

$$d\phi_{L\pm} = \phi_{L\pm}\ B_L\ N_3\ \frac{h\nu_L}{vol_L} + \frac{N_3}{\tau_{32sp}}\ \frac{h\nu_L}{vol_L}\ F_L$$

$$d\phi_{A\pm} = \phi_{A\pm}\ B_A\ N_3\ \frac{h\nu_L}{vol_L} + \frac{N_3}{\tau_{32sp}}\ \frac{h\nu_L}{vol_L}\ F_A$$

ϕ_p = Pump field energy density
ϕ_L = Signal field energy density
ϕ_A = Fluorescence field energy density
ϕ_+ = Propagating
ϕ_- = Counter propagating
B = Einstein coefficients = $c\sigma/\mu h\nu$
$h\nu$ = Photon energy
vol = Effective active volume of field
F = Spontaneous emission capture fraction
ratio = ratio of signal bandwith to total fluorescence bandwidth
τ_{FL} = Fluorescence decay time from level 3
τ_{32sp} = Spontaneous decay time from level 3 to level 2

The justification for the form of these Equations will now be described.

Both propagating and counter-propagating signal and fluorescence fields are explicitly included to allow analysis of propagating and counter-propagating signal and pump configurations.

Active devices in a glass host present particular problems over a crystal host as the pseudo-random nature of the glass host contributes to substantial inhomogeneous broadening. This is in addition to the substantial homogenous broadening caused by metastable lifetimes or phonon scatter. Unfortunately previous analysis of systems with both homogeneous and inhomogeneous contributions to linewidths is incomplete. The approach adopted by Yariv [37] and later Mears [35] is to divide the active ions into inhomogeneous classes labelled f, each with a homogeneous linewidth

$$\int g^f(\nu)d\nu = 1 \qquad (3.4.2)$$

Thus

$$g(\nu) = \int_0^\infty p(f)g^f(\nu)df \qquad (3.4.3)$$

where p(f) = probability ion is characterised by class f.

In a numerical analysis it was desirable to employ a cross section which could be directly included in equation,

We can define the total stimulated rate

$$\frac{dN_3}{dt} = N_3 \; W_T \qquad (3.4.4)$$

and

$$\frac{d\text{ø}_T}{dt} = N_3 \frac{h\nu_L}{vol_L} W_T$$

$$= N_3 \frac{h\nu_L}{vol_L} \; \text{ø}_T \; B_T \qquad (3.4.5)$$

ø_T = total field energy density

Now $B_T = \dfrac{c\sigma_T}{h\nu_L \; \mu}$ (3.4.6)

and $\dfrac{d\text{ø}_T}{dt} = \dfrac{d\text{ø}_T}{dz} \; \dfrac{c}{\mu}$ (3.4.7)

Thus, by substitution of (3.4.7) and (3.4.6) into (3.4.5)

$$\frac{d\phi_T}{dz} = \frac{N_3}{vol_L} \sigma_T \phi_T \tag{3.4.8}$$

Equation (3.4.8) defines the total effective cross section.

From Yariv [37] the stimulated rate $W_f(\nu)$ due to an energy density field $\phi(\nu)$ per unit frequency interval can be expressed as

$$W_f(\nu) = \frac{c^3}{8\pi \mu^3 h \tau_{sp}} \frac{\phi(\nu) g^f(\nu)}{\nu^3} \tag{3.4.9}$$

Hence

$$W_T = \frac{c^3}{8\pi \mu^3 h \tau_{sp}} \int\int \frac{\phi(\nu) p(f) g^f(\nu)}{\nu^3} dfd\nu \tag{3.4.10}$$

Equation (3.4.10) presents some difficulty as it is necessary to know the field energy spectral distribution and for that the total stimulated rate is required. Hence there is no direct analytical solution. Yariv [37] adopts the approximation that one type of broadening dominates.

From the literature we see that the inhomogeneous linewidth is typically twice the homogeneous linewidth [21]. The fluorescence spectrum (Figure 3) is wide. However, broadband fibre lasers reported previously operated with output spectra dependent on pump wavelength and linewidths of similar magnitude to the homogeneous linewidth. This indicates that coherent pumping is site selective and that the effective inhomogeneous contribution is reduced. This is further indicated by the efficiency of line narrowed fibre lasers (described in Section 6.5) compared to the broadband case. Hence the linewidths were treated as spatial hole burning of a homogeneous transition. We include a single field for the signal and a number of other fields which experience the same population inversion but do not contribute to the signal field. It must be noted that due to the complexity of the calculation the axial variations of the fields were not included. Hence the fields were not modelled to interfere with each other, in contrast to the true spatial hole burning case.

Instead, the fluorescence spectrum of Nd^{3+}-doped fibre at 1088nm (as shown in Figure 3) is modelled as a narrow signal field and a number of average spontaneous fields. We define a cross section for the signal field and one for the spontaneous field. We introduce the term "ratio" to indicate the ratio of the signal linewidth to the broadband linewidth.

Branching ratios are included as the various spontaneous decay times contribute to the fluorescent decay. The total fluorescent decay time is given by:

$$\frac{1}{\tau_{FL}} = \Sigma \frac{1}{\tau_{sp}} \tag{3.4.11}$$

For Equations (3.4.1) it must be remembered that the fields are the average energy densities across the active core region.

The capture fraction terms, F, represent the fraction of the spontaneous emission captured by the fibre.

Equations (3.4.1) are valid for a section of fibre, assuming small axial variation in field along the section length. To model the entire fibre many of the sections are concatenated, with each section passing on the pump and signal fields to the next. In this way the axial variations in fields were incorporated, with no explicit assumptions (such as exponential pump decay) included. Obviously it was necessary to choose a suitable section length such that the population change from one section to the next was small. Hence a typical fibre length was divided up into approximately 100 sections. The time taken for light to traverse each section was then the small dt in Equations (3.4.1). For ease of computation it was assumed that the fibre had zero dispersion.

Once the values of the parameters have been determined (described in the next section) the model assumes zero pump and signal fields with all ions in the ground state. The pump and signal were then introduced to one end of the fibre and the model run for the appropriate time. Both copropagating and counter propagating signal and spontaneous field were included.

The above model was programmed in both PASCAL and FORTRAN77. The PASCAL version provided easy graphics capability to enable the fields and populations along the fibre to be viewed while the FORTRAN version was considerably faster. A flow diagram for the program AMP3.F77 is shown in Figure 13.

3.5. <u>Determination of Values</u>

Dopant concentration

Levels of dopant concentration were based on data supplied by attenuation characteristics of multimode fibre, which were in turn based on the work of Smith and Cohen [38]. There was however some degree of uncertainty in accurately determining dopant level and so a well characterised fibre (type ND490) was chosen as as 'standard' fibre with a "best estimate" dopant level of 200ppm. The ionic density was calculated as follows:

per ppm, density of Nd $=2.218\mathrm{X}10^{22}$ m^{-3}.

Field energy density

The resultant field energy density for a given input field was calculated from:

$$\emptyset = \frac{\mu \, P}{A_{eff} \, c} \qquad (3.5.1)$$

where A_{eff} is the effective area of the core defined in Equation (3.2.13).

B coefficient

a) Absorption

The absorption coefficient was similar to that determined previously [38] and was taken as $9.5 \times 10^{-25}\mathrm{m}^2$ at 826nm. A spectral attenuation plot yielded the cross sections at various pump wavelengths. For 810nm pumping, as employed on some experiments, the cross-section was taken as $16.4 \times 10^{-25}\mathrm{m}^2$.

b) Emission

The stimulated cross section employed was, as outlined above, a peak cross section for the laser field and an integrated average cross-section for the spontaneous field. There has been much work presented previously on the determination of this cross-section, especially as a function of glass composition [39]. For GeO_2 glass the value is somewhat lower than the values given by Sarkies and a value of $12.5 \times 10^{-25}\mathrm{m}^2$ for the laser field and $6.4 \times 10^{-25}\mathrm{m}^2$ for the spontaneous field was chosen.

Fluorescent decay time

The fluorescent decay time was measured directly by rapidly removing the pump beam from a length of doped fibre and noting the decay of the fluorescence. The decay was not purely exponential, further indicating selective excitation and there has been determined a fast initial decay in some fibres due to clustering [17]. An average value of 450μs was chosen.

Spontaneous decay time

The value of the spontaneous decay time was determined from the fluorescence decay time by direct experiment. With reference to Figure 3 the branching ratio can be found by measuring the ratio of energy emitted into the transition bands and assuming a similar capture fraction for the bands. The experimental set up is shown in Figure 14; the diode laser pump enabled various pump wavelengths to be employed. Due to the three level nature of the $^4F_{3/2}$-$^4I_{9/2}$ transition there was some reabsorption of the fluorescence in this band. Hence the ratio of each of the bands was determined for different lengths and various pump powers. In addition, various fibres were measured to ensure that the values measured were a microscopic rather than a macroscopic function.

A typical output spectrum is similar to that shown in Figure 3. The area under each of the fluorescence band was measured and the branching ratio calculated from:

$$\text{Branching ratio 1:2:3} = \frac{\text{Area 1}}{h\nu 1} : \frac{\text{Area 2}}{h\nu 2} : \frac{\text{Area 3}}{h\nu 3}$$

The results for GeO_2 Nd gave spontaneous decay times of:

$^4F_{3/2} - ^4I_{9/2} = 804 \pm 70\mu s$
$^4F_{3/2} - ^4I_{11/2} = 1125 \pm 170\mu s$
$^4F_{3/2} - ^4I_{13/2} = 11250 \pm 510\mu s$

These were found to be independent of fibre and pump wavelength within experimental errors and broadly in line with those presented elsewhere [40]. For Al_2O_3 co-doped fibres the ratio might be expected to be different but unfortunately the highly-doped nature of the co-doped fibre made accurate determination by the above method impossible. From attempts to measure a fibre (type ND518) and from the literature [41] the values shown in Table 1 were chosen.

Capture fraction

As an initial estimate of the fraction of isotropically-scattered radiation capture by the core, the analytical formula developed for OTDR by Hartog [42] can be used:

$$F \approx \tfrac{1}{4}\left(\frac{NA}{\mu}\right)^2 \tag{3.5.2}$$

For doped fibres, however, the dopant was not uniformly distributed across the core and so some modification of the results was required. By measuring the A.S.E. (Section 3.6.1) it was possible to calculate a value of the capture fraction for the spontaneous field which was some 7.5 times larger than the OTDR value and might indicate non-isotropic radiation. Attempts were made to measure the radiation distribution resulting from a monochromatic narrow input beam but the results were inconclusive.

There still remained considerable degree of uncertainty in the values of some of the critical parameters. However, fine adjustment was possible by fitting a wide range of experimental data to the model and choosing the set of parameters which best fitted all of the results.

3.6 Results

Attenuation

The attenuation of various neodymium-doped fibres was determined using the multiple cutback method and employing an optically-isolated diode laser as the signal source. In addition a monitor photodiode was incorporated to ensure negligible diode laser wavelength and power drift.

In Figure 12 the small signal attenuation against V-value for fibre type ND499 are shown. Also plotted are the results for the computer model and the analytical values from Equation (3.2.11). The agreement between experiment and both theories is satisfactory. The analytical approach remains valid because the small signal conditions eliminate both pump saturation and stimulated emission. For V-values greater than 2.405 the fibre was double moded at the signal wavelength and hence the attenuation was strongly dependent on the local environment, bends and local stresses. In this region both theoretical models were invalid. However, subsequent experiments all employed fibre which was single mode at both the pump and signal wavelengths and so this loss of information is not important.

In Figure 15 the attenuation of fibre type ND540-05 at 810nm against pump power is plotted, together with the computer model and analytical results. It can be seen that pump saturation is an important consideration, even at diode laser pump powers. Indeed, for short fibre lasers (such as are employed for three-level or Q-switching experiments) there is significant residual pump at the far end of the fibre and optimisation of system design requires pump saturation effects to be included.

3.6.1. A.S.E. and Capture Fraction

With growing interest in ring fibre gyros there is an accompanying requirement for a stable short coherence length source with ability to launch greater than -20dBm of power into a single mode fibre. One possible source is an active fibre amplifier, but with no input signal and the output composed entirely of amplified spontaneous emission.

To determine the characteristics of the source and to provide data useful in fixing some of the fibre parameters required for the model the experimental configuration shown in Figure 16 was employed.

Spectral filtering of the ${}^4F_{3/2}$-${}^4I_{11/2}$ band emission was provided by a dielectric coated mirror. The emission detector was a pyroelectric NBS traceable instrument (Laser Precision type RS5900). This type of detector was selected as it was adequately sensitive, had a flat spectral response and presented negligible optical feedback. The fibre length was sufficient to absorb over 90% of the pump light, thereby maximising A.S.E. The collecting lens was specially manufactured for maximum transmission between 800 and 1300nm, with minimal chromatic aberration between these wavelengths. The transmission of this lens was determined in a separate experiment. As described in Section 1.4 above and shown in Figure 3, the emission bands merge into one another. The partition wavelengths were chosen at the emission minima at 1.00μm and 1.20μm. A small correction factor was included for the mirror characteristics over the ${}^4F_{3/2}$-${}^4I_{11/2}$ band. The amount of pump power launched was determined by the normal cutback method.

The A.S.E. outputs from a number of fibres were characterised in this way and the results for a fibre commonly employed (type ND490-04) is shown in Figure 17. Also shown are the results of the program AMP3.F77 for these cases incorporating the model parameters shown in Table 1. The agreement between experiment and theory is good for lower pump powers but the curves diverge at larger pump powers. The fall in A.S.E. measured is not understood but it is a feature encountered in other active fibre devices. Notice that the capture fraction used was some 7.5 times that of the Hartog OTDR type result. This has been discussed previously in Section 3.5.

3.6.2. Four-level Gain in Neodymium-doped Fibres

One of the most important parameters of any amplifier is the small signal gain. In terms of the analytical theory this was evaluated in Section 3.2

To determine the gain experimentally the configuration shown in Figure 18 was used. The source was an air cooled tungsten white light source launched copropagating with the pump beam. The pump launch optics were similar to those employed previously. The spectral content of the gain curve was investigated by employing a monochromator to filter the amplified output. Simulation of a narrowband source, by placing the monochromator between the white light source and the fibre, was attempted but the A.S.E. to signal ratio at the detector for the configuration was too great. As the wideband signal was small (a few μW) there was little signal depletion of the population inversion and so small-signal conditions were maintained. The pump power launched was determined by monitoring the residual pump and employing a cutback technique.

Two sets of experiments were performed. Firstly the gain spectrum was determined in order to locate the gain peak. A typical spectral gain plot is shown in Figure 19. All the GeO_2 Nd-doped fibres measured exhibited the gain peak at 1088nm. Secondly the gain at various pump powers for various fibres was determined at the 1088nm peak.

Due to the presence of considerable A.S.E. incident on the detector within the monochromator bandwidth, the system was sensitive to external acoustic noise. Attempts to reduce this noise, by isolating the white light cooling fan and eventually switching it off, were only partially successful. The problem was most pronounced for fibres with higher N.A's as the A.S.E. was increased. The experiments were repeated a number of times to reduce the random errors. It was considered that employing a source with greater output power would be beneficial. To this end an edge-emitting LED operating at 1070nm was employed. Unfortunately it was not possible to couple into the fibre more light in the 1088nm bandwidth than was available from the white-light source. A laser signal source at 1088nm was also considered and indeed Mears employed a fibre laser as the source. Unfortunately A.S.E. feedback from the pumped amplifier fibre into the source fibre laser resulted in a decrease in fibre laser gain and unreliable results. A line-narrowed fibre laser employing a grating as a spectral filter also did not produce satisfactory results. It is necessary to temporally isolate the source, such as a Q-switched laser pulsing into a delay line, to eliminate A.S.E. feedback. Unfortunately such sources are not presently readily tunable.

Results

The small-signal gain coefficient per mW absorbed, γ, was determined for a number of fibres and a number of pump wavelengths and is shown in Figure 20 against pump power for a typical fibre. Also plotted are the numerical model results for γ. In every experimental case γ decreased for increasing pump power, again indicating some gain saturation, as seen in Figure 17. The reason for such a rapid fall off is not known.

Cutoff

The estimated extrapolated γ at zero pump power for fibre ND499 is plotted in Figure 21 against cutoff wavelength. Also plotted are the corresponding values for the analytical theory and the numerical model AMP3.F77

γ incorporates the overlap of the pump, dopant and signal. As expected for small cutoff values the gain decreases as the field distribution spreads out more. However the theories predict a maximum gamma for a cutoff of approximately 770nm but this is not as observed experimentally. It must be noted however that the errors are considerable and further solid state analysis of the dopant distribution is required to make further progress.

NA

γ as function of NA is shown both experimentally and theoretically in Figure 22. It is apparent that the higher gains expected for higher NA fibres may be realised experimentally but at the cost of reduced launch efficiency.

Pump wavelength

γ as a function of pump wavelength is shown in Figure 23. It is notable that none of the theories include this feature. It has been determined that the fluorescence lifetime changes as the pump wavelength is altered around the 590nm [43] band but this does not appear to be the case for the 810nm pump band. The cause was probably selective ion excitation. Figure 23 provides useful data which can be incorporated into the model. Hence, altering the pump wavelength can lead to a modification of the small signal gain, possibly by reducing η.

Co-Propagating and Counter-Propagating

Experiments were performed at 1088nm for neodymium doped fibres for both co-propagating and counter-propagating signal and pump fields. The experiments produced identical results within errors measured. Both the analytical model and the numerical model produced identical results for the two cases.

3.6.3. Large Pulse Amplification

Diode-pumped miniature solid-state lasers are commanding an increasing share of the laser market and considerable effort is being expended in increasing output power. A diode pumped fibre amplifier might provide a reliable device to boost the output power for relatively modest (<50mW) pump power. The numerical model allows exploration of the expected performance of such a device.

As an example, the typical output expected from a Q-switched fibre laser or diode pumped Q-switched Nd:YAG laser was chosen. The input pulse was modelled as a triangular pulse of 10ns FWHM and varying peak power from 10mW to 10kW. The model was run for a single shot pulse. The active fibre was pumped with 20mW at 826nm and allowed to settle for 10ms so that the inversion stabilised. The gain and the A.S.E. at the end of the pulse were noted to indicate the final level of inversion and hence the degree of energy extraction. In addition, the total pulse energy gain was noted.

Results

In Figure 24 the results for input pulse peak powers up to 10kW are shown. It can be seen that the amplifier begins to saturate for pulses of peak power of only a few watts while the degree of energy extraction approaches unity for pulses of peak power greater than 1kW. In practice a number of fibre amplifiers could be easily cascaded and there is no reason why 100W Q-switched pulses presently available from a diode pumped fibre laser may not be amplified up to 1kW.

As the amplifier begins to saturate the trailing edge of the pulse experiences less gain than the leading edge and pulse distortion occurs. This can be seen in Figure 25 for a 10kW triangular input pulse. Such pulse distortion must be considered for any practical system.

3.6.4. Three-level Gain in Erbium-doped Fibres

As optical communication systems improve there is an ever-increasing demand for high bandwidth, efficient, optical repeater and amplifier devices. Previous work has concentrated on stimulated emission based devices such as semiconductor diode amplifiers [31] .

Active fibres offer a new type of stimulated emission device with direct splice compatibility and the possibility of high gains and large bandwidths [33]. Er^{3+}-doped fibre presents a particularly attractive device as the Er^{3+} stimulated emission spectrum is centred around the preferred 1.55μm telecoms band. Considerable work was performed on the Er^{3+}-doped fibre amplifier [33], but it was considered inappropriate to include the results in this thesis as the amplifier was not diode pumped. It has been demonstrated that pump wavelengths compatible with GaAlAs diode lasers are, however, possible [44].

Since initial work on the Er^{3+}-doped fibre amplifier was reported extensive work has been performed to further characterise the fibre and reduce some of the drawbacks [45]. Analysis of the expected amplifier performance has been carried out elsewhere [46]. Recent results [46] indicate the potential of the Er^{3+}-doped fibre amplifier as a viable telecommunications device.

3.7 **Summary**

Investigation of an analytical approach to the theoretical behaviour of fibre amplifiers has revealed that critical assumptions are invalid. In particular it was found necessary to include both pump saturation and spontaneous and stimulated emission terms. In order to produce a useful theoretical approach, a numerical computer model was constructed. This model successfully predicted a number of aspects of fibre amplifier behaviour and indicated the expected performance and characteristics of a large pulse fibre amplifier.

Experimental investigation of fibre amplifier behaviour was performed and a number of important characteristics measured. Agreement between experimental and numerical model results was found to be good, whereas the analytical model failed to produce satisfactory results.

CHAPTER 4 : CW LASERS

4.1 Introduction

One of the important driving forces behind development of active fibre devices is the realisation of a new class of laser sources. Due to the high pump intensities efficient CW lasers can be fabricated and laser action on transitions never previously obtainable in glass is possible [12]. Further the broad fluorescence linewidths enable widely tunable sold state lasers to be constructed [9]. In this chapter the development of CW lasers both experimentally and theoretically is described .

4.2 Analytical Theory

The threshold for laser action can be determined as the point at which overall gain exceeds overall loss. This can be expressed, employing the notation from Section 3.3, as

$$\left(\frac{\varnothing_{Lf}}{\varnothing_{Li}} \right)^2 . \text{ loss} = 1 \qquad (4.2.1)$$

The overall loss can be calculated from the inherent fibre losses and cavity loss at the lasing wavelength and the mirror reflectivities

$$\text{loss} = R_1R_2(1-L) \qquad (4.2.2)$$

R_1, R_2 = mirror reflectivities

L = sum of fibre and other cavity losses

Combining (4.2.1) and (4.2.2) yields

$$\left(\frac{\phi_{Lf}}{\phi_{Li}}\right)^2 R_1R_2(1-L) = 1 \qquad (4.2.3)$$

From (3.3.10)

$$\ln\left(\frac{\phi_{Lf}}{\phi_{Li}}\right) = P_o\,\gamma \qquad (4.2.4)$$

Substituting into (4.2.3) at threshold yields the power absorbed at threshold, P_{TH}

$$P_{TH} = \frac{-\ln[R_1R_2(1-L)]}{2\gamma} \qquad (4.2.5)$$

where γ can be evaluated from (3.3.11)

For mirror reflectivities close to 1 and small cavity losses, Equation (4.2.5) approximates to

$$P_{TH} = \frac{1-R_1R_2+L}{2\gamma} \qquad (4.2.6)$$

Above threshold, the slope efficiency is given by [35]:

$$\Delta = \frac{\eta\, h\nu_L \quad \ln[R_2]}{h\nu_P \quad \ln[R_1R_2(1-L)]} \qquad (4.2.7)$$

4.3 Development of Model to Include Lasing

The addition of positive feedback to an electronic amplifier results in oscillations if the loop gain exceeds the loop loss. Similarly in fibre lasers, optical feedback to an amplifier produces a laser oscillator. In the simulation model feedback at the fibre ends was incorporated to construct a fibre laser model. In the model the co-propagating energy density at the far end of the fibre becomes the counter-propagating energy density when multiplied by the appropriate mirror reflectivity and similarly for the near end of the fibre.

Once the pump was applied in the model it was necessary to allow it to run for sufficient time for the spontaneous decay to build up. However, once lasing action commenced, the lasing energy density build up grew rapidly, eventually overshooting the available inversion and leading to relaxation oscillations. Such relaxation oscillations are well know in experimental lasers [37]. Indeed, chopping of the pump beam and observation of relaxation oscillations was the method adopted to determine laser action in CW lasers. To obtain the steady state condition it was necessary to wait for these oscillations to decay. For experimental lasers, with decay times of the order of 10ms, the required waiting time was acceptable. However, it was found that the computing time required, even on the fastest transputer based computer available, was too long. It required a few hours of computing time to determine one lasing characteristic. Hence it was necessary to examine the model in order to reduce the computing time required.

To reduce the required computing time a decrease in the number of repetitive loops required to reach the CW steady state condition was necessary. An improvement was found by slowly ramping up the pump rather than by a discontinuous step. This gained a factor of two reduction in time. Further reduction of number of loops required an increase in the loop time. However, the loop time was determined by the speed of light traversing one segment, typically 50ps for a 2m fibre laser divided into 100 segments. Reduction in the number of segments was not possible as the population change across adjacent segments would have been too large, incurring errors. Instead, it was realised that, for CW lasers only (ie for systems with a steady-state output), a longer piece of fibre having the same total dopant level would produce an identical result. Hence a one kilometre fibre laser having the same total number of dopant ions would produce the same CW characteristics as a 1m fibre laser. This behaviour was modelled by including an "expansion" factor. In order to retain identical characteristics between the normal and expanded fibres, the total dopant must remain equal, hence the dopant concentration in the expanded case must be correspondingly less. As the pump and laser fields were in units of energy density no modification was required.

In this way, a typical 2m fibre laser could be expanded up to a 50km laser. This enabled the segement transit time to be increased to 1.25μs, in increase of some 25000. The limit on expansion was set by the requirement that the segment time was much smaller than the fastest rate involved in the equations.

The expansion scheme proved very successful and enabled a typical lasing characteristics to be plotted in minutes. As a test, the fast CW2.F77 program including expansion was run against the non-expanded version. Both produced identical results but with a computing time ratio of 20000. The flow chart for the CW2.F77 program is shown in Figure 26.

4.4 Experimental

In a manner similar to that described in the previous section, experimental construction of a fibre laser consisted of applying optical feedback to a pumped fibre amplifier. For convenience dielectric coated mirrors were employed to provide spectral feedback. These were readily available with a variety of reflectivities and could be manufactured to suit the individual application. Other methods of providing feedback have been demonstrated. These include fibre gratings, as discussed in chapter 6, fibre Sagnac reflectors, ring resonators [47] and dielectric layers directly coated on the fibre ends [48]. One of the advantages of employing bulk mirrors was the ability to construct a number of lasers a number of times with the same mirrors.

The experimental arrangement for a diode pumped CW fibre laser is shown in Figure 27. To form the Fabry Perot cavity the fibre was first stripped of its coating layer and then cleaved. The quality of the cleave was of paramount importance in determining the finesse of the cavity. The cleaves were always examined using an interference microscope. Cleaves with less than two interference fringes were acceptable. A number of cleaving techniques and commercial cleavers were employed and best results were obtained with the York type FK11 device. The cleaved fibre was then butted against the mirror at normal incidence. Force was applied along the fibre towards the mirror to keep the fibre in contact with the mirror. This was achieved by placing the fibre in a V-groove with two clamps, as shown in Figure 28. The clamp further from the butt firmly held the fibre while the other clamp retained the fibre in the groove, thus ensuring normal incidence, whilst allowing some axial movement. In this way the fibre could be brought against the mirror and then the groove brought slightly closer to bend the fibre between the clamps and retain pressure on the butt.

Marcuse has analysed the expected finesse of such fibre cavities [49] and concludes that angle and separation are important. Further analysis has revealed that for multilayer mirrors designed for use in a butted configuration can produce different reflectivities with only micron separation [50]. Hence, even after butting as above it was usually necessary to adjust the V-groove slightly to achieve maximum performance. Such adjustments are not available with other reflector types.

The butt loss has been measured by Morkel using a cavity ring down technique [51] and the results indicate only a small loss, some 5% per round trip. However variations across the spectral band could not be investigated using this technique. The frequency of relaxation oscillations has been suggested [52] but this process has a number of problems, as discussed in Section 4.5.

In order to investigate fibre laser performance a number of mirrors with graded reflectivities were obtained and the CW lasing characteristics plotted for each.

4.5 **Four-Level Results for Neodymium-doped Fibres**

A typical lasing characteristic obtained is shown in Figure 29. It can be seen to be composed of three regions:

(a) below threshold where the output was small,

(b) around threshold where the output increased rapidly and

(c) above threshold where a constant slope was obtained.

Region (a) Here the output consisted of A.S.E. with the gain less than the cavity losses. The output spectrum gradually narrowed from the fluorescence shape as stimulated gain increases.

Region (b) The spectrum narrows and relaxation oscillations were usually observed. This was the region around threshold where gain and loss were almost equal.

Region (c) The spectrum broadened due to hole burning, both spatial and spectral. The gain is saturated and remains clamped.

Also shown in Figure 29 are the plots from the analytical model and the numerical model CW2.F77. The agreement between the analytical plot and the numerical and experimental plots is poor. The laser characteristic was chosen as an example to illustrate the problem of defining a laser threshold for high gain systems. Analytical models for previous lasers have predicted behaviour more accurately, mainly due to the smaller capture fraction of spontaneous emission. In these systems the threshold was well defined as the A.S.E. contributed negligible output. Hence the intercept threshold (marked th2) and the threshold obtained from the onset of relaxation oscillations or spectral narrowing (marked th1) were concurrent. For fibre laser systems the problem is significant. Analytical theory predicts a threshold (Equation (4.2.5)) and for higher pump powers the gain is clamped. From experiment this is clearly not so. Laser threshold as defined by relaxations is predicted correctly but the intercept threshold, a more meaningful definition since slope efficiencies are calculated from it, is not. The numerical model explicitly includes the A.S.E. terms. However, it appears that as mentioned previously, the gain does become saturated at pump powers larger than expected. This characteristic is included in the model by defining a "saturation loss". The term represents, as a loss, the reduction in gain before true gain saturation is reached. This parameter was fitted for a number of GeO_2 Nd^{3+}-doped fibre laser characteristics and was always found to be 19% for the $^4F_{3/2}$ - $^4I_{11/2}$ transition.

Inclusion of "saturation loss" enabled both the numerical and analytical models to predict intercept thresholds for a fibre laser with a range of output reflectivities. Experimentally this was determined by measuring characteristics for each laser. The results, obtained in collaboration with Dr W.L. Barnes, are plotted in Figure 30. The agreement between the experimental and numerical model results must be considered excellent. It should be noted that no other published model has closely predicted actual fibre laser thresholds. The agreement between the analytical and experimental results is not so good, indicating a deficiency in the analytical theory.

Differential slope efficiency is defined as the differential output power divided by pump absorbed power. The experimental and theoretical results are shown in Figure 31. Here, the agreement between the analytical, numerical and experiemental reults is good, but the experimental fibre laser characteristics show decreased slope efficiency for output reflectivities less than 50%. This again was probably due to some further gain reduction effects not included in the model. It has been suggested that E.S.A. might be responsible. Previous work on Nd:YAG [53] suggested that the E.S.A. cross-section is less than 0.3 of the stimulated cross section. A version of CW2.F77 was run which included the E.S.A. term to evaluate its significance, but it failed to predict the slope efficiency roll off.

Further evidence for the inclusion of the "saturation loss" was found by analysing the relaxation oscillations discussed earlier. A simple analytical model [37] predicts relaxation oscillations giving relaxation oscillations of frequency:

$$f = \frac{1}{2\pi} \left\{ \frac{r-1}{\tau_C \ \tau_{FL}} \right\}^{\frac{1}{2}} \qquad (4.5.1)$$

r = pump power ratio above threshold

and oscillation decay time:

$$\tau = \frac{2\tau_{FL}}{r} \qquad (4.5.2)$$

Measurement of the relaxation oscillation frequency been suggested by Hanna [52] as a method of determining the cavity decay time and hence the intracavity loss and the quality of the butts. However, care was necessary to yield valid results. As described by Hanna, the analytical model is only valid for small relaxation oscillation amplitudes and is sensitive to any spectral shift in the diode laser output. Shown in Figure 32 are the relaxation oscillations of a particular fibre laser. In Figure 33 the oscillation frequency is plotted as a function of pump power above threshold. In this case the appropriate threshold is the relaxation oscillation threshold. The points all lie on a line in accordance with the analytical theory. However, the slope of the line corresponds to an intracavity loss of -4%+-2%. Also plotted are the results from the CW2R.F77 program. This was a slightly modified version of the CW2.F77 program, but not including the expansion factor as temporal results were required. The agreement is again good, even though the CW2R model includes a total intracavity loss of 24%. Using the numerical model it is possible to determine from the frequency to the intracavity loss. This technique was useful for determining the insertion loss of various intracavity components.

The frequency of oscillation was observed experimentally to change with relaxation number and this is shown in Figure 34. This was not predicted by the model and was possibly another characteristic of the gain saturation effect. Further, the decay rate of the oscillations is shown in Figure 35. Here the experimental data forms a line (which is independent of loss) in accordance with the analytical theory rather than the numerical model.

Optimum fibre laser design

Part of the motivation outlined above for detailed investigation of fibre laser behaviour was the determination of optimum fibre laser parameters. Experimentally this was limited to relatively few parameters, such as optimum output coupling, cutoff, NA. However, in many cases a change in the macroscopic parameter changed affected a number of other considerations, for example NA or cutoff affect launch power as well as fibre laser efficiency. However the model allows such parameters to be independently adjusted so that the influence of each can be assessed.

Output coupling

Figures 30 and 31 discussed above show the effect of the output mirror reflectivity on the lasing characteristic. As described above the numerical model and experimental results for slope efficiency diverge for lower reflectivity mirrors. Hence the most useful definition of optimum output coupling is one that produces the largest output power for a given pump power. This might not necessarily produce the largest slope efficiency. In Figure 36 the experimental and numerical model maximum output powers for 15mW launched power are plotted. The concept of optimum output coupling is clearly shown. Optimum output coupling is also discussed in Section 6.5.

Cutoff wavelength

Experimental determination of cutoff wavelength yielded an optimum of approximately 780nm (V-value = 1.72) for a variety of lasers. Figure 37 shows the lasing characteristics obtained from the numerical model with a range of cutoff wavelengths. It can be seen that a cutoff around 700nm was optimum. Figure 7 shows the launch efficiency against cutoff and when this was combined with fibre an optimum value around 750nm was obtained, close to the experimental value.

Eta and stimulated cross-section

The lasing characteristics for various excitation efficiencies and stimulated cross sections are shown in Figures 38 and 39. It is clear that attempts to increase these parameters, by altering the glass composition for instance, would be advantageous.

Decay times

Figure 40 show the lasing characteristics obtained for a range of fluorescence decay times. Once again, increases in the decay times are advantageous.

NA

One of the few differences between standard telecommunication fibres and active fibres is the increased numerical aperture usually chosen for active fibres. The effect of increase N.A. can be seen in Figure 41; higher N.A. fibres provided higher gain and larger output power. However, higher N.A. fibres exhibit lower launch efficiency and so a compromise was adopted. For applications requiring high gain, such as the three-level Er^{3+}-doped laser, a high NA fibre is required. For maximum power, from an Ar-ion laser pumped Nd^{3+}-doped fibre laser for example, a lower NA fibre was preferable.

Capture fraction

The capture fraction multiplier was discussed in section with reference to the A.S.E. output obtained. Figure 42 shows the region around threshold for various capture fraction multipliers. Examination of figure indicates that the value chosen yields a fibre laser characteristics similar to reality. It can be seen that a multiplier of 1, ie a purely Hartog [42] derived capture fraction, fails to produce a satisfactory curve.

4.6 Three-Level Results for Neodymium-doped Fibres

The fibre environment enables investigation of 3-level laser systems operating on a CW basis. The high pump intensities and small active volumes enable CW thresholds to be achieved and maintained. In this section we describe a diode laser pumped Nd^{3+}-doped fibre laser operating on the three-level $^4F_{3/2}-^4I_{9/2}$ transition and, in section 4.7, an Er^{3+}-doped fibre laser operating on the $^4I_{13/2}-^4I_{15/2}$ transition.

Numerical model

In a manner similar to that described above for the four-level model, a three-level amplifier model can be readily modified to include lasing action. The starting point is the three level rate equations:

$$\begin{aligned} dN_1 &= (\phi_{p+} + \phi_{p-})\, B_p\, N_1\, \eta + (\phi_{L+} + \phi_{L-})\, B_L\, (N_3 - N_1^*) \\ &\quad + \text{ratio}\, (\phi_{A+} + \phi_{A-})\, B_A\, (N_3 - N_1^*) + \frac{N_3}{\tau_{FL}} \end{aligned}$$

$$dN_3 = -dN_1$$

$$d\phi_{p+} = -\phi_{p+}\, B_p\, N_1\, \frac{h\nu_p}{vol_p} \tag{4.6.1}$$

$$d\phi_{L+} = \phi_{L+}\, B_L\, (N_3 - N_1^*)\, \frac{h\nu_L}{vol_L} + \frac{N_3}{\tau_{sp}}\, \frac{h\nu_L}{vol_L}\, F_L$$

$$d\phi_{A+} = \phi_{A+}\, B_A\, (N_3 - N_1^*)\, \frac{h\nu_L}{vol_L} + \frac{N_2}{\tau_{sp}}\, \frac{h\nu_L}{vol_L}\, F_A$$

$d\phi_{p-}$, $d\phi_{L-}$, $d\phi_{A-}$ similarly.

$N_1^* = N_1 \times \text{Boltz}$

where Boltz = thermal excitation factor i.e. fraction of ground-state population thermally excited to lower laser level.

Previous Work

To reach laser threshold in a three-level system it is necessary to saturate the absorption at the lasing wavelength. This was relatively straightforward to achieve in a single-mode fibre laser owing to the small mode size and the consequent high pump intensity obtainable with modest pump powers. Initial work on the three level transition in neodymium-doped fibre laser was centred on Rh6G pumped systems [54]. Miniature Nd:YAG lasers operating at 946nm have also been reported, pumped by either a Rh6G dye laser or an GaAlAs diode laser [55]. However, careful cavity design of the Nd:YAG was required to minimise intracavity losses and mode volume. In addition, it was found necessary to chop the pump beam to minimise any thermal effects which would lead to increased lower level population and hence higher threshold. The small guide volume and lack of thermal effects make these precautions unnecessary with single-mode fibre lasers.

Experimental

In order to maximise the fibre performance it was necessary to pump as close to the peak of the 810nm absorption band as possible. A Sharp LT016MD diode laser operating at 810nm was chosen. Even though this diode laser did not couple as much pump into the fibre as others diodes, operation at 810nm was assured. The fibre was type ND540-04, described in Table 1. The input mirror had a high transmission at the pump wavelength and a high reflectivity at the lasing wavelength. In addition, the input mirror reflectivity was low (R=3%) at 1.09μm to suppress build up of A.S.E. on the four-level transition. The output mirror had a reflectivity of 43% at the lasing wavelength.

Owing to the three-level nature of the transition it was necessary to avoid leaving an unsaturated absorbing region near the end of the fibre. Hence the fibre was cut back from an original length of 4.9m to determine the optimum length. At each length a lasing characteristic was measured. The optimum length for the maximum pump power available (8.36mW launched) was found to be 1.57m. The results for threshold, slope efficiency and maximum output power as a function of fibre length are shown in Figures 43, 44 and 45, respectively. Although characteristics were usually presented in terms of absorbed power, it was more illustrative in this case to employ launched power. The scatter of the experimental data points indicate the degree of repeatability obtainable from successive cleaves, even though great care was taken.

Also shown in Figures 43-45 are the results of the CW4.F77 program, using the data from Table 1. The agreement was less satisfactory than for the four-level transition, especially for the threshold prediction. However, the trends are similar and the prediction of optimum length (2.2m compared to an experimental result of 1.57m) was acceptable. It must be considered that only minor changes in the model originally set up for the four -level transition were required to predict the quasi three-performance.

Figure 46 shows the output wavelength as a function of length. The change in wavelength was due to the indistinct merging of the three-level transition at 904nm and the pseudo four-level transition at 950nm. This wavelength shift phenomenon is more fully explored in Section 4.7 with reference to the Erbium system.

One of the advantages of developing a computer based the model was the ability to extract useful information not available experimentally. This can be illustrated with reference to the 3-level fibre laser. A PASCAL version of CW4.F77 plotted the population levels and energy densities within a strictly 3-level laser. Figure 47 show three points in the laser characteristics. In part a) the area of absorption is greater than the area of gain and so the laser remains below threshold. At point b) the are of gain is greater than area of loss but not sufficient to overcome the 50% output mirror loss. In part c) the system is above threshold. The large laser field forces the populations almost equal. However, there remains an area of gain to overcome the cavity 50% loss. Such insights into fibre laser behaviour were useful in visualising population dynamics.

4.7 Three-level Results for Erbium-doped Fibres

Er^{3+}-doped fibre lasers and high-gain amplifiers operating within the important third window for telecommunications have already been demonstrated. However, these devices have all been pumped by ion or ion/dye lasers [56]. As shown in Figure 4, Er^{3+}-ions in glass have an absorption band around 808nm and can therefore be pumped by an GaAlAs diode laser. Dye laser pumping of an Er^{3+}-doped fibre laser at 807nm using a styryl 9 dye laser have already been reported [57]. In this section the first operation of a diode pumped Er^{3+}-doped fibre laser and its characteristics are described [23]. The assistance of Mr L. Reekie in performing this work is gratefully acknowledged.

In a manner similar to that described in section 4.6 for the $^4F_{3/2}$-$^4I_{9/2}$ transition in neodymium, for laser operation it is necessary to bleach out the inherent absorption at the lasing wavelength. The experimental configuration employed is shown in Figure 27, with a number of modifications. Due to the stringent pump wavelength requirement (808nm ±1nm) it was found that the only diode lasers available were 30mW devices with high astigmatism. Thus it was found necessary to employ the two diode polarisation multiplex scheme with cylindrical lenses to compensate for the astigmatism. The combined maximum power launched from both diodes was 26.8mW. The laser diodes were cooled to force operation at 808nm.

The input mirror had a transmission of 75% at the pump wavelength and a reflection of 99.8% over the lasing bandwidth, while the output mirror had a transmission of approximately 16% over the lasing range and a reflectivity of 30% at 808nm. In order to further increase the performance of the laser it would have been preferable to employ an output mirror which reflected more of the residual pump back into the fibre. However, no such mirror was available.

The doped fibre employed was type ND450 with characteristics shown in Table 1. It was fabricated using the solution doping technique outlined in Section 1.3.2

In order to determine the optimum pump wavelength a tunable styryl 9 dye laser was initially employed as the pump source. Figure 48 shows the variation in fibre laser threshold with pump wavelength. The requirement to pump at 808nm is demonstrated.

The laser characteristics obtained using diode lasers were measured using a Laser Precision RS 5900 calibrated power meter and a Bentham monochromator provided spectral information. A typical laser characteristic is shown in Figure 49. The intercept threshold was 4.37mW with a slope efficiency of 5.5%.

As described above for the three-level Nd^{3+}-doped fibre laser it was possible to determine the optimum length of doped fibre. If too long a length was employed an unsaturated lossy region at the far end of the fibre remained, while too short a length meant insufficient pump absorption. Hence, a long length of fibre was initially employed, a characteristic taken and then the fibre was gradually cut back with a characteristic plotted each time.

The results for threshold, slope efficiency and maximum output power against fibre length are shown in Figures 50, 51 and 52. The considerable scatter of the data points was due to a combination of cleave inconsistency and variable feedback into the diode lasers. As discussed before in section 2.4, optical feedback into the diode lasers was sufficient to disrupt their performance. It was not possible to place monitor photodiodes within the launch optics due to lack of space and the requirement to maximise the launch power. It is considered that it was pump wavelength shift which produced the scattering of the results. Optical isolators were not used in order to maximise input power.

It is interesting to examine Figure 51. It shows that the slope efficiency in terms of absorbed power decreases for shorter fibre lengths, when it might be expected to remain constant. The reason for this was excited state absorption (E.S.A.) of pump photons from the metastable upper laser level. Indeed the decay of the upper E.S.A. level produced photons of wavelength around 540nm and the strong green colour of the pumped fibre was obvious while the experiments were being performed. E.S.A. is a limiting influence on fibre laser and amplifier performance and much work has been recently reported to minimise this effect [58]. Unfortunately it appears that pumping at 808nm inevitably results in considerable E.S.A. and consequent degrading of performance.

Another aspect of the diode pumped Er^{3+}-doped fibre laser was the extended output wavelength range obtained by employing different fibre lengths [59]. Figure 53 shows the wavelength of operation of the above system against fibre length. Employing a dye laser as the pump source increased this range to 1650nm. The explanation for this wavelength shift lies in the quasi 3-level nature of the transition. At wavelengths around 1540nm the transition is pure three-level with lasing terminating on the ground state. However, at longer wavelengths, lasing terminates at a partially thermally populated level above the ground state and the laser therefore behaves as a quasi four-level system. Consequently the inherent loss of the fibre due to reabsorption at the lasing wavelength is decreased as the wavelength is increased. By employing a range of fibre lengths the relative significance of this effect compared to the other cavity losses can be adjusted. Thus for long cavity lengths the pure three-level transition remains unsaturated and so the lasing wavelength shifts towards the quasi four-level transition around 1.6μm. The lasing wavelength was found to be independent of pump power for powers up to four times above threshold.

The wavelength shift effect has also been observed on other three-level fibre laser systems, such as the $^4F_{3/2}$-$^4I_{9/2}$ Nd-doped fibre laser discussed in Section 4.6.

4.8 Tunable Fibre Lasers

The spectral dependance of the laser emission with glass composition has been investigated previously [60]. Dependance of the emission spectrum on pump wavelength has also been reported [61]. The conclusion drawn was that for certain wavelengths (802, 815 and 822nm) the average wavelength dependance vanished. However, as pointed out in the publication, external feedback has a strong influence on the output spectrum. In the next sections the effect of strong external feedback is examined.

Narrow linewidth fibre lasers

The broad fluorescence bandwidth shown in Figure 3 suggested that large fibre laser tuning ranges should be possible. With the incorporation of strong, spectrally dependant feedback into a fibre laser cavity, it has already been demonstrated that narrow linewidth and broadly tunable operation is possible [9]. Two diode pumped, Nd^{3+}-doped, broadly tunable fibre lasers are described in this section.

Tuning around 1088nm

The experimental arrangement for the tunable fibre laser is shown in Figure 54. Spectral feedback was provided by a bulk diffraction grating of 600 lines per mm and 1μm blaze. Rotation of the grating provided tuning of the fibre laser. A pellicle was employed to provide an output beam. A 3 metre length of fibre (type ND199-05) was employed. The threshold for laser action at the 1088nm peak was 2.8mW absorbed.

Figure 55 shows the output as the grating was adjusted, for an absorbed power of 15mW. The range of operation was continuous from 1062nm to 1154nm, a range of 92nm. This was the largest tuning range for a diode pumped fibre laser source reported. The maximum output power at 1088nm was 0.25mW. It should be noted that the tuning range compares favourably with the fluorescence spectrum shown in Figure 3.

The linewidth of the output was measured to be less than 30GHz. From the beam diameter at the grating and the grating characteristics the reflection bandwidth was estimated to be 200GHz, somewhat larger than the laser bandwidth. This indicates strong modal gain competition. The efficiency of the line-narrowed fibre laser was not substantially less than that of the broadband device, indicating significant homogeneous contribution to the transition.

Tuning around 935nm

A similar experimental arrangement to that described above and shown in Figure 54 was employed to achieve tunable operation around 925nm. The fibre used was type ND540-04. As previously, the fibre length was cut back to achieve optimum performance. For the particular configuration employed the optimum length was found to be 92cm. Threshold for laser operation at this length was 6.5mW absorbed. The tuning range of over 40nm is shown in Figure 56 for an absorbed pump power of 15mW. The tuning range was discontinuous, indicating Stark splitting of the ground state. As might be expected, the quasi-four-level transition around 935nm produced the greatest output, a maximum power of 0.2mW.

4.9. **Offset Core Fibre Laser**

One of the advatages miniature Nd:YAG lasers possess over fibre lasers is their ability to be pumped by powerful diode-laser arrays. Fibre lasers require a single stipe pump source and this has undoubtedly limited their performance. However, a technique has been presented which enabled a multstripe phased array to be used as a pump source [62].

The scheme involved fabrication of a special fibre with two cores. The first, doped core was surrounded by a secondary, multimode core. The multimode core supported modes launched by a multistripe source. As these modes travelled down the fibre the skew rays passed into the doped core and were thus absorbed. Less skew rays were absorbed further down the fibre. The technique required the fabriction of a highly doped primary core as the pump rays passed through the core at a skew angle rather than longitudinally, as in a single-mode fibre.

A demonstration has been reported where an offset core single mode fibre laser was pumped by a dye laser [62]. In this section the first operation of a diode pumped offset core fibre laser is presented.

The fibre employed was characterised by a primary NA of 0.2. The seconday cladding was silcone rubber coating, providng a large index difference. The Nd^{3+}-doped core was offset to increase coupling. The pump source employed was a Spectra-Physics SDL2420 200mW phased array, emitting at 813nm. The experimental arrangement was the double-butted arrangement as shown in Figure 27. Some diffculty was experienced in coupling in the highly elliptical pump light spot into the secondary core. It was discovered that a standard collecting objective and a 0.3 NA launch objective were optimum. In this way the launch efficiency was increased to approximately 30%. The exact measure is not known as a cutback was non linear due to preferential mode absorption.

The output mirror was 40% reflective at the lasing wavelength to maximise output power. Difficulty was experienced in achieving good cleaves. However, a length of 6 metres of fibre enabled the characteristic shown in Figure 57 to be obtained. The threshold was high due to large intra-cavity losses. Note the maximum output power of over 10mW. This was the largest output power yet achieved from a diode pumped single-mode fibre laser.

4.10 **Neodymium-doped Fibre Laser operating at 1.4μm**

The second low-loss telecoms window for silica is around 1.3μm, a transition readily available from Nd:YAG. Initial attempts to excite laser action in this transition in a fibre laser were unsuccessful. Work by Morkel [63] and others indicated strong E.S.A. on this transition. However, work at other laboratories has produced laser action on the long wavelength end of the transition at 1.4μm [64]. More recently work has concentrated on fluorozirconate glasses [65]. In this section lasing at 1.4μm in neodymium-doped silica/germania/alumina fibre is discussed.

The experimental arrangement was the double butted configuration shown in Figure 27, except that a styryl 9 dye laser operating 823nm and a X5 objective for the launch lens were employed. Both mirrors were high (R=99%) reflectors. The fibre was co-doped with alumina, type ND518, shown in Table 1. Laser action was observed at 1.394μm, in line with the wavelength seen by other workers, and at an estimated threshold of 6mW. Due to the high reflectivity of the output coupler, maximum output power was limited to 44μW.

4.11 **Thulium-doped Fibre Laser**

A number of rare-earth doped fibre laser systems with absorption bands compatible with diode laser pump sources have been proposed, amongst them holmium and thulium. Here, laser action from thulium doped fibre pumped around 800nm is described [66]. A considerable portion of this work was performed by the Department of Physics at Southampton University.

As can be seen from Figure 58, thulium has a strong absorption band around 800nm. Analysis has revealed a lifetime of approximately 200μs for the $^3H_4$ metastable.

The experimental configuration was as shown in Figure 27, except that a Styryl 9 dye laser was employed as the pump source. The fibre employed possessed characteristics as shown in Table 1. The $^3H_4$ - $^3H_6$ transition was inherently quasi three-level and it was found necessary to place most of the doped fibre in liquid nitrogen to depopulate the lower laser Stark levels. The optimum pump wavelength was found to be 797nm. Without nitrogen, optimum fibre performance was found to occur with 27cm of fibre. With an output coupler of 3% transmission, the output wavelength was measured to be 1.94μm , with a threshold of 30mW absorbed and an output slope efficiency of 13%.

In spite of considerable effort it was not possible to reduce the fibre laser threshold and attempts at diode laser pumping were unsuccessful. However, further fibre design and cavity optimisation might enable a diode pumped, Tm^{3+}-doped fibre laser to be constructed.

4.12 Summary

An analytical theory for CW fibre laser action has been developed but was found to be unable to predict experimental characteristics. Inconsistencies in the definition of laser threshold have been identified and resolved. By the inclusion of a "saturation loss" it has been demonstrated that the numerical model can predict, with considerable success, some aspects of CW fibre laser behaviour. The numerical theory has allowed evaluation of the influence of various microscopic and macroscopic parameters to be performed and has indicated possible optimum fibre designs.

Efficient diode laser pumped CW fibre lasers have been constructed operating at 1088nm, 935nm and 1600nm. In addition, fibre lasers operating at 1400nm and 1940nm have been described. Widely tunable CW lasers have been demonstrated and, by the development of an offset core fibre laser, the highest output power reported from a diode laser pumped single mode fibre laser has been described.

CHAPTER 5 : Q-SWITCHING

5.1 Introduction

Lasers capable of launching pulses of high peak power into a single-mode fibre find immediate applications in a wide variety of sensor and non-linear devices. Current sensor techniques employ LED's and diode lasers, but high peak powers are not yet available from these devices. Diode pumped miniature Nd:YAG lasers provide high peak power, but suffer launch limitations and are not widely tunable. Alternatively, diode pumped Q-switched fibre lasers offer a novel source of stable high power pulses.

High power, Q-switched fibre lasers have been demonstrated previously [9] and non linear effects investigated [35]. However, such sources were ion or ion/dye pumped with attendant limitations. In this chapter diode laser pumped Q-switched Nd^{3+}-doped fibre lasers operating at 925nm and 1088nm are described.

5.2 Analytical model and theory limitations

Analytical treatments of Q-switched operation of bulk lasers have been well documented [67,68,69] and many of the characteristics predicted and explained. Application to fibre lasers has been made by extrapolating results calculated for low mode order bulk crystal devices.

In this section an analytical theory for single shot Q-switched operation is presented.

In the analytical analyses presented by Koechner and by Gaeta, Digonnet and Shaw, initial equations were taken from Equations (3.2.2) with the assumption that both spontaneous emission and pumping can be neglected during the Q-switch pulse. Thus, during the Q-switched pulse,

$$\frac{dn_3(x,y,z,t)}{dt} = -n_3(x,y,z,t)\ B_{32}\ \phi_L\ (x,y,z,t) \qquad (5.2.1)$$

$$\frac{d\Phi_L(t)}{dt} = B_{32}\ h\nu_L \int_{vol} n_3(x,y,z,t)\phi_L(x,y,z,t)dv - \frac{\Phi_L(t)}{\tau_c}$$

To proceed further, Gaeta et al [69] were forced to make a number of assumptions. Firstly, the spatial dependence of the lasing field was assumed to be independent of time. Unfortunately, this assumption is not valid and direct experimental evidence of the breakdown of this approach is presented in Section 5.8. To accurately calculate the initial inversion before the Q-switch was activated, Equations (3.3.1) are the necessary starting equations as the stimulated emission and pump saturation terms are significant. It is unfortunate that Gaeta et al, who failed to include these terms, did not present any experimental data to assess their theory.

In spite of these difficulties it is instructive to pursue the bulk analytical approach developed by Koechner [67] and Carlson [68]. Equations (5.2.1) can be rewritten as

$$\frac{dn_3}{dt} = -n_3\ B_{32}\ \phi_L \qquad (5.2.2)$$

$$\frac{d\phi_L}{dt} = n_3\ B_{32}\ h\nu_L\ \phi_L - \frac{\phi_L}{\tau_c}$$

If the Q-switch acts instantaneously then

$$\text{For } t < 0 \quad \tau_c = 0$$

$$t \geq 0 \quad \tau_c = \tau_{passive} = \tau_p \tag{5.2.3}$$

From (5.2.2)

$$\frac{d\phi_L}{dn_3} = \frac{-n_3 B_{32} h\nu_L \phi_L + \phi_L/\tau_c}{n_3\ B_{32}\ \phi_L} = \frac{1}{n_3 B_{32} \tau_c} - h\nu_L \tag{5.2.4}$$

But in CW operation at threshold $\tau_c = \tau_p$ and $d\phi/dt = 0$. Thus

$$n_{3T} = \frac{1}{\tau_c\ B_{32}\ h\nu_L} \tag{5.2.5}$$

Hence

$$\frac{d\phi_L}{dn_3} = -h\nu_L \left\{ 1 - \frac{n_{3T}}{n_3} \right\} \tag{5.2.6}$$

Integration of (5.2.6) gives

$$\phi_L(t) - \phi_{Li} = -h\nu_L \left[n_3(t) - n_{3i} - n_{3T} \ln \left\{ \frac{n_3(t)}{n_{3i}} \right\} \right] \tag{5.2.7}$$

where n_{3i} is the inversion at $t = 0$.

At the peak of the Q-switched pulse $d\phi/dt = 0$ and thus $n_3(max) = n_{3T}$. Thus

$$\phi_L(max) = -h\nu_L \left[(n_{3T} - n_{3i}) - n_{3T} \ln \left\{ \frac{n_{3T}}{n_{3i}} \right\} \right] \tag{5.2.8}$$

If we take $\omega = n_{3i}/n_{3T}$ then Equation (5.2.8) equates to the expression (7) in Carlson. From (5.2.8) the peak power can be calculated from

$$\text{Peak Power, } P_{max} \approx \frac{\phi_L(\max)\ A_{eff}\ l}{\mu\ \tau_p} \qquad (5.2.9)$$

where A_{eff} = effective area
l = cavity length

An expression for the pulse width can be derived by further differentiation of Equations (5.2.2)

$$\frac{d^2\phi_L}{dt^2} = \frac{d\phi_L}{dt} n_3\ B_{32}\ h\nu_L + \frac{dn_3}{dt} B_{32}\ h\nu_L\ \phi_L - \frac{d\phi_L}{\tau_c dt} \qquad (5.2.10)$$

The inversion, n_3, can be eliminated, giving

$$\frac{d^2\phi_L}{dt^2} = \frac{\left(\frac{d\phi_L}{dt}\right)^2}{\phi_L} - \frac{\phi_L{}^2\ B_{32}}{\tau_c} - \phi_L \frac{d\phi_L}{dt} B_{32} \qquad (5.2.11)$$

If the last term on the right of Equation (5.2.11) is neglected then a solution is given by

$$\phi_L(t) = \frac{\phi_L(\max)}{\cosh^2\left[\left(\frac{\phi_L(\max)\ B_{32}}{\tau_c}\right)^{\frac{1}{2}}(t-t_o)\right]} \qquad (5.2.12)$$

Note there is a small typographical error in the similar expression (11) in Carlson's paper [68]. The pulse FWHM can be approximated from Equation (5.2.12) as

$$\Delta t_{FWHM} \approx \frac{1.76}{\left[\frac{B_{32}}{\tau_c} h\nu_L\ n_3 T\ (\omega-1-\ln\omega)\right]^{\frac{1}{2}}} \qquad (5.2.13)$$

where $\omega = \frac{n_{3i}}{n_{3T}}$ as before.

However, as discussed in Section 3.3, this approach has limited value. In order to retain all the terms which have significant influence on the required result a transcendental equation (Equation (3.3.1)) is involved. This requires numerical evaluation for each segment of the fibre, involving as many computations as a full numerical, model. For Q-switched fibre lasers, the initial field intensities are important, as the capture fraction for spontaneous emission is large compared to most bulk laser systems. The build up of the Q-switched pulse is usually calculated from noise [70], a process involving only order of magnitude agreement.

The analysis by Gaeta, Digonnet and Shaw [69] on Q-switched fibre lasers follows similar lines to that by the authors for CW operation. Again stimulated emissions and pump saturation are ignored and an exponential decay for the pump assumed. Further more, their analysis fails to predict the presence of significant spiking within the Q-switched pulse, a characteristic fully predicted by the numerical model and only recently observed.

5.3 **Numerical model**

Adaptation of the numerical model developed to predict amplifier and CW laser action to pulse operation was straightforward. The flow diagram for the model QSW2.F77 is shown in Figure 59.

As Q-switching is a temporal non-steady-state effect the technique of "expanding" the fibre length as described in the CW section was not directly applicable. However, during the inversion build up, prior to the evolution of the pulse, the system approximated to an equilibrium situation, in a manner similar to that for the amplifier model. Hence, the model "expanded" the fibre length during inversion build up in the low-Q state and then "contracted" again as the high-Q state began. The energy densities and total dopant levels for the normal and expanded situations were the same. Hence it was possible to obtain the energy densities and inversion values quickly with the "expanded" fibre and without the approximations employed in the analytical methods described earlier. All the significant terms, from equations 3.3.1, could be included and hence non valid assumptions were omitted.

During the evolution of the Q-switched pulse, the model operated on the "normal" fibre. In line with the approach chosen by others, the pump and spontaneous transitions can be neglected during this time. To evaluate the validity of this assumption the typical characteristic time for these processes can be used. For a "normal" fibre laser the pump excitation time was evaluated as 5μs. The characteristic time for the spontaneous decay was obviously the decay time, taken as 450μs. For the Q-switching region the relevant time was that for which the inversion was significantly less than the initial inversion. This could be taken as the FWHM, as only for high peak powers would the stimulated rate rapidly decay the inversion. In all cases this width was less than 1μs.

For analysis by the numerical model, the most uncertain parameters were those describing the intra-cavity modulator characteristics. The values chosen for diffraction efficiency and switching time were supplied from experimental evidence gathered by W.L. Barnes. The insertion loss of the modulator could not however be measured directly. Instead, a CW lasing characteristic of the laser in the high-Q state was taken. The CW2.F77 program was then employed to find the best fit intracavity loss. The results are shown in Figure 60. Also shown are the double butted CW characteristics (experimental and theoretical) for comparison. As can be seen, the agreement for the Q-switched arrangement was good for an intracavity loss of 45%. If the "saturation loss" described in Section 4.5 is subtracted this leaves an insertion loss for the intracavity components of 21% per round trip.

Further uncertainty was found in attempting to assign a decay time to the $^4I_{11/2}$ level. This decay time is of the order of 10ns and so for CW lasers is much faster than any other populating process. However, for Q-switched lasers with pulses widths of similar times, it is important. However, due to the rapidity of the decay [71] no reliable experimental values were found, and so a decay time of 10ns was chosen. In Section 5.5 the effect of this rate is investigated. The final parameters employed in the model are shown in Table 1.

5.4 Experimental

In order to modulate the cavity finesse for Q-switching it was necessary to gain access intra-cavity. This was facilitated by including an intra-cavity lens, in a manner similar to that described in section 4.8 on tunable fibre lasers. To provide for a low-Q and high-Q state a means of modulating the cavity finesse was required.

Initial work [72] employed a mechanical chopper with the experimental arrangement shown in Figure 61. To minimise the switching time it was necessary to arrange for the chopper to be placed close to a beam focus in the cavity, next to the output mirror in this case. The chopper was suitably designed to have a mark/space ratio of 1:300. The diode laser was a Hitachi HLP1400 device and the launch optics were as described in Section 2.4. The length of fibre (type ND199-05, Table 1) was approximately 2.5 metres in order to absorb most of the pump power. As the cavity loss was larger than in the CW configuration the optimum output reflectivity was changed and, of the mirrors then available, a mirror with R=40% at 1.088μm proved the most suitable. The laser threshold for CW action in this configuration was 3.4mW absorbed.

The peak pulse power obtainable with this system was just over 300mW with a FWHM of 500ns at a repetition rate of 400Hz and absorbed pump power of 5.6mW. The pulse power was limited by the relatively long switching time of the chopper. In addition, there was considerable jitter in the output pulses and no control of any after pulses.

In order to shorten the pulse duration and increase the peak pulse power it was necessary to modulate the cavity finesse more rapidly. This was attempted by employing an acousto-optic deflector (A.O.D.), Isomet type 1205C, instead of the mechanical chopper. Insertion of this device into the cavity described above increased the CW threshold to 3.7mW. As before the A.O.D. was placed as close as possible to the cavity focus to minimise the switching time. The A.O.D. was employed in transmission mode; the high-Q state being achieved by electrically switching the A.O.D. off with 2μs duration pulses. The A.O.D. allowed for greater control of the Q-switched pulses; a larger repetition rate could be achieved and after pulses could be suppressed.

In this configuration a mirror with 88% reflectivity at 1.09μm was found to be the optimum output coupler of those then available. A typical Q-switched pulse had a peak power of 30mW with a FWHM of 300ns at an absorbed power of 5.6mW. The repetition rate could be varied from single shot to 4kHz without any change in peak power or pulse duration. The peak power available with the A.O.D. was considerably less than that with the chopper due to the inefficient nature of the A.O.D. Even when the A.O.D. switched the cavity into its low-Q (ie "off") state some background CW laser action was observed, at a threshold of 5mW.

To avoid the problem of background laser action it was necessary to re-arrange the cavity [73], as shown in Figure 62. In this case the inefficient nature of the A.O.D. was usefully employed to couple out the pulse. In the low-Q state, with the A.O.D. off, there was no feedback from the mirror and so lasing action could not occur. In the high-Q state, with the A.O.D. on, approximately 40% of the light was diverted into the first order onto the highly reflective (R=99%) output mirror, thus generating feedback and initiating laser action. However, apart from the estimated 20% single-pass inherent loss, the rest of the light remained in the zero-order and was coupled out. Of the reflected light, 40% remained undeflected on passage back through the A.O.D. and represented useful output, although this was not collected.

For this experiment a Sharp LT015 40mW diode laser was employed. A typical Q-switched pulse obtained was characterised by a peak power was 13.3W, with a FWHM of 120ns at a repetition rate of 400Hz and 19mW absorbed power, thus a considerable improvement on the previous configuration. However, the A.O.D. was not placed at a cavity focus and and so the A.O.D. switching time was limited to 1μs

Further improvements in performance were obtained with the acquisition of a more efficient acousto-optic deflector. Using this device it was possible to again employ the cavity configuration shown in Figure 61 without background CW laser action reaching threshold. In addition, the switching time of the A.O.D. was significantly reduced, to about 30ns. In this way further increases in performance were obtained and the results are discussed in the next section.

5.5 Experimental and Theoretical Results

Four-level neodymium

Examination of the analytical model results for Q-switching, although not necessarily producing accurate results, does enable trends to be recognised. It can be seen from Section 5.2 that high peak power and short pulses are obtainable for systems pumped as far above threshold as possible and for short cavity decay times. In some respects these two requirements are contradictory as a lossy cavity enables short cavity decay times to be achieved but increases the laser threshold. Thus decreasing the fibre length, not applicable in the CW case, might reduce the decay time but reduces pump absorption and hence decreases the gain. In order to optimise performance it was necessary to investigate the variation of the available macroscopic parameters, such as fibre length and pump power launched. Many of the experimental results presented in this section were obtained in collaboration with Dr W.L. Barnes.

Pump power launched

It might be considered that maximising pump power was wholly desirable. However, as pointed out in Section 5.4, if there is too much gain in the system the A.O.D. was unable to hold off background CW laser action and Q-switching was disabled. Figures 63 and 64 show respectively the peak power and pulse FWHM as a function of pump power launched for two experimental plots employing different A.O.D.'s and analytical and numerical model theoretical plots. The agreement between the experimental and numerical model results is satisfactory, whereas the analytical predictions are not so successful. It can be seen that for pump powers larger than 20mW the peak power and width began to saturate, indicating that simply increasing the pump power may not be beneficial. Note that this result, of importance for the practical design of optimal systems, is not in any way predicted from the analytical descriptions. For reduced pump powers close to threshold the agreement between the numerical theory and experiment is not as satisfactory. The uncertainty errors on the numerical theoretical plot are a result of significant spike features on the Q-switched pulse, further analysis of which is left to Section 5.8. However, it must be remembered that importing the microscopic parameters determined from CW results to Q-switched behaviour may not be valid and factor of 2 agreement must be considered satisfactory. In addition there remained uncertainty in the behaviour of the A.O.D. at speed and the lower laser level decay rate.

Fibre length

For four-level CW lasers the optimum length was shown to be one that absorbed all of the pump, provided that the intrinsic fibre loss at the lasing wavelength was small. In a Q-switched system there was the competing requirement of reducing the fibre length to decrease the cavity decay time. Figure 65 shows the experimental and numerical theoretical dependence of the pulse peak power and width on fibre length. The agreement for pulse width was excellent for lengths from 0.5m to 10m. The peak power shows unusual behaviour for the experimental results. The character of the experimental results in the length region around 1m was due to excessive noise during the pulse. This was not the same as the "spiking" noise mentioned above and discussed in Section 5.8. Instead, this feature appeared to be possibly due to inconsistencies in the A.O.D., as a result of acoustic-wave reflection and distortion. In this region the setup was particularly sensitive to A.O.D. alignment. Further investigation is required.

Figure 65 shows clearly the concept of optimum length. For too short a fibre length there was insufficient pump absorption and hence reduced gain, whereas too long a length produced long pulses with reduced peak power. The optimum length was theoretically found to be 1.2 m for this particular configuration, close to the length of 1.1m projected from the "expected" experimental performance.

Output reflectivity

Figure 66 shows the results obtained against output mirror reflectivity. Optimum performance was achieved theoretically for an output coupler of 40% reflectivity. This was close to the experimentally determined figure of 52%. As before, a mirror with too large a reflectivity failed to couple out sufficient power while one with too small a reflectivity did not allow the laser to reach far enough above threshold.

Optimum Fibre Design

For investigating the role of microscopic parameters the numerical model was a useful tool. Figure 67 shows the expected performance of the Q-switched fibre laser as a function of the lower laser level decay time. It is significant that the decay times greater than 1ns degraded the laser performance. For a decay time of 10ns, as chosen in the model, this reduction was 25% in peak power. The influence of the glass host composition on decay times has been well documented [41], but it is unlikely that significant reductions in the lower laser level decay time would be possible.

Another component that might be tailored was the A.O.D.. Figures 68 and 69 show the effect of the A.O.D. switching time and diffraction efficiency. These are parameters which might be available for experimental adjustment. The optimum conditions was a compromise, as small switching times could be obtained by focussing the beam through the A.O.D. (possibly by employing a curved output mirror) but at the expense of reduced diffraction efficiency. Figure 68 indicates that the laser performance would fall off rapidly with decreasing diffraction efficiency. This was due to increased stimulated emission build up prior to Q-switching depopulating the inversion. This effect was discussed in Section 5.4 where zero order Q-switching with a less efficient A.O.D. had to abandoned due to the stimulated emission reaching laser action. Figure 68 also shows that there would be only a modest increase in peak power for efficiencies greater than 70%, while the fall off in performance with increased switching time from Figure 69 would be slow. The measured diffraction efficiency in an experimental optimised Q-switched fibre laser was 62%, close to this predicted value.

5.6 **Highly-Doped Fibres**

Further increases in Q-switched fibre performance could only be realised with the introduction of efficient highly doped fibres, allowing the use of short fibre lengths. Previous fabrication attempts at highly doped fibre via the solution doping techniques produced clustered fibres with shortened decay times and consequent gain reduction. However, the development of Al_2O_3 co-doped fibres enabled large dopant concentrations with greatly reduced clustering problems to be achieved.

In this section initial results are presented on Q-switched fibre lasers employing highly neodymium-doped fibre, co-doped with Al_2O_3. The assistance of Dr W.L. Barnes and others in helping to provide these results is acknowldged.

The addition of alumina to the fibre, type 518, also influenced some of the microscopic parameters [17]. The values chosen for the co-doped fibres are shown in Table 1. The dopant concentration was taken to be 920ppm, based on the "standard" ND490 concentration of 200ppm.

The experimental arrangement [26] for Q-switching was similar to that shown in Figure 61. However, it was found that replacement of the intra-cavity bulk lens with a 1/4 pitch Grinrod Selfoc lens proved advantageous. It enabled the open cavity length to be reduced by over 30% to 20cm, while retaining an acceptable A.O.D. diffraction efficiency.

The results obtained with this configuration were encouraging and a typical Q-switched pulse in Figure 70. Note that the peak power of 110W was of the same order of magnitude as that obtained from a miniature YAG laser which requires some 20 times the pump power. As described above, there existed an optimum fibre length. Figure 71 shows the results from the model QSW2.F77, indicating an optimum fibre length of 20cm. Unfortunately the experimental results are sparse as such short lengths of fibre were difficult to handle. Figure 72, indicates that increasing pump power would increase the pulse power, with no indication of the levelling shown in Figure 64.

Further increases in performance might be obtained by employing fibre manufactured using "soft glass" techniques. Such fibre could have dopant concentrations of over 1% without clustering or quenching as they are fabricated from bulk laser glasses. However, low-loss single-mode fibres employing this technique have yet to be manufactured. CW action has been obtained but with poor performance.

5.7 Three-Level Q-switching Results

In a manner similar to that adopted for the four-level Q-switching, the three-level transition in neodymium at 935nm was investigated [74]. The production of high peak power pulses at a wavelength compatible with silicon detectors is of considerable interest. Previous work [54] has relied in ion or ion/dye pump sources while any practical device must be pumped by solid state, compact devices such as LED's or diode lasers.

Numerical modelling of the three-level Q-switched laser proceeded in a similar manner to that described for the four-level laser, except that the intrinsic three-level nature meant that the lower laser level was implicitly included. Adjustment was made to the values chosen for the A.O.D. characteristics due to the shift in wavelength from 1088nm to 935nm. The parameters employed are shown in Table 2.

The experimental configuration is shown in Figure 61 except that the two diode multiplex scheme was employed to maximise the launched power. The fibre was type ND540-04, as employed in the CW laser experiments. Due to pump saturation, accurate determination of the launched power was difficult. The A.O.D. employed was an IntraAction device which had sufficient diffraction efficiency to hold off background CW laser action in the zero order mode. The fibre length was cutback to a length of 1.36m to achieve maximum performance.

A typical Q-switched pulse obtained at a repetition rate of 500Hz was characterised by a peak power of 5.2W, a FWHM of 80ns and a corresponding pulse energy of $0.2\mu J$. This result compares favourably with the value of "a few Watts" obtained by Alcock et al with 80mW pump power absorbed [54].

Figure 73 shows the experimental and numerical theoretical pulse characteristics as a function of pump power launched. The agreement between theory and experiment is not as good as that obtained for the four-level transition, but is still satisfactory. Figure 73 also indicates that further increases in launched pump power would be beneficial resulting from the more efficient nature of the A.O.D. at this wavelength. It is notable that the peak powers obtained (5.2W) compares well with the value obtained for the four-level transition with the GeO_2 fibre (13.3W). Hence it can be expected that similar increases in performance might be obtained by employing the Al_2O_3 fibre discussed earlier. In this case the numerical model may be employed to predict the optimum length and thus negate some of the difficult experiments involving short fibres on a clustered system.

As an indication of optimum length for the GeO_2 fibre, Figure 74 shows the Q-switched performance as a function of length. It is interesting to compare the experimental and theoretical results. The output mirror employed was unfortunately of poor quality with variations in reflectivity across its surface. Cutting the fibre back to a new length involved slight realignment and for each length the cavity focus lay on different parts of the mirror. This produced a large amount of scatter in the results and only a few data points were considered valid. It is possible that the optimum length was indeed around 1.8m as indicated by the theory and the experimental figure was a false result.

Unfortunately the output mirror employed was subsequently damaged over the entire surface and further work was suspended pending the acquisition of a new output mirror.

Figure 75 shows the experimental fibre laser performance as a function of repetition rate. As explained in Section 5.3 the roll off was not analysed by the theoretical single shot model. The 3dB drop in performance occurred at 3kHz, significantly larger than the frequency obtained in the four-level case. The roll-off frequency is significant for any possible fibre laser multiple shot application, such as OTDR.

5.8 **Noise Features**

One of the more significant successes of the numerical approach was the prediction, before conclusive experimental evidence emerged, of strong "spiking noise" patterns within the Q-switched pulse. This feature was briefly mentioned in section 5.5 and is now discussed further.

Upon examination of the output pulses from the QSW2.F77 program it was immediately apparent that the pulses obtained were not smoothly varying signals, as shown experimentally in Figure 70, but possessed large fluctuations as shown in Figure 78a. The cause of this feature was not immediately understood and it was necessary to program a PASCAL version of the model to enable graphics routines to display the cavity fields and populations as the pulses evolved.

It became apparent that the origin of the fluctuations was the stimulated field within the cavity just before the Q-switch was activated. It had previously been assumed that the spontaneous noise from which the pulse built up originated at the pumped end of the fibre. However, the largest signal energy density was found at the entrance to the A.O.D. The fibre was essentially loss-less and the travelling energy density built up in the fibre but increased along th fibre until it reached the loss mechanism of the A.O.D. The light was passed through the A.O.D. twice per round trip and the difference in energy density between the opposite propagation directions were over an order of magnitude. Hence, as the Q-switch opened, the difference in energy densities was retained during lasing action, producing spikes on the Q-switched pulse, separated by exactly one cavity round trip. Measurement of the spike separation confirmed this prediction.

Further evidence for the significance of the A.O.D. in this mechanism was found by noting the relative size of the spikes to the main Q-switch pulse as a function of A.O.D. diffraction efficiency. As the efficiency increased so must the difference in energy density on either side and hence the relative spike size. Figure 68 shows the relative spike noise obtained against diffraction efficiency and follows the expected trend.

No firm experimental evidence of this major noise feature was available. It had been occasionally noted that there appeared to be some ripple in the peak of the Q-switched pulse, but no conclusive traces were taken. It was realised that the experimental traces , such as in Figure 70, were a superposition of many pulses while the numerical model was only capable of single shots analysis. By reducing the repetition rate until the pulses could just be faintly seen, experimental pulses such as shown in Figure 76 were obtained. These confirm the presence of the noise spikes, at exactly the round trip interval as expected. However, their relative size is significantly less than the theory predicted. Further work revealed that the detection system employed was of insufficient bandwidth to accurately capture the spikes.

By convolving the detector and oscilloscope frequency response, a detection response time of 2ns was calculated.

To show how a theoretical pulse would appear when viewed with a detection system of limited bandwidth, a PASCAL program was written which imported the data from the QSW2.F77 model and displayed the pulse when viewed with a detector of given response time. The flow chart for the program is shown in Figure 77.

Figure 78 shows the results of viewing a theoretical pulse with different detector response times. It can be seen that as the detector response time increases the spikes are gradually reduced although the overall Q-switched pulse remained relatively unaffected. It can also be seen that the pulse shown in part b) with a 2ns detector response time is similar to that achieved experimentally in Figure 76. It should be noted that the pulse energy was calculated for the pulses and did not change, as required.

All the numerical model Q-switched pulses described in this thesis were analysed using the PASCAL PLOT1.PAS program with the appropriate detection response times.

The presence of the noise spikes on the Q-switched pulses would be an important consideration for any application and the numerical model enables analysis of this phenomenon to be performed.

5.9 Summary

A synopsis of the analytical theory employed to describe bulk Q-switched lasers has been presented. Comparison with experimental results has again indicated that a relatively simple analytical approach is inadequate. Development of the numerical model produced results which were similar to the experimental characteristics, both for four-level and three-level Q-switched fibre lasers. The numerical model enabled the influence of various experimental parameters to be assessed and indicated that some approaches to producing higher power pulses, such as increasing pump power, may not necessarily be beneficial.

Diode laser pumped Q-switched single mode fibre lasers have been described capable of producing pulses of over 110W peak power at 1088nm and 5.2W at 935nm. The presence of noise features on the Q-switched pulse was predicted by the numerical model and were subsequently discovered experimentally. These noise features would be of considerable importance to any practical application of a Q-switched fibre laser.

CHAPTER 6 : GRATING DEVICES

6.1 Introduction

The prospect of fabricating single-mode waveguide components in fibre format is a very attractive one [75]. It can be envisaged that many of the functions currently realised in bulk optic format may be transformed into single-mode fibre devices. Such elements offer the advantages of direct splicing capability, ruggedness, environmental isolation and possible increases in stability and performance.

Wavelength dependent and independent fibre couplers and splitters have already been fabricated using the fused taper technique [75]. These devices have found numerous applications and are now commercial items.

Furthermore, fibre devices have been fabricated which allow access to be gained to the single-mode evanescent field without removing the field from the fibre [76]. Such devices offer many possibilities for applications, including tunable couplers and ring dye lasers.

For active fibre applications, all-fibre devices are particularly attractive. Dichroic filters are desirable for launching pump power into amplifiers and optical feedback to construct fibre lasers. Such techniques eliminate the alignment problems associated with previous lasers and avoids the possibilities of poor butting to the bulk dielectric mirrors. In this way ring fibre lasers have been constructed [9]. Also, fibre ring Sagnac reflectors have been fabricated and usefully employed to form an all-fibre laser [10]. In addition, narrow bandwidth photochromic filters formed within the fibre core have been demonstrated [77]. Unfortunately the reflectivities of such gratings was too low for fibre laser applications.

Work has been performed which combined periodic structures with evanescent field access techniques. The periodic structure is useful for providing phase matching between modes which travel with different propagation velocities and has been employed in the integrated optics field to perform such functions as optical filtering, coupling into dielectric waveguides and distributed feedback for semiconductor diode lasers [78]. It is this last application which is of importance for fibre lasers as wavelength selective feedback had only previously been achieved by employing a bulk diffraction grating.

The fabrication of a periodic structure on the side of a polished single-mode fibre half coupler has already been demonstrated by Russell and Ulrich [79]. Their application was to a high resolution spectrometer and a second-order photoresist grating was deposited. Reflectivities up to 8% were reported. Further work by Sorin and Shaw [80] demonstrated backward wave coupling by placing a first-order metal grating in the evanescent field of a similar polished half coupler. Guided reflectivities up to 38% were demonstrated at 808nm for the TM-like mode. However, the presence of the metal produced considerable attenuation of this mode and only 0.3% reflectivity was observed for the TE-like mode.

The first high reflectivity single-mode fibre grating filters were produced by Bennion et al [81]. In this demonstration a first-order guided mode Bragg filter was fabricated by corrugations etched into the fibre core itself. The devices were narrow band (1.8nm at 1.3μm) and offered high reflectivities (>92%). Initial applications were centred around external cavity line narrowing of diode lasers [82].

It is the development of this fabrication technique in conjunction with doped fibres which has led to the construction of stable, narrow linewidth fibre lasers.

6.2 Fibre Grating Design and Theory

In this section a simple analytical theory of grating operation is presented. The format closely follows that adopted by Rowe, Bennion and Reid [83].

The basic structure of a fibre grating is shown in Figure 79 with a grating corrugation period of Λ. The waveguide properties of the device are best explained in terms of k-space as shown in Figure 80. Here, the grating period is represented as the grating constant k_g where

$$k_g = \frac{2\pi}{\Lambda}$$

Non guided waves travelling in the cladding and the superstrate are shown as circles of radii k_c and k_s respectively. The fibre core guided mode with propagation constant β is shown incident in the positive z direction.

In Figure 80 the incident mode is phase matched to waves radiated both in the superstrate and the cladding according to the relation

$$\beta - k_g = k_{s,c} \sin\theta_r \qquad (6.2.1)$$

If the grating constant is set according to the first order Bragg condition,

$$k_g = 2\beta \text{ or } \lambda = 2n_e \Lambda \qquad (6.2.2)$$

phase matching to a guided backward mode is achieved, as shown in Figure 81. It is worth noting that if the mode effective index, n_e, can be adjusted then a certain amount of tunability is allowed.

At wavelengths longer than that for the Bragg condition, ß is smaller and we find that $k_g > 2ß$, no phase matching can occur and the grating has no influence on the guided mode. For wavelengths shorter than the Bragg condition, the condition $k_g < 2k_c$ is satisfied and so phase matching into a mode radiated into the cladding is achieved. Thus for longer wavelengths the grating transmits while for shorter, incident light is lost to a radiated mode. This is clearly seen in the transmission plot of a typical grating shown in Figure 82. Obviously the range of wavelengths between the Bragg condition and the onset of radiation into the cladding is related to n_e-n_c. For weakly guiding fibre n_e-n_c is small and so the reflection bandwidth should be correspondingly narrow.

The above analysis assumes complete interaction with the grating whereas in practice the interaction might remain incomplete. To evaluate the interaction strength the following analysis was employed.

The effect of the grating corrugations can be considered as a polarisation source perturbation $\underline{P}_{pert}(\underline{r},t)$ on the wave equation

$$\nabla^2 E(\underline{r},t) = \mu\varepsilon \frac{\partial^2 E}{\partial t^2} \tag{6.2.3}$$

with $\underline{D} = \underline{E}\,\varepsilon_o + \underline{P}$ Equation (6.2.3) becomes for E_y

$$\nabla^2 E_y(\underline{r},t) = \mu\varepsilon \frac{\partial^2 E_y}{\partial t^2} + \mu \frac{\partial^2}{\partial t^2} [P_{pert}(\underline{r},t)]_y \tag{6.2.4}$$

E_y can be expressed as

$$E_y = \sum_{l} \frac{A_l(z)}{2}\, \xi_y^{(l)}(x)\, e^{\,i(\omega t-\beta_l\ z)} \qquad (6.2.5)$$

$$+$$

complex conjugate (c.c)

$$+$$

radiation modes (ignored)

where l extends over the discrete set of confined modes. Substituting (6.2.5) into (6.2.4) and assuming "slow" variations of A_l with z gives

$$\sum \left[-i\beta_l \frac{dA_l}{dz}\, \xi_y^{(l)}(x) e^{i(\omega t-\beta_l z)} \right] + \text{c.c.} = \mu \frac{\partial^2}{\partial t^2} (P_{pert})_y \qquad (6.2.6)$$

Multiplication of (6.2.6) by $\xi_y^{(m)}(x)$ and integration

yields

$$\frac{dA_m^{(-)}}{dz} e^{i(\omega t\ \beta_m\ z)} - \frac{dA_m^{(+)}}{dz} e^{i(\omega t-\beta_m\ z)} + \text{c.c.}$$

$$= \frac{-i}{2\omega} \frac{\partial^2}{\partial t^2} \int_{-\infty}^{\infty} [P_{pert}\ (\underline{r},t)]_y\ \xi_y^{(m)}(x)\ dx \qquad (6.2.7)$$

where use has been made of the orthogonality relation

$$\int_{-\infty}^{\infty} \xi_y^{(l)}\ \xi_y^{(m)}\ dx = \frac{2\omega\mu}{\beta_m}\, \delta_{l,m} \qquad (6.2.8)$$

Now $\underline{P} = [\varepsilon(\underline{r}) - \varepsilon_0]\underline{E}$ (6.2.9)

Thus

$$\underline{P}_{pert} = \Delta\varepsilon(\underline{r})\ \underline{E}(r,t) = \Delta n^2(\underline{r})\varepsilon_o\underline{E}(r,t) \qquad (6.2.10)$$

Using (6.2.5) for E_y, setting $l = m$ and substituting in (6.2.9) gives

$$[P_{pert}(\underline{r},t)]_y = \frac{\Delta n^2(\underline{r})\varepsilon_o}{2}[A_m^{(+)}(z)\xi_y^{(m)}(x)e^{i(\omega t-\beta_m\ z)}+c.c.] \qquad (6.2.11)$$

At the Bragg condition, (6.2.2), coupling will take between the forward and backward modes of order m. From (6.2.7)

$$\frac{dA_m^{(-)}}{dz} = \frac{i\omega\varepsilon_o}{4} A_m^{(+)}e^{-2i\beta_m z} \int_{\text{corrugations}} \Delta n^2(x,z)[\xi_y^{(m)}(x)]^2\ dx \qquad (6.2.12)$$

In the unperturbed medium two counterpropagating unmatched modes can be represented by

$$a(z,x,t) = Ae^{i(\omega_a t\ +\ \beta_a\ z)}f_a(z)$$

$$b(z,x,t) = Be^{i(\omega_b t\ +\ \beta_b\ z)}f_b(x) \qquad (6.2.13)$$

Introduction of the perturbation gives

$$\frac{dA}{dz} = k_{ab}\ Be^{-i\Delta z}$$

$$\frac{dB}{dz} = k_{ba}\ Ae^{-i\Delta z} \qquad (6.2.14)$$

Δ = phase mismatch constant

By conservation of total power

$$\frac{d}{dz}(|A|^2 - |B|^2) = 0 \qquad (6.2.15)$$

which is satisfied by (6.2.14) if

$$k_{ab} = k_{ba}* \tag{6.2.16}$$

Hence

$$\frac{dA}{dz} = k_{ab}\ Be^{-i\Delta z}$$

$$\frac{dB}{dz} = k_{ab}*\ Ae^{-i\Delta z} \tag{6.2.17}$$

If the perturbation extends from z = 0 to z = L then A(L) = 0 and the solutions of (6.2.17) are

$$A(z) = B(o)\ \frac{k_{ab}}{|k_{ab}|}\ \frac{\sinh[|kab|(z-L)]}{\cosh\ (|k_{ab}|L)} \tag{6.2.18}$$

$$B(z) = B(o)\ \frac{\cosh[|kab|(z-L)]}{\cosh\ (|k_{ab}|L)} \tag{6.2.19}$$

for the phase-matched condition $\Delta = 0$.

At z = 0 the perturbation reflectivity is given by

$$R = |A|^2 \tag{6.2.20}$$

Substitution from (6.2.18) gives

$$R = \tanh^2\ (KL) \tag{6.2.21}$$

where $K = |k_{ab}|$.

Combining (6.2.15), (6.2.12) and (6.2.13) yields

$$K = \frac{k_o{}^2}{2\beta\ N^2} \int_{\text{corrugation}} \Delta n^2(x,z)\ E^2(x)dx \tag{6.2.22}$$

where

$$N^2 = \int_{-\infty}^{\infty} E^2(x)dx$$

Thus to increase the interaction strength it was necessary to maximise the field strength at the corrugation layer and maximise the index difference without inducing any excess loss. For the structure employed by Ulrich the value of K was about 0.025mm^{-1}, which from Equation (6.2.21) corresponds to an interaction length of 40mm for satisfactory results. This was too long for any practical device and the problem results from the low value of the mode field at the corrugation boundary. This could be increased by placing a layer of higher index material onto the grating. However, this would also decrease Δn leaving a value of K of 0.02mm^{-1}. However, Δn could be increased by depositing a thin high index layer over the corrugations and increasing K to an acceptable 2.82mm^{-1}. The final grating design is shown in Figure 79 with the thin layer of Al_2O_3 providing the high index region.

6.3 **Fabrication**

The first step in fibre grating fabrication was to construct the basic field access device known as a polished half coupler. The construction technique follows that of Sorin and Shaw [80] and involved polishing away the fibre cladding to reveal the core. The assistance and guidance of Mr D.C.J. Reid and Mr C.J. Rowe in helping to prepare the gratings is acknowldged.

A length of locally stripped fibre was glued using UV curable glue (Norland Optical Adhesive no. 61) into a groove cut into a 15X20X35mm silica glass block. The groove was curved such that the fibre would be preferentially polished in the centre of the block rather than at the ends. The radius of the groove determined the the interaction length of the device; a larger radius of curvature meant that a greater length of the fibre was polished and the interaction length was increased. The radii of the grooves employed was usually 80cm. After curing, the fibre was reinforced at each end of the block, first by applying a small amount of epoxy and then some silicone rubber. This provided some ruggedness to the device.

The glued block was then mounted in a jig and levelled so that the lapping plane was parallel to the block. This ensured that the interaction region was at the centre of the block as intended. The block was lapped on an iron wheel with Al_2O_3 slurry until the fibre was reached. A typical lapping rate was approximately $2\mu m$ per minute. On lapping into the fibre the exposed fibre surface took the form of an ellipse, whose length indicated the depth already polished. At approximately $20\mu m$ from the fibre core the block was washed, transferred to a polyurethane wheel with Ce_2O_3 slurry and further polished. It was critical that the final polished surface was the correct distance from the core; too close and the device was lossy, too far and the interaction was too small. Unfortunately the exact distance depended not only on the fibre refractive index profile (RIP) but also on the desired wavelength of operation. Hence it was necessary to demount the block from time to time and test the interaction strength. This was achieved by launching light into the fibre and noting the increase in attenuation as a drop of oil was placed on the polished surface. A change of 35dB in transmitted power was acceptable. The device was then a completed polished half coupler.

The block was cleaned prior to photoresist application. It was essential that the polished surface was free from all contamination, otherwise the photoresist did not adhere properly. A successful cleaning technique involved mechanical cleaning in Microstrip, chemical cleaning in hexane reflux apparatus, plasma beam cleaning in an asher and a final Microstrip wash in an ultrasonic bath. The block was then baked at 80°C for 10 minutes before a layer of Shipley primer was spun on at 6000rpm. The blocks were baked for a further 10 minutes and a layer of Shipley AZ1350 thinned with 1:1.5 parts thinner spun on at 3000rpm. The photoresist layer was about 70nm thick. The block was then further baked for 30 minutes at 80°C.

A holographic interference pattern using an Ar+ laser operating at 457.9nm was set up such that the fringe separation equalled the Bragg grating period at the required wavelength. It must be recalled that the typical fringe separation was 0.36μm, representing a feature an order of magnitude smaller than those found on most semiconductor resist exposures. Successful exposure of the required sub-micron lithography was one of the more difficult stages; exposures of finer gratings, at 0.31μm for use as reflectors at 940nm, were all unsuccessful. After a typical exposure time of 40seconds the resist was developed and fixed. The fringe pattern was then transferred into the fibre by employing a chemically assisted reactive-ion beam etching technique (CARIBE). In this process argon ion etching was enhanced by the introduction into the reactive chamber of highly reactive CHF_3 and reliable etch rates of 80nm per min were achieved. After cleaning in the plasma asher to remove unwanted resist, a thin (90nm) layer of aluminium oxide was sputtered into the surface. The index of this layer was 1.6. Finally, this layer was in turn overlaid with a layer of index matching oil. The final grating structure is shown in Figure 79.

6.4 **Characterisation**

The main characteristic of a fibre grating is the narrowband reflection. Figures 82 and 83 show typical transmission and reflection traces for a fibre grating fabricated with a Bragg reflection wavelength of 1092nm. As explained in Section 6.2 , the transmitted light is reduced for wavelengths less than, and approaching, the Bragg wavelength due to coupling into the cladding. For longer wavelengths the light is transmitted whereas at the Bragg wavelength the transmission reached a minimum. The amount of light transmitted at the Bragg wavelength indicated the strength of the reflected wave, as the amount of light scattered at this wavelength was small. The reflection trace shows the expected narrow bandwidth high reflectivity characteristics. The width of the reflection trace was approximately 0.8nm. An estimate of the expected width can be found from the approximate relation:

$$\frac{\Delta\lambda}{\lambda} \approx \frac{\Lambda}{L} \tag{6.4.1}$$

For L= 1mm equation 6.4.1 gives $\Delta\lambda$ = 0.42nm at 1092nm. Combined with an experimental resolution of 0.5nm this value agrees well with the experimental value obtained.

One of the problems associated with corrugated optical waveguides was the presence of sidelobes due to the sharp commencement and end of the corrugations. These could be suppressed by tapering the corrugation depth (or interaction strength) with a function which has low, Fourier transform sidelobes [84]. With the fabrication technique described above, the interaction strength, due to the gradual curvature of the fibre, was a smoothly varying function. Hence sidelobes were not a problem with these fibre gratings.

By varying the index of the oil overlayer it was possible to achieve some degree of adjustment, both of the Bragg centre wavelength and reflectivity. This was due to a)the mode effective index, n_e, having a small dependence on the oil overlayer, thus affecting the Bragg condition given in equation and b)due to oil altering the mode overlap with the corrugations. Both these effects are clearly seen in Figure 84, which shows the reflection traces obtained by C.J. Rowe from a 1.55μm fibre grating. Tunable fibre gratings reported previously involved fabrication of chirped or fan type gratings impressed on a polished half coupler [85].

While index-matching oil as the overlayer material provided a convenient method of adjusting the grating characteristics, it was not suitable as a component on a rugged device. Instead, silica was sputtered as the overlayer. This had the added advantage that local heating of the oil, due to excess pump laser power for instance, was avoided. The thickness of silica was critical, as too little reduced the interaction strength while too much induced slab mode propagation. It was found that 29um of silica was optimum.

6.5 **Experimental**

The direct compatibility of fibre gratings with active fibres resulted in only slight modification to existing experimental arrangements to incorporate a grating.

A typical experimental configuration is shown in Figure 85. The pump launch setup was as described a number of times previously and shown in Figure 6. For the experimental convenience of allowing a number of devices to be built employing the same grating, the grating fibre and active fibre were not fusion spliced but were butted. This also enabled adjustment of the butt to be performed. Some etalon effects were observed at the butt between the fibres but these could be eliminated by placing a drop of index-matching oil on the butt.

A number of gratings, with different characteristics were fabricated. The fibre lasers constructed with them provided useful devices and the results are discussed in the next section.

6.6 Experimental Results

Neodymium

Initial experiments [27] were performed with 3 metres of Nd^{3+}-doped fibre type ND199-05 and grating type X3. The reflection and transmission characteristics of this particular grating are shown in Figures 82 and 83. The first experiment measured the lasing linewidth of the fibre laser. The grating fibre was characterised by a NA of 0.12 and $9\mu m$ core diameter, while the active fibre (Table 1) had an NA of 0.21 and $3.5\mu m$ core diameter. Hence there was considerable mis-match in the spot sizes of the two fibres and the loss at the butt joint was measured as 7dB single-pass. The threshold for laser action was 6mW absorbed, with a slope efficiency of less than 1%, due to the large intracavity loss. However, it was the spectral properties of the fibre laser which were of most interest.

The lasing spectrum was measured using a Fourier transform Michelson interferometer and consisted of an approximately Gaussian shaped output in the frequency domain with a FWHM of 1.5GHz, corresponding to some 50 longitudinal modes. The centre wavelength was 1092nm, coincident with the peak of the reflection curve, as expected. The laser linewidth was considerably less than the grating reflection bandwidth. This indicated strong modal gain competition. That the lasing spectrum did not collapse down to a single longitudinal mode, even though the linewidth was substantially less than the homogeneous linewidth, indicated the presence of spatial hole burning. Even so, the lasing linewidth was substantially less than that of the conventional cavity.

Optimum output coupling

In order to improve the lasing characteristics of the system another grating was fabricated, but with a fibre whose NA and cutoff matched that of the active doped fibre. The peak reflectivity of this grating (type S1) was centred at 1084nm with a FWHM of 300GHz. The butt loss was measured as 1.3dB single pass, further attempts to reduce this using taper techniques were unsuccessful.

Overlayer oils having a range of refractive indices were each placed in turn on the grating and the lasing characteristic measured. As expected, a change in refractive index of the oil caused a change in the reflection characteristics of the grating producing a different laser threshold and efficiency. Figure 86 shows the threshold and slope efficiencies for a range of oils. It can be seen that optimum performance was obtained with an oil of refractive index of 1.442, enabling a threshold of less than 2mW combined with a slope efficiency of 19% to be obtained. It can be noted that such smooth adjustment of output reflectivity to enable optimum output coupling to be achieved was not possible using the more common dielectric coated mirrors. The output spectrum of the system was measured again as a Gaussian in the frequency domain, centred at 1084nm with a FWHM of 16GHz.

Single longitudinal mode operation

From the above section it can be seen that fibre gratings enabled narrow linewidth fibre lasers to be realised. The initial experiments produced a linewidth of 1.5GHz. If a similar cavity could be constructed with a cavity longitudinal mode spacing greater than 1.5GHz then single longitudinal mode operation might be expected. The corresponding fibre length was calculated to be 6.8cm. To absorb significant pump light in this length it was necessary to fabricate a grating directly in a length of highly doped fibre.

After several attempts such a grating was successfully constructed, employing fibre fabricated using the solution doping technique. The fibre, type ND392, possessed characteristics as shown in Table 1. The peak of the reflectivity occurred at 1082nm with a measured bandwidth of 0.8nm. The maximum reflectivity was estimated to be greater than 80%, and probably close to 99%.

An experimental [28] arrangement similar to that shown in Figure 85 was employed, except that the pump source was a CW Rh6G dye laser operating at 594nm and the butt was not present.

Initially, the output from the fibre laser was analysed using a scanning Fabry-Perot interferometer. With an absorbed power of 40mW and a fibre cavity length of approximately 50cm (corresponding to a longitudinal mode spacing of 200MHz), some 10 longitudinal modes were seen to oscillate. The resultant total bandwidth was approximately 2GHz, similar to the results described above. The fibre cavity was then gradually cut back and the number of modes oscillating correspondingly decreased. At a length of 51mm only a single longitudinal mode was observed. This was the first single longitudinal mode fibre laser reported. Note that the cavity length was close to that estimated above. At this length, due to the relatively high dopant concentration, over 80% of the launched pump light was absorbed.

The threshold for laser action was 6mW absorbed power and the laser slope efficiency was 2.3%. These values were considerably less than optimum, due to non optimum output coupling and significant clustering present in the highly dope fibre.

The output wavelength was measured to be 1082nm, coincident with the peak reflectivity. The single longitudinal mode remained stable with no other modes visible up to a maximum launched power of 40mW, at which an output power of 0.78mW was obtained.

The spectral width of the fibre laser could not be measured by conventional analysers and it was necessary to construct a delayed self-heterodyne interferometer [86]. The experimental arrangement is shown in Figure 87. The interferometer employed a 2km fibre delay line and had a nominal resolution of 100kHz. The RF spectrum analyser had a resolution of 30kHz. The RF output from the interferometer was approximately Lorentzian in profile, indicating that the coherence length of the laser was significantly shorter than the interferometer delay line. Consequently the optical linewidth is half the measured RF linewidth of 2.6MHz FWHM, ie an optical linewidth of 1.3MHz. This width is about an order of magnitude less than the spectral width of a comparable DFB injection laser. This indicates the potential use of fibre lasers in coherent transmission systems, especially as limited tunability is available. Hence a range of stable, coherent, close spectrally spaced fibre laser sources can be envisaged.

An approximate indication of the expected linewidth may be obtained from the cavity decay time:

$$\Delta\omega = 1/\tau_C \qquad (6.5.1)$$

$\Delta\omega$ = FWHM of the resonator's Lorentzian response curve

τ_C = cavity decay time

The cavity decay time was measured by chopping the pump beam and noting the fibre laser relaxation frequency at different pump powers. Applying these values to (4.5.1) yielded a value for τ_C of 2.5×10^{-7} s. Insertion of this value into equation 6.5.1 gives $\Delta\omega$ = 4.0 MHz.

Note there is order of magnitude agreement. The disparity probably resulted from assessing the cavity decay time from the noisy relaxation oscillations.

Erbium

A line narrowed fibre laser operating at the important telecommunications wavelength of 1.55μm was constructed [29] in a manner similar to that shown in Figure 85. The pump source was a CW DCM dye laser operating at 650nm. The doped fibre (type ND263-01, Table 1) was characterised by an NA of 0.22 and a core diameter of 7μm, where as the grating fibre had an NA of 0.12 and 9μm core diameter. Hence again there was considerable loss, measured as 3.1dB single pass, at the butt joint.

In line with all three-level lasers it was necessary to determine the optimum fibre length in order to avoid an unsaturated absorbing region of fibre. It was found that a length of 2m of fibre was satisfactory. Optimum output coupling was attempted by changing the index of the oil overlayer on the grating. It was found that a reflectivity of 40%, peaked at 1.551μm, was optimum.

The lasing characteristics of the fibre laser at 1551nm demonstrated a slope efficiency of 5% and a lasing threshold of 13mW absorbed. The slope efficiency was less than might be expected due to the large butt loss and the peak reflectivity of the grating not being centred on the peak of the erbium gain.

The spectral characteristics of the laser output were measured using a scanning Fabry Perot interferometer. The free spectral range (FSR) of the interferometer was 13.8GHz and the finesse was estimated to be greater than 100. The output trace is shown in Figure 88. The output was approximately Gaussian in profile in the frequency domain with a FWHM of 4.9GHz (0.04nm), corresponding to fewer than 100 longitudinal cavity modes. The laser output linewidth was significantly narrower than that of the grating owing to modal gain competition. An increase in resolution of the interferometer revealed no structure on the curve and no decrease in FWHM. This indicated that there were no etalons formed by intra cavity components, as would be expected if bulk optic components were employed.

The prospect for single longitudinal mode operation of an erbium doped fibre laser are encouraging. The main difficulty lies in fabricating a fibre with the required dopant concentration. Whereas for a free-running three-level laser the length can be adjusted for single longitudinal mode operation there is the added constraint of ensuring the longitudinal mode spacing exceeds the lasing linewidth. Obviously at the same time the device must retain enough fibre length to allow for experimental mounting. Effort instead concentrated on reducing the grating reflection bandwidth, as discussed in Section 6.8

6.7. **Launching Pump Light Through Gratings**

In the drive towards all-fibre devices it was considered desirable to replace not only the output reflector with a fibre grating, as shown in Figure 85, but also the input reflector. Such a scheme could be readily realised by incorporating a dichroic coupler to introduce the pump light, as shown in Figure 89. This setup was attempted but unfortunately the losses at each splice were too large for lasing action to occur. Obviously it was necessary to employ two gratings with coincident peak reflectivities and unfortunately the only pair available were fabricated using fibre of different NA and cutoff to the doped and coupler fibre. The work discussed in this section involved launching pump light through an input grating, thus eliminating the need for a dichroic coupler.

The typical transmission for a fibre grating with peak reflectivity at 1092nm is shown in Figure 82. It can be seen that radiation into the cladding and superstrate results in a low transmission at the pump wavelength around 820nm. The measured insertion loss of the grating at this wavelength was 7dB. Thus a typical pump power launch efficiency of 35% was reduced to less than 8%. Unfortunately, for the same reasons described above, it was again necessary to employ gratings fabricated with non matching fibre and laser action was not observed.

Another approach to the problem was taken with reference to work on launching pump light directly into the grating at the correct angle, in a manner simply the reversal of the spectrometer technique reported by Ulrich and Russell [79]. It can be seen from Figure 80 that if pump light is projected onto the grating with the correct k vector, ie at the correct angle, then phase matching to the guided wave is achieved. Furthermore, as the polished fibre shape was an ellipse it might be considered that the elliptical output from a high powered phased array would enable high launch efficiencies to be achieved. Unfortunately, experimental launch efficiencies using this technique did not exceed 0.5%. The experimental arrangement employed , shown in Figure 90, indicates the reason. The problem results from the requirement that the pump light must be launched at an angle (about 45°) to the grating, whereas the phased array output is peaked normal to its emitting plane. Hence it was not possible to image the phased array output facet onto the ellipse plane without most of the output being lost. Further attempts were made by incorporating a diffraction grating to overcome this problem. However, total component loss and lens distortion reduced the launch efficiency to 0.4%.

6.8 **Concatenation of Gratings**

The substantial homogeneous broadening of rare-earth transitions in silica has been demonstrated by the line narrowed experiments. It was expected, due to the pseudo random nature of the glass host, that there would be a significant inhomogeneous component. This had been measured by a number of previous workers [21]. Multiple wavelength oscillation has been reported previously, but on different transitions and by splicing two doped fibres together [87]. In this experiment, simultaneous oscillation at two wavelengths on the $^3F_{3/2}$ - $^4I_{11/2}$ transition is investigated.

The experimental arrangement is shown in Figure 91. The two gratings reflected at 1085nm (A) and 1092nm (B) respectively. It was imperative that the gratings were placed in the cavity in the order shown. This was due to the transmission characteristics of the gratings (Figure 82) which shows that the gratings transmitted on the long wavelength side of the reflection wavelength.

Hence, the shorter reflection wavelength grating was placed "inside" the longer wavelength grating. By adjusting the index of the oil overlayers on each of the gratings it was possible to ensure that sufficient feedback was present from both gratings without too much loss at other wavelengths.

The output spectrum from the laser is shown in Figure 92. Both wavelengths, 1085nm and 1092nm, oscillated simultaneously, indicating strong inhomogeneous broadening, with spectral hole burning.

This experiment indicates one of the important potential applications for line narrowed fibre lasers as a multiple wavelength sources. The inhomogeneous component of the broadening allows multiple wavelength operation to be achieved and fibre grating techniques provide a means of finely controlling the output wavelengths and spectral widths. It is considered that long interaction length gratings, already realised in basic form and described in Sections 6.8 and 6.9, combined with active fibres, represent a critical step forward in WDM, coherent and other telecommunication devices.

6.9 **Motivation for D-fibre**

The technique described in Section 6.3 for fabricating fibre gratings was moderately successful. Two main areas of difficulty remained. Firstly, the polishing stage of the method presented numerous problems. In determining the end point of polishing it was necessary to demount, clean, test and remount the block. This was repeated a number of times and device failure at this stage was common due to the repeated handling. Secondly, there was a limit of about 1mm on the interaction length from the largest radius of curvature achievable. To fabricate fibre gratings with longer interaction lengths, either for narrower reflection bandwidth or for multiple gratings on one block, required a new method.

Other field access techniques had been reported, including a novel fibre design [88]. In this work the interaction plane was defined in the preform fabrication stage and was present over the whole length of the fibre. Utilisation of this fibre presented possibility of eliminating the two problem areas of the polishing technique discussed above.

6.10 **Fabrication of D-fibre.**

The fabrication technique for the covered D-fibre has been reported elsewhere [88]. However, it was found that fibre produced by this technique was not suitable for fibre gratings as the size of the covered hole was too small and, upon removing the covering, the fibre broke. It was necessary to investigate the fabrication technique and tailor the process for the particular fibre grating requirement.

The objective of the fabrication was to produce fibre with dimension as shown in Figure 93. It was vital that a) the fibre was made as strong as possible, so that stress centres could be eliminated, b) the fibre was pulled at as high a temperature as possible to reduce brittleness and c) the interaction surface should be flat.

The initial step of the process was to fabricate a base preform and the assistance of Dr G. Wylangowski, who produced the base preform, is gratefully acknowldged. The preform was fabricated by the normal vapour assisted deposition process. However, it was found necessary to avoid the inclusion of P_2O_5 in the process. This was normally introduced to reduce the fictive temperature.

Unfortunately the phosphorus also reduced the melting temperature of the core region and upon pulling, this caused the core to expand and distort the flat, as shown in Figure 94.

The flat was then milled into the preform using an ultrasonic milling machine. It was at this stage that the core-flat separation was defined. It was found that a separation (from the core centre to the flat) of a core diameter was optimum. The milling was similar to the polishing described in Section 6.3, except the the scale of the removal was some two orders of magnitude larger.

The milled preform was then sleeved using a silica tube. It was important that the preform fitted closely into the tube. If necessary either the tube or the preform was stretched to the correct diameter. A poor fit resulted into fibres as shown in Figure 94, with obvious stress centres and consequent low resistance to brittle damage.

The completed preform was then pulled in the conventional manner. This was the most difficult stage as the pulling temperature was critical. Figure 95 shows the effect of temperature. If the temperature was too hot the hole distorted and closed up, too cold and the inner preform and tube did not fuse together properly.

Figure 96 shows a completed successful fibre, type HD021-04. The core was undistorted, the interaction surface was flat, there were no sharp stress centres and the covering wall thickness was close to the optimum.

A more simple method of producing suitable fibre was investigated. This involved drilling a hole at the correct distance from the core in the preform stage. This technique was useful for converting already fabricated doped preforms into preforms suitable for fibre gratings. Unfortunately the correct drilling of the hole was difficult, but a successful preform was manufactured.

6.10.1 Fabrication of devices with D-fibre

To realise the goal of fabricating fibre gratings with D-fibre the first task was to remove the covering wall over the required fibre length. This was achieved by coarsely lapping the fibre instead of the more time consuming polishing. Once the covering wall had been broken through it was important that the lapping was stopped as further machining would have not only degraded the flat interaction surface but would also have allowed the slurry to travel up the opened D hole. A new mounting technique was developed. This involved cutting a 100X100μm straight groove 35mm long in a microscope slide with a diamond saw. The slide was then cut to size to match the block (15X35mm). To provide curvature the slide was heated in an oven at 650°C for 5 minutes under a specially shaped 3g weight to curve the slide, as shown in Figure 97. In this way relatively complex curve profiles could be easily achieved by altering the shape of the weight. This slide was then glued to a standard mounting block.

The fibre could then be glued in the groove. Firstly, a thin thin strip of UV glue (N.O.A. no 61) was run along the groove. The assembly was then heated to 100°C to release any bubbles in the glue. The locally stripped fibre was then placed in the glues and a thin (<100μm) coverslip placed on top. This ensured the fibre remained seated in the groove. While viewed under a microscope the fibre was rotated until the D-hole was uppermost and the UV glue quickly cured. The slight oval shape of the fibre shown in Figure 96 greatly aided this rotation. After complete curing the fibre ends were reinforced with epoxy and then silicone rubber yielding the final assembly as shown in Figure 98.

To remove a length of D-hole wall required lapping with an iron wheel and Al_2O_3 slurry. As the fibre was exposed, the ellipse, as described in Section 6.3, became visible. Lapping was stopped as soon as the hole had been broken into, as shown in Photo 99. As the end point was not critical, it was only necessary to stop lapping and visually inspect the groove every 20μm. Consequently the time to completion of this stage was 20 minutes, compared to 5 hours for the lapping and polishing technique described in section 6.3.

The device could then be cleaned and inspected. It was at this stage that any breaks in the fibre could be viewed. Some of the common causes of failure are shown in Figure 100. Part a) shows the effect of debris on the wheel; part b) the effect of a concealed air bubble; part c) has no obvious cause. Large stresses in the fibre appeared to cause minor breaks as in c) but these were reduced by improved preform fabrication as described above.

To prevent photoresist and other contamination from entering the remaining D-holes, silicone rubber was applied to the ends of the uncovered region. The remaining useful uncovered region, and hence the interaction length, was routinely greater than 5mm, almost an order of magnitude improvement over the previous technique. An oil drop attenuation test revealed sufficient interaction to increase attenuation by over 35dB.

The devices could then be spun with photoresist and exposed in the manner described in Section 6.3. It became apparent that as the interaction surface was inset in the block the normal cleaning procedures were not adequate. Longer cleaning times in the ultrasonic bath and asher gave some improvement, but poor photoresist adhesion remained a problem. This can be seen in Figure 101. Photo a) shows areas of resist lift off after exposure. Photo b), again after exposure, shows a good device. Consistent fringes can easily be seen.

The gratings produced were initially tested by launching HeNe 632.8nm laser light into the fibres. For a typical device, despite the absence of the high index overlayer, outcoupling was clearly visible and the interaction length was over 5mm. Unfortunately, due to failure of the ion beam etching apparatus it was not possible to etch the gratings and deposit the high index layer. This limited the interaction strengths to those seen by Ulrich and Russell. Hence it was not possible to obtain satisfactory reflection traces, but it is considered that the reflection bandwidth would be approximately 0.05 to 0.1nm. Attempts were made to line narrow a fibre laser with one of the gratings, but it appeared that the interaction strength, and hence the reflectivity, was too small.

6.10.2 Fabrication of devices with polished fibre

The development of a novel polishing technique for rapidly producing field access fibres [89] lead to another method of producing long interaction length gratings. The polishing technique has been described elsewhere and produced fibres with cladding removal over 5-10mm. In order to successfully clean, spin and expose a grating it was necessary to mount the fibre in a block. It was necessary to glue the fibre over most of its polished length, else the fibre broke during the asher cleaning or spinning processes. It was found that the UV glue employed previously, ran over the entire fibre. Hence, a more viscous, visible curing glue, LCR61 from ICI, was used. However, the glue appeared to leave deposits on the polished surface after cleaning which prevented resist adhesion. Subsequently it was found that cleaning with strong solvent ("Polystripper") of the central interaction region allowed some resist adhesion. Successful devices were then exposed as before, but no etching was available. These devices showed good outcoupling when HeNe 623.8nm light was launched and interaction lengths of a few millimetres.

Both novel processes were considerably faster to complete than the process described in section 6.3 and had a higher yield rate. More important, they represented methods of achieving long interaction length gratings. These gratings would find immediate application for very narrowline operation of fibre lasers, such as a single longitudinal mode Erbium-doped fibre laser or as multiple wavelength sources and analysers. A photo of one of the gratings described in section with Ar ion laser light launched is shown in Figure 102.

6.10 **Summary**

An analytical theory for the operation of narrow bandwidth fibre grating reflectors has been presented and the construction of fibre gratings has been described in detail. The incorporation of fibre gratings into fibre laser cavities has enabled narrow linewidth operation to be achieved. In addition, single longitudinal mode operation of a fibre laser has been presented.

Some of the difficulties of producing fibre gratings have been outlined. In order to overcome some of these drawbacks, construction of a novel fibre type, incorporating a D shaped hole close to the core, has been described. Rapid fabrication of long interaction length fibre gratings employing this fibre has been presented.

CHAPTER 7 : CONCLUSIONS

7.1 Conclusions and Future Work

Active devices are playing an increasingly important role in the technological development of a number of areas, such as telecommunications and solid-state sensors. Consistent with this growth is the demand for novel, reliable and compact devices in a variety of configurations. Diode pumped fibre amplifiers and lasers possess many of the characteristics required for application in the emerging technology.

It has been demonstrated that cheap semiconductor diode-lasers can be successfully employed as convenient pump souces and high launch efficiencies obtained. Complex launch schemes, involving many optical components, have not proved particularly successful. Future work should perhaps concentrate on fabricating diode-lasers with reduced astigmatism and more circular Gaussian output beams.

Fibre amplifier behaviour has been investigated and some fundamental active fibre characteristics measured. The possibility of employing a fibre amplifier as a broadband source, such as might be required for a ring laser gyro, has been examined. The prospects for a diode pumped Erbium-doped fibre amplifier operating at 1.55μm appear promising. However, it is possible that pump E.S.A. may force practical systems to be pumped at another wavelength, such as 980nm or 1490nm.

Diode pumped CW fibre lasers operating at 935nm, 1088nm and 1555nm have been described. The success of the recently introduced diode pumped Nd:YAG miniature laser indicates the demand for compact, solid-state sources. Further development of fibre lasers may enable more efficient devices to be fabricated and new diode pumped lasers, employing thulium or holmium for instance, can be expected.

Pulsed operation of a diode-pumped fibre laser has enabled a device capable of producing pulses of over 100W peak power at 1070nm to be constructed. These pulses are of sufficient power to induce significant non-linear behaviour and it is foreseen that continuation of this work could produce pulses of similar power from the transition at 935nm. It is interseting to note that frequency doubling of the three transitions in neodymium reported in this thesis (935nm, 1088nm and 1394nm) would produce the three visible primary colours.

Existing analytical theories of active fibre performance have been outlined but have been found to contain a number of problems. A numerical, computer based model has been proposed which attempts to overcome some of the diffculties. This model has been successfully applied to fibre amplifiers, and to CW and Q-switched fibre lasers. The model has been employed to estimate the performance of a diode pumped fibre device as a large pulse amplifier. In addition, the model enables parameters, perhaps not experimentally accessible, to be varied. Hence an optimum device configuration could be derived theoretically. Such a tool would prove invaluable in, for instance, predicting the optimum fibre length for a highly doped fibre operating on a three-level transition. Indeed, the uses of the model are only just emerging and many more applications, such as optimum A.O.D. specification, can be envisaged.

Fibre gratings have provided a convenient means of fabricating narrow-linewidth fibre lasers. With the growth in coherent telecommunications the demand for stable, narrow linewidth sources is increasing. Long interaction length gratings may provide the route towards multiple wavelength or extremely narrow-linewidth operation.

In conclusion, although the work presented in this thesis has contributed significantly to the growing field of active fibre devices, much work remains to be done.

LIST OF REFERENCES

References marked with an asterisk (*) are publications by the author.

1. Snyder, A.W. : "Understanding monomode optical fibres", Proc IEEE, 1981, 69, no.1, pp 6-13.

2. Young, C.G.. : "Glass lasers", Proc IEEE, 1969, 57, no.17, pp 1267-1288.

3. Snitzer, E. : "Optical maser action of Nd^{3+} in a barium crown glass", Phys Rev. Lett., 1961, 7, no.12, pp 444-446.

4. Koester, C.J. : "Laser action by enhanced total internal reflection", J. Qu. Elect., 1966, QE-2, no.9, pp 580-584.

5. Stone, J. and Burrus, C.A. : "Neodymium-doped silica lasers in end-pumped fiber geometry", Appl. Phys. Lett., 1973, 23, no.7, pp 388-389.

6. Stone, J. and Burrus, C.A. : "Neodymium-doped fiber lasers: room temperature CW operation with an injection laser pump", Appl. Optics, 1974, 13, no.6, pp 1256-1258.

7. Poole, S.B., Payne, D.N. and Fermann, M.E. : "Fabrication of low-loss optical fibres containing rare-earth ions", Elect. Lett, 1985, 21, no.17, pp 737-738.

8. Mears, R.J., Reekie, L., Poole, S.B. and Payne, D.N. : "Neodymium-doped silica single-mode fibre lasers", Elect. Lett., 1985, 21, no.17, pp 738-740.

9. Reekie, L., Mears, R.J., Poole, S.B. and Payne, D.N. : "Tunable single-mode fiber lasers", J. Light. Tech., 1986, LT-4, no.7, pp 956-960.

10. Urquhart, P:"Review of rare earth doped fibre lasers and amplifiers", IEE Proc J, 1988, 135, no.6, pp 385-407.

11. Farries, M.C., Morkel, P.R. and Townsend, J.E. : "Samarium-doped glass laser operating at 651nm", Elect. Lett., 1988, 24, no.11, pp 709-711.

12. Reekie, L., Mears, R.J., Poole, S.B. and Payne, D.N. : "A Pr^{3+}-doped single-mode fibre laser", IEE Conference "Advances in Solid-State Lasers", London, 1986, paper 9.

13. Namikawa, H., Arai, K., Kumata, K., Ishii, Y. and Tanaka, H. : "Preparation of Nd-doped SiO_2 glass by plasma torch CVD", Jap. J. Appl. Phys., 1982, 21, no.6, pp L360-L362.

14. Nagel, S., MacChesney, J.B. and Walker, K.L. : "An overview of the modified chemical vapor deposition (MCVD) process and performance", J. Qu. Elect., 1982, QE-18, no.4, pp 459-476.

15. Townsend, J.E., Poole, S.B. and Payne, D.N. : "Solution-doping technique for fabrication of rare-earth-doped optical fibres", Elect. Lett., 1987, 23, no.7, pp 329-331.

16. Arai, K., Namikawa, H., Kumata, K., Ishii, Y., Tanaka, H. and Iida, I. : "Fluorescence and its Nd^{3+} concentration dependence of Nd-doped SiO_2 glasses prepared by plasma torch CVD", Jap. J. Appl. Phys., 1983, 22, no.7, pp L397-L399.

17. Arai, K., Namikawa, H., Kumata, K., Honda, T., Ishii, Y. and Handa, T. : "Aluminium or phosphorus co-doping effects on the fluorescence and structural properties of neodymium-doped silica glass", J. Appl. Phys., 1986, 59, no.10, pp 3430-3436.

18. Poole, S.B. : "Fabrication of Al_2O_3 co-doped optical fibres by a solution-doping technique", ECOC 88, Digest no.292/1, pp 433-436.

19. Koester, C.J. and Snitzer, E. : "Amplification in a fiber laser", Appl. Optics, 1964, 3, no.10, pp 1182-1186.

20.(*) Mears, R.J., Reekie, L., Jauncey, I.M. and Payne, D.N. : "High-gain rare-earth-doped fiber amplifier at 1.54μm", OFC '87, paper W12, Reno, Nevada.

21. Pellgrino, J.M., Yen, W.M. and Weber, M.J. : "Composition dependence of Nd^{3+} homogenous linewidths in glasses", J. Appl. Phys., 1980, 51, no.12, pp 6332-6336.

22. Ainslie, B.J., Craig, S.P. and Davey, S.T. : "The absorption and fluorescence spectra of rare earth ions in silica-based monomode fiber", J. Light. Tech., 1988, LT-6, no.2, pp 287-293.

23.(*) Reekie, L., Jauncey, I.M., Poole, S.B. and Payne D.N. : "Diode-laser-pumped Nd^{3+}-doped fibre laser operating at 938nm", Elect. Lett, 1987, 23, no.17, pp 884-885.

24.(*) Reekie, L., Jauncey, I.M. and Payne, D.N. : "Near optimum operation of a diode-laser pumped fibre laser", ECOC '87 Tech. Digest, vol.1, pp 105-108.

25.(*) Reekie, L., Jauncey, I.M., Poole, S.B. and Payne, D.N. : "Diode-laser-pumped operation of an Er^{3+}-doped single-mode fibre laser", Elect. Lett., 1987, 23, no.20, pp 1076-1078.

26.(*) Barnes, W.L., Lin, J.T., Reekie, L., Taylor, D.J., Jauncey, I.M., Poole, S.B. and Payne, D.N. : "Q-switched and single polarisation laser diode pumped Nd^{3+}-doped fibre lasers", IEE Colloquium on All-Fibre Devices, London, 1988, Digest no.1988/90.

27.(*) Jauncey, I.M. et al : "Narrow linewidth fibre laser with integral fibre grating", Elect. Lett., 1986, 22, no.19, pp 987-988.

28.(*) Jauncey, I.M., Reekie, L., Townsend, J.E., Payne, D.N. and Rowe, C.J. : "Single-longitudinal-mode operation of an Nd^{3+}-doped fibre laser", Elect. Lett., 1988, 24, no.1, pp 24-26.

29.(*) Jauncey, I.M., Reekie, L., Mears, R.J. and Rowe, C.J. : "Narrowlinewidth fiber laser operating at 1.55μm", Optics Lett, 1987, 12, no.3, pp 164-165.

30. Streifer, W. et al : "Advances in diode laser pumps", J. Q. Elect., 1988, 24, no.6, pp 883-894.

31. O'Mahoney, M. and Millar, C.A. : "Semiconductor and active fibre amplifiers", OFC '88, paper THM1/2, New Orleans.

32. Yamamoto, S. et al : "Long-haul high-speed optical communication systems using a semiconductor laser amplifier", OFC '88, paper TUD2, New Orleans.

33.(*) Mears, R.J., Reekie, L., Jauncey, I.M. and Payne, D.N. : "Low-noise erbium-doped fibre amplifier operating at 1.54μm", Elect. Lett., 1987, 23, no.19, pp 1026-1028.

34. Digonnet, M.J.F. and Gaeta, C.J. : "Theoretical analysis of optical fiber laser amplifiers and oscillators", Appl. Optics, 1985, 24, no.5, pp 333-342.

35. Mears, R.J. : "Optical fibre lasers and amplifiers", PhD thesis, 1987, University of Southampton.

36. Snitzer, E. : "Fibre lasers and dispersion in fibres", First European Electro-Optics Markets and Technology Conference, 1971, pp 374-378.

37. Yariv, A. : "Optical Electronics", 1985, CBS Publishing, New York.

38. Smith, H.L. and Cohen, A.J. : "Absorption spectra of cations in alkali-silicate glasses of high ultra-voilet transmission", Phys. and Chem. of Glasses, 1963, 4, no.5, pp 173-188.

39. Sarkies, P.H., Sandoe, J.N. and Parke, S. : "Variation of Nd^{3+} cross section for stimulated emission with glass composition", J. Phys. D:Appl. Phys., 1971, 4, pp 1642-1649.

40. Weber, M.J., Ziegler, D.C. and Angell, C.A. : "Tailoring stimulated emission cross sections of Nd^{3+} laser glass: Observation of large cross sections for $BiCl_3$ glasses", J. Appl. Phys., 1982, 53, no.6, pp 4344-4350.

41. Brecher, C., Riseberg, L.A. and Weber, M.J. : "Line narrowed fluorescence spectra and site-dependent transition probailities of Nd^{3+} in oxide

and fluoride glasses", Phys. Rev. B, 1978, 18, no.10, pp 5799-5811.

42. Hartog, A.H. and Gold, M.P. : "On the theory of backscattering in single-mode optical fibres", J. Light. Tech., 1984, LT-2, no.2, pp 76-82.

43. DeShazer, L.G. and Komai, L.G. : "Fluorescence conversion efficiency of neodymium glass", JOSA, 1965, 55, no.8, pp 940-944.

44. Whitley, T.J. and Hodgkinson, T.G. : "1.54μm Er^{3+}-doped fibre amplifier optically pumped at 807nm", ECOC '88, Digest no.292/1, pp 58-61.

45. Laming, R.I., Morkel, P.R., Payne, D.N. and Reekie, L. : "Noise in erbium-doped fibre amplifiers", ECOC '88, Digest no.292/1, pp 54-58.

46. Laming, R.I., Reekie, L., Payne, D.N., Scrivener, P.L., Fontana, F. and Righetti, A. : "Optimal pumping of erbium-doped fibre optical amplifiers", ECOC '88, Digest no.292/2, pp 25-28.

47. Miller, I.D. et al : "New all-fibre laser", OFC '87, paper W13, Reno, Nevada.

48. Shimizu, M., Suda, H. and Horiguchi, M. : "High-efficiency Nd-doped fibre lasers using direct-coated dielectric mirrors", Elect. Lett., 1987, 23, no.15, pp 768-769.

49. Marcuse, D. and Stone, J. : "Coupling efficiency of front surface multilayer mirrors as fiber-end reflectors", J. Light. Tech., 1986, LT-4, no.4, pp 377-381.

50. Barnes, W.L. : Private communication.

51. Morkel, P.R., Farries, M.C. and Payne, D.N. : "Losses in fibre laser cavities", OFC '88, paper THD4, New Orleans.

52. Hanna, D.C., Smart, R.G., Suni, P.J., Ferguson, A.I. and Phillips, M.W. : "Measurements of fibre laser losses via relaxation oscillations", Optics Comms., 1988, 68, pp 128-133.

53. Vance, M.E. : "Saturation and excited-state absorption in neodymium laser glass", J. Qu. Elect, 1970, QE-6, no.5, pp 249-253.

54. Alcock, I.P., Ferguson, A.I., Hanna, D.C. and Tropper, A.C. : "Continuous-wave oscillation of a monomode neodymium-doped fibre laser at 0.9μm on the $^4F_{3/2}$-$^4I_{9/2}$ transition", Optics Comms., 1986, 58, no.6, pp 405-408.

55. Fan, T.Y. and Byer, R.L. : "Diode-laser pumped 946nm Nd:YAG laser at 300K", CLEO '86, paper FL3.

56. Mears, R.J., Reekie, L., Poole, S.B. and Payne, D.N. : "Low-threshold tunable CW and Q-swithced fibre laser operating at 1.55μm", Elect. Lett., 1986, 22, no.3, pp 159-160.

57. Millar, C.A., Miller, I.D., Anslie, B.J., Craig, S.P. and Armitage, J.R. : "Low threshold CW operation of an erbium-doped fibre laser pumped at 807nm wavelength", Elect. Lett, 1987, 23, pp 865-866.

58. Laming, R.I., Poole, S.B. and Tarbox, E.J. : "Pump excited-state absorption in erbium-doped fibres", Optics Lett., 1988, 13, no.12, pp 1084-1086.

59.(*) Jauncey, I.M., Reekie, L., Poole, S.B. and Payne, D.N. : "Extended wavelength operation of an Er^{3+}-doped fibre laser pumped at 808nm", OFC '88, paper THD2, New Orleans.

60. Kimura, Y. and Nakazawa, M. : "Lasing spectrum of P co-doped Nd^{3+} silica fibers", Jap. J. Appl. Phys., 1987, 26, no.8, pp L1253-L1254.

61. Liu, K., Digonnet, M., Fesler, K., Kim, B.Y. and Shaw, H.J. : "Broadband diode-pumped fibre laser", Elect. Lett, 1988, 24, no.14, pp 838-840.

62. Snitzer, E., Po, H., Hakimi, F., Tumminelli, R. and McCollum, B.C. : "Double clad, offset core Nd fiber laser", OFC '88, Postdeadline paper PD5, New Orleans.

63. Morkel, P.R., Farries, M.C. and Poole, S.B. : "Spectral variation of excited state absorption in neodymium doped fibre lasers", Optics Comms., 1988, 67, no.5, pp 349-352.

64. Miniscalco, W.J., Thompson, B.A. and Andrews, L.J. : "Nd^{3+}-doped fibre laser at 1.3um", OFC '88, paper THD1, New Orleans.

65. Brierley, M.C. and Millar, C.A. : "Amplification and lasing at 1350nm in a neidymium doped fluorozirconate fibre", Elect. Lett., 1988, 24, no.7, pp 438-439.

66. Hanna, D.C. et al : "Continuous-wave oscillation of a monomode thulium-doped fibre laser", Elect. Lett, 1988, 24, no.19, pp 1222-1223.

67. Koechner : "Solid state laser engineering", Springer Verlag, 1976, Berlin.

68. Carlson, D.G. : "Dynamics of a repetitively pump-pulsed Nd:YAG laser", J. Appl. Phys., 1968, 39, no.9, pp 4369-4374.

69. Gaeta, C.J., Digonnet, M.J.F. and Shaw, H.J. : "Pulse characteristics of Q-switched fiber lasers", J. Light. Tech., 1987, LT-5, no.12, pp 1645-1650.

70. Kleinman, D.A. : "The maser rate equations and spiking", Bell Syst. Tech. Jour., 1964, pp 1505-1519.

71. Martin, W.E. and Milam, D. : "Direct measurement of gain recovery in a saturated Nd-glass amplifier", Appl. Phys. Lett., 1978, 32, no.12, pp 816-818.

72.(*) Jauncey, I.M., Lin, J.T., Reekie, L. and Mears, R.J. : "Efficient diode-pumped CW and Q-switched single-mode fibre laser", Elect. Lett., 1986, 22, no.4, pp 198-199.

73.(*) Jauncey, I.M., Lin, J.T., Reekie, L., Mears, R.J. and Payne, D.N. : "A diode pumped single-mode fibre laser", IEE Colloquium on Nonlinear optical waveguides, 1986, London, paper 12, Digest no.1986/81.

74.(*) Reekie, L., Jauncey, I.M., Poole, S.B. and Payne, D.N. : "CW tunable and Q-switched operation at 938nm of a diode-laser pumped Nd^{3+}-doped fibre laser", CLEO '88, paper THM46, Anaheim.

75. Hill, K.O., Johnson, D.C. and Bilodeau, F. : "Advances in passive components", OFC '88, Paper THE1, New Orleans.

76. Parriaux, O., Godin, S. and Kuznetsov, A.A. : "Distributed coupling on ploished single-mode optical fibers", Appl. Optics, 1981, 20, no.14, pp 2420-2423.

77. Kawasaki, B.S., Hill, K.O., Johnson, D.C. and Fujii, Y. : "Narrow-band Bragg reflectors in optical fibers", Optics Lett., 1978, 3, no.2, pp 66-68.

78. Yariv, A. and Nakamura, M. : "Periodic structures for integrated optics", J. Quant. Elect., 1977, QE-13, no.4, pp 233-253.

79. Russell, P.St.J., and Ulrich, R. : "Grating-fiber coupler as a high-resolution spectrometer", Optics Lett, 1985, 10, no.6, pp 291-293.

80. Sorin, W.V. and Shaw, H.J. : "A single-mode fiber evanescent grating reflector", J. Light. Tech., 1985, LT-3, no.5, pp 1041-1043.

81. Bennion, I., Reid, D.C.J., Rowe, C.J. and Stewart. W.J. : "High reflectivity monomode-fibre grating filters", Elect. Lett., 1986, 22, pp 341-343.

82. Park, C.A. et al : "Single-mode behaviour of a multimode 1.55μm laser with a fibre grating external cavity", Elect. Lett, 1986, 22, no.21, pp 1132-1134.

83. Rowe, C.J., Bennion, I. and Reid, D.C.J. : "High reflectivity surface relief gratings in single-mode optical fibres", IEE Proc. J., 1987, 134, no.3 pp 197-202.

84. Corss, P.S. and Kogelnik, H. : "Sidelobe suppression in corrigated-waveguide filters", Optics Lett., 1977, 1, no.1, pp 43-45.

85. Whalen, M.S., Tennant, D.M., Alferness, R.C., Koren, U. and Bosworth, R. : "Wavelength-tunable single-mode fibre grating reflector", Elect. Lett, 1986, 22, no.24, pp 1307-1308.

86. Richter, L.E., Mandelberg, H.I., Kruger, M.S. and McGrath, P.A. : "Phase noise measurements of external cavity semiconductor lasers", CLEO '85, Tech. Dig, pp 52-53, Baltimore.

87. Nakazawa, M. and Kimura, Y. : "Simultaneous oscillation at 0.91, 1.08 and 1.53μm in a fusion spliced fiber laser", Appl. Phys. Lett., 1987, 51, no.22, pp 1768-1770.

88. Li, L., Wylangowski, G., Payne, D.N. and Birch, R.D. : "Broadband metal/glass single-mode fibre polarisers", Elect. Lett., 1986, 22, no.19, pp 1020-1022.

89. Hussey, C.D. and Minelly, J.D. : "Optical fibre polishing with a motor-driven polishing wheel", Elect. Lett., 1988, 24, no.13, pp 805-807.

Twice

LIST OF FIGURES

Number	490	499	199	392	518	540	450	263	291
Dopant	Nd^{3+}	Nd^{3+}	Nd^{3+}	Nd^{3+}	Nd^{3+} Al_2O_3	Nd^{3+}	Er^{3+}	Er^{3+}	Tm^{3+}
Concentration (ppm)	200	107	74	1000	920	62	300	150	830
N.A.	0.21	0.17	0.21	0.20	0.17	0.24	0.27	0.22	0.15
Cutoff (μm)	0.78	0.78	0.96	0.94	0.81	0.76	1.1	1.4	1.7
λ Laser (μm)	1.09	1.09	1.09	1.09	1.07	0.94	1.6	1.6	1.9
σ_p 810 (X10-25m ^{2})	16	16	16		16	16			
σ_p 826 (X10-25m ^{2})	9.5	9.5	9.5		9.5	9.5			
σ_L (X10-25m ^{2})	12.5	12.5	12.5		17.5	12.5			
σ_A (X10-25m ^{2})	6.5	6.5	6.5		7.4	6.5			
Boltz						0.09			
F_L	15	15	15		15	15			
F_A	7	7	7		7	7			
T_{fl} (μs)	450	450	450		400	450			
T_{sp32} (μs)	1125	1125	1125		850	1125			
T_{sp31} (μs)	804	804	804			804			
T_{21} (ns)	10	10	10		5	10			
ratio	10	10	10		10	10			
Saturation loss	0.19	0.19	0.19		0.0	0.19			
Eta	0.58	0.58	0.58		0.58	0.58			

Table 1. Fibre data.

Fibre/ Wavelength (μm)	Fibre length (m)	Open cavity length (m)	AOD diffraction efficiency	AOD single-pass loss	AOD switch time (ns)
490-04/ 1.09	1.2	0.2	0.62	0.13	30
518-04/ 1.07	0.17	0.3	0.60	0.13	20
540-04/ 0.94	1.36	0.2	0.75	0.10	20

Table 2. Values for various parameters concerned with investigation of Q-switched behaviour.

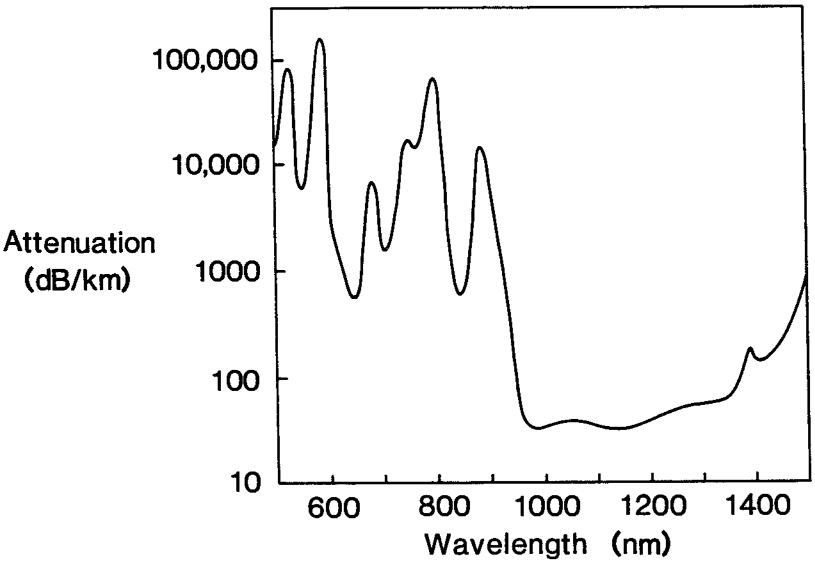

Figure 1. Neodymium-doped fibre attenuation spectrum.

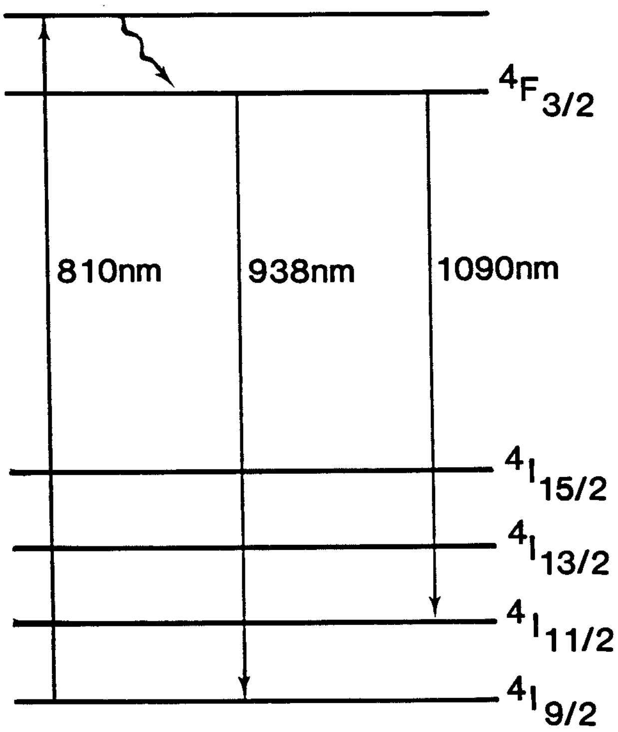

Figure 2. Neodymium energy levels with excitations and decays.

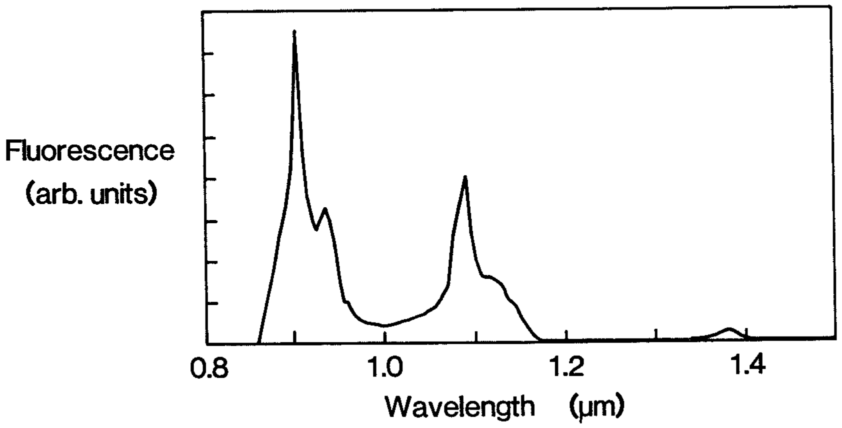

Figure 3. Neodymium-doped fibre fluorescence spectrum.

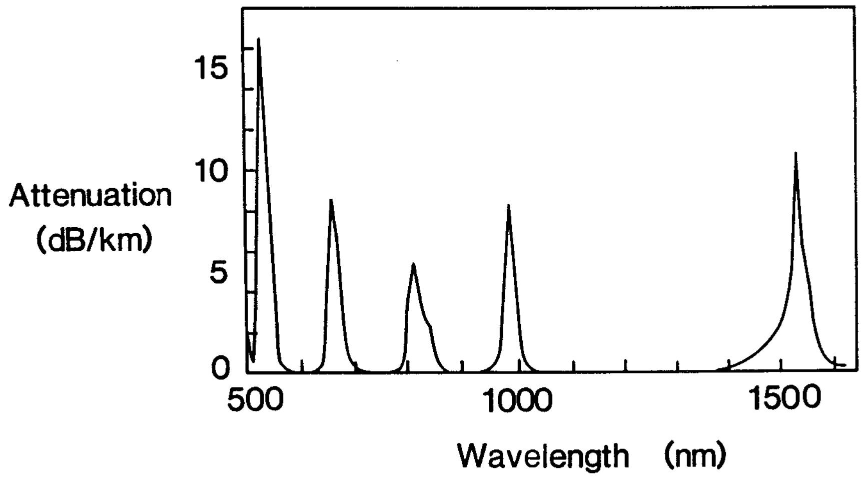

Figure 4. Erbium-doped fibre attenuation spectrum.

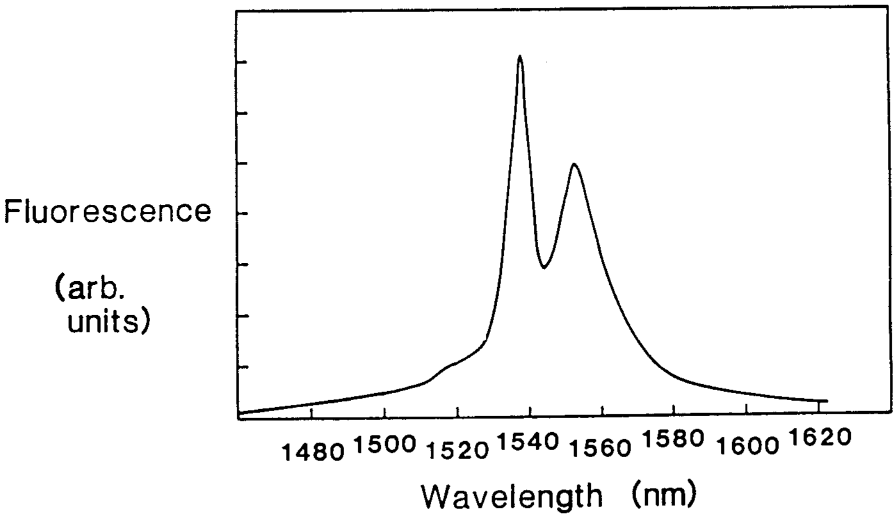

Figure 5. Erbium-doped fibre fluorescence spectrum.

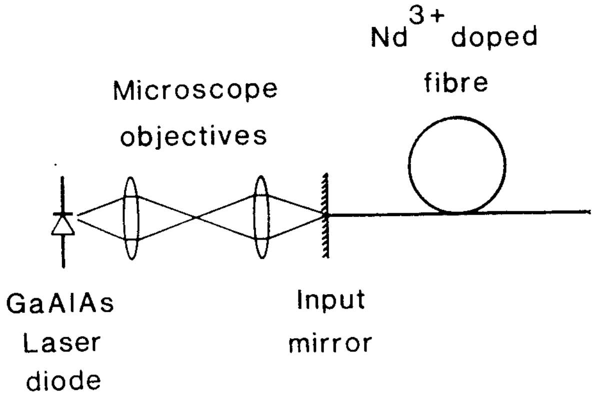

Figure 6. Simple diode-laser launch scheme.

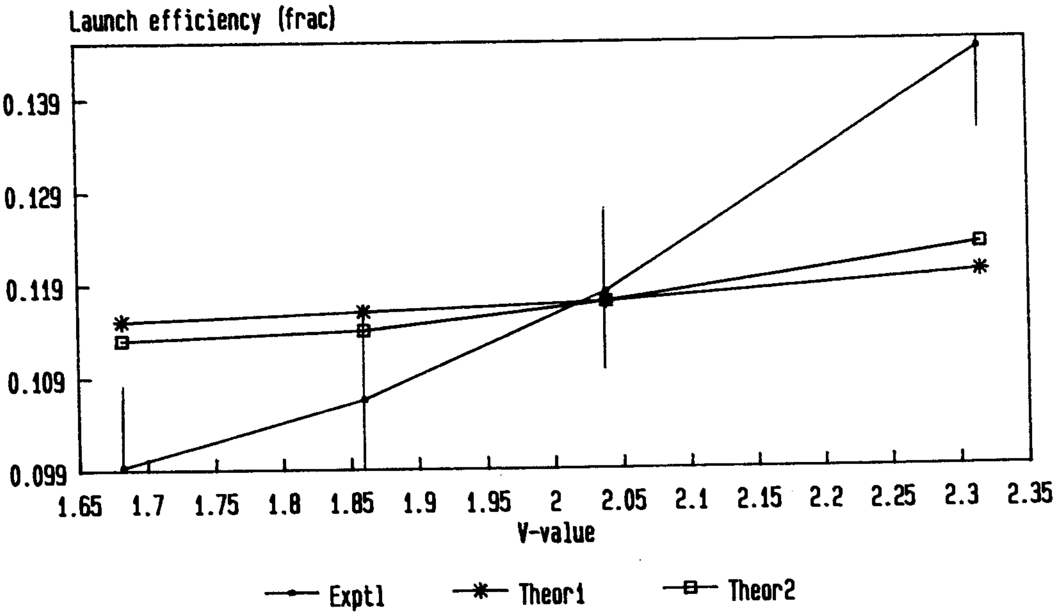

Figure 7. Experimental and theoretical launch efficiency against V-value.

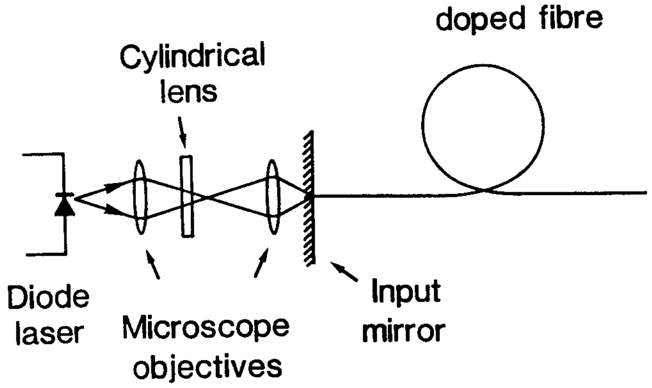

Figure 8. Diode-laser launch scheme with cylindrical lens.

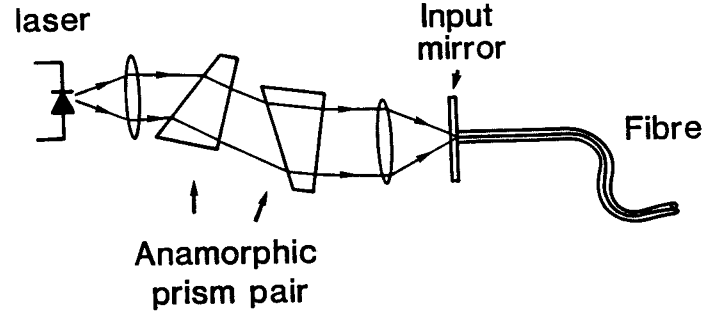

Figure 9. Diode-laser launch scheme with anamorphic prism pair.

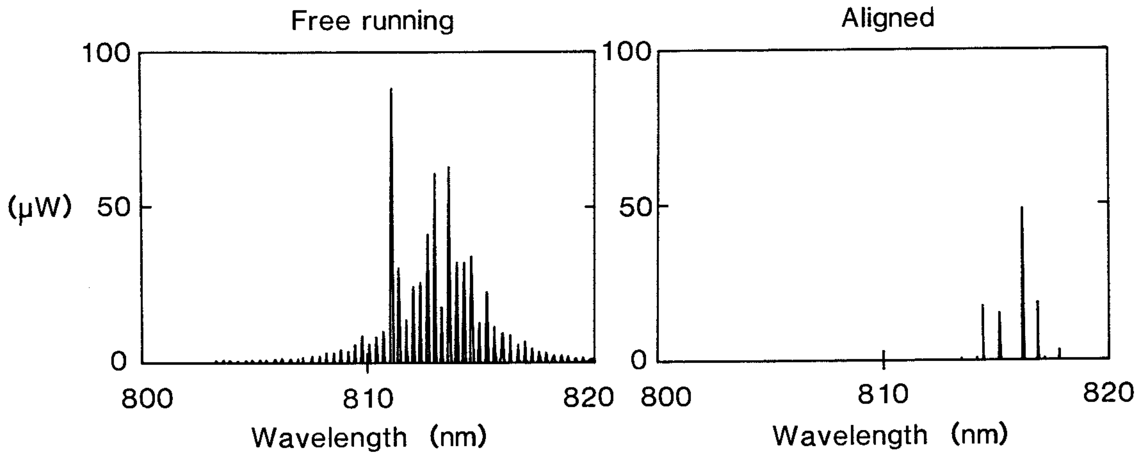

Figure 10. Diode-laser output spectrum, aligned and not aligned.

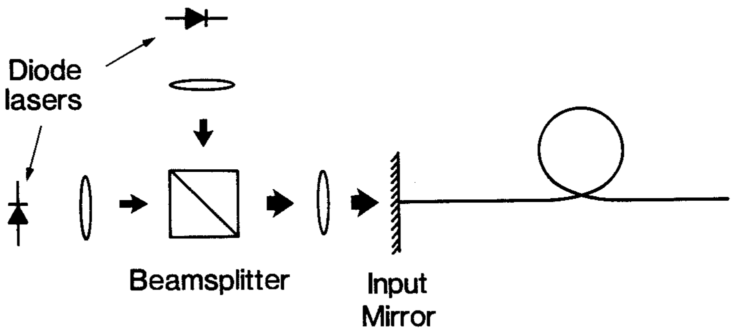

Figure 11. Two-diode-laser multiplex launch scheme.

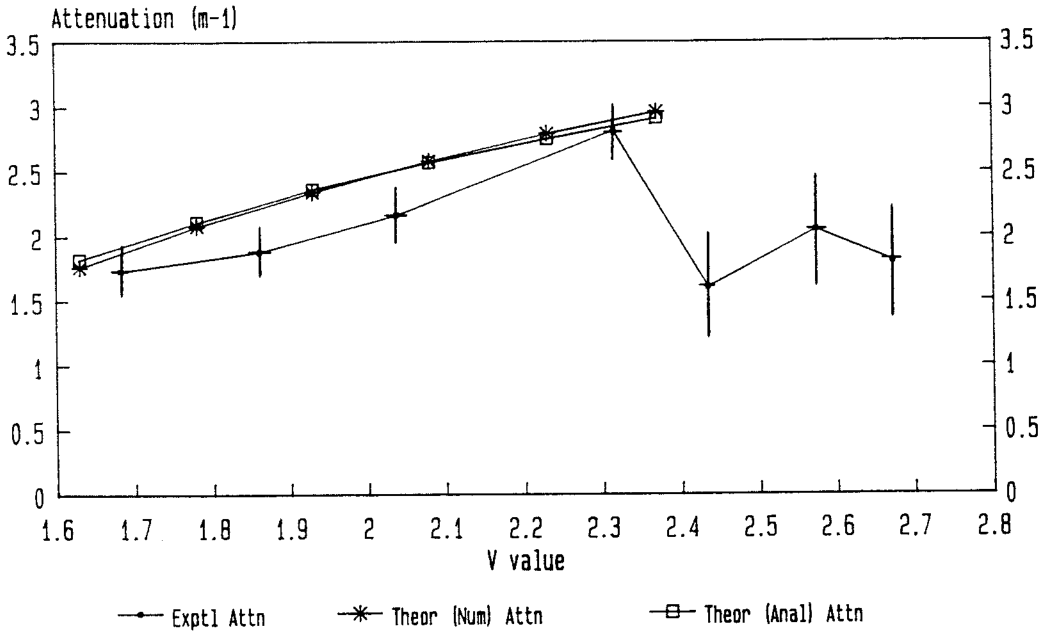

Figure 12. Experimental and theoretical fibre attenuation against V-value.

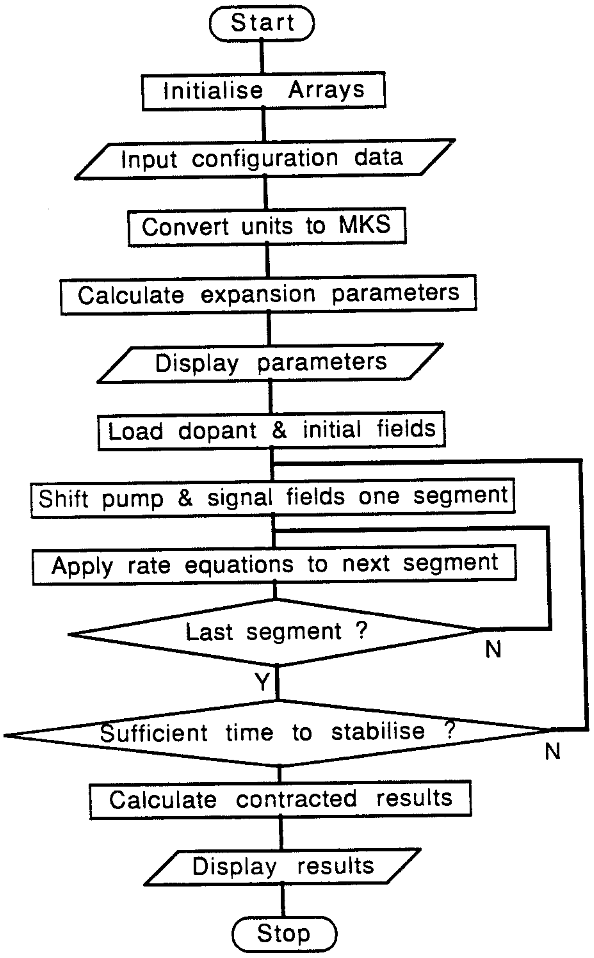

Figure 13. FORTRAN program AMP3.F77 flow chart.

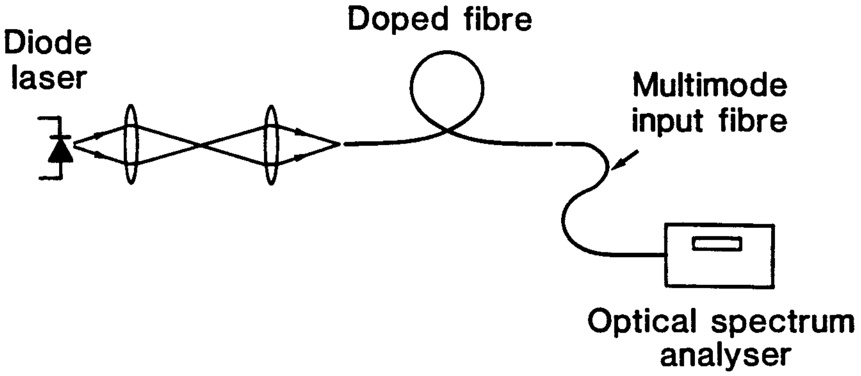

Figure 14. Experimental setup employed to determine branching ratio.

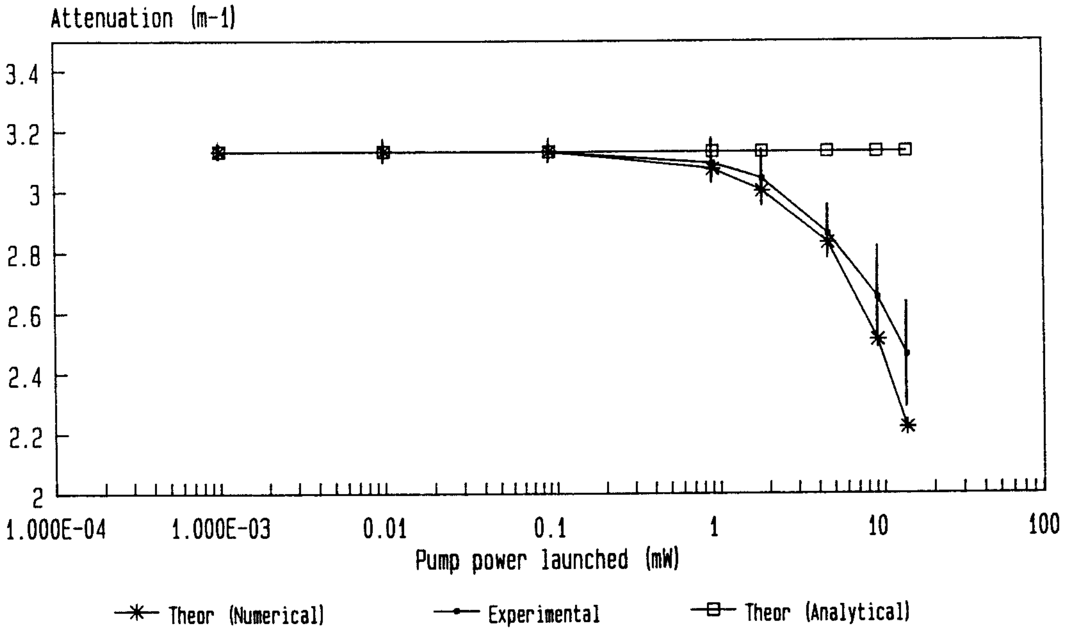

Figure 15. Experimental and theoretical fibre attenuation against launched pump power.

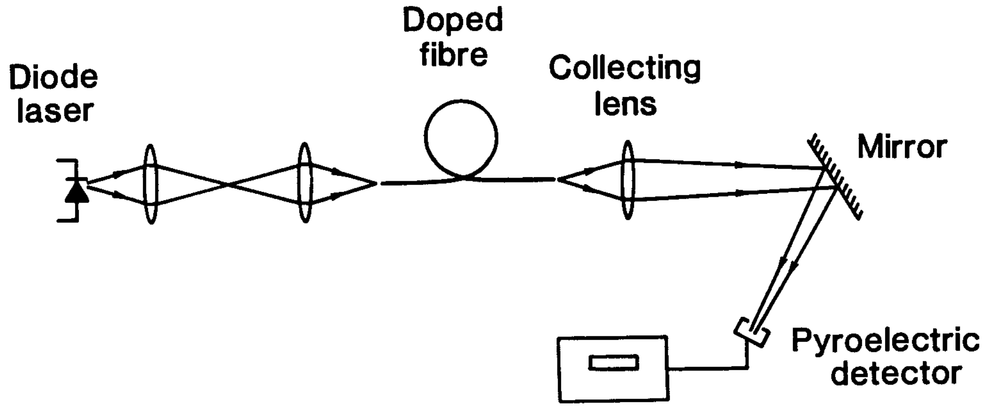

Figure 16. Experimental setup employed to determine A.S.E. output.

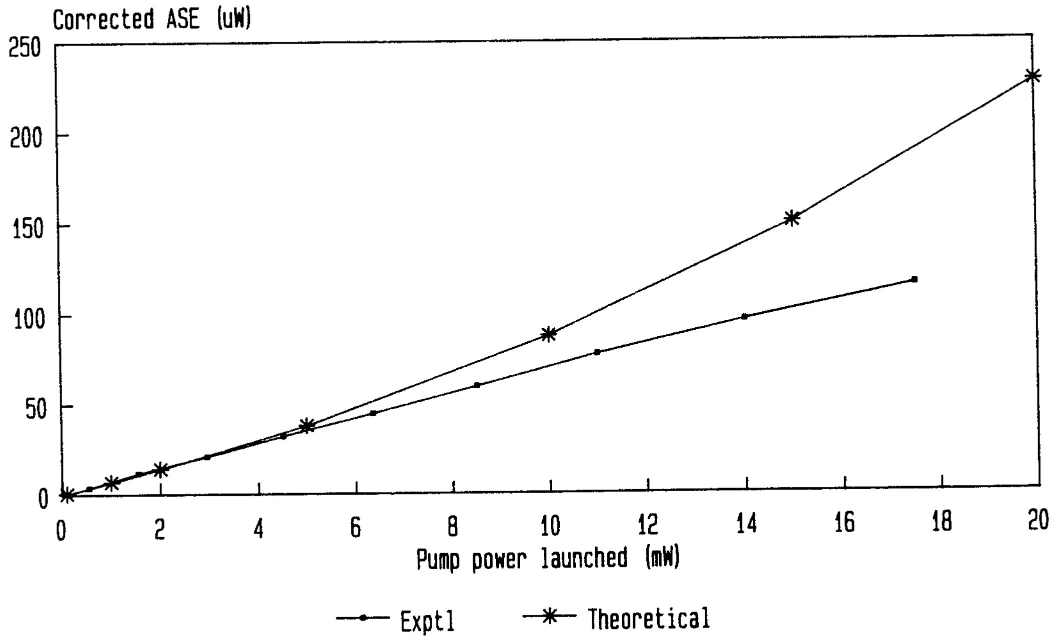

Figure 17. Experimental and theoretical A.S.E. output against launched pump power.

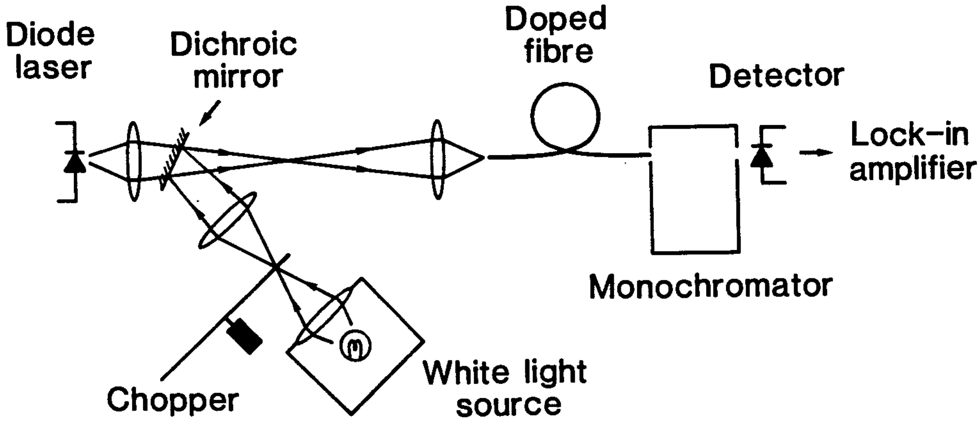

Figure 18. Experimental setup employed to determine small signal gain coefficient.

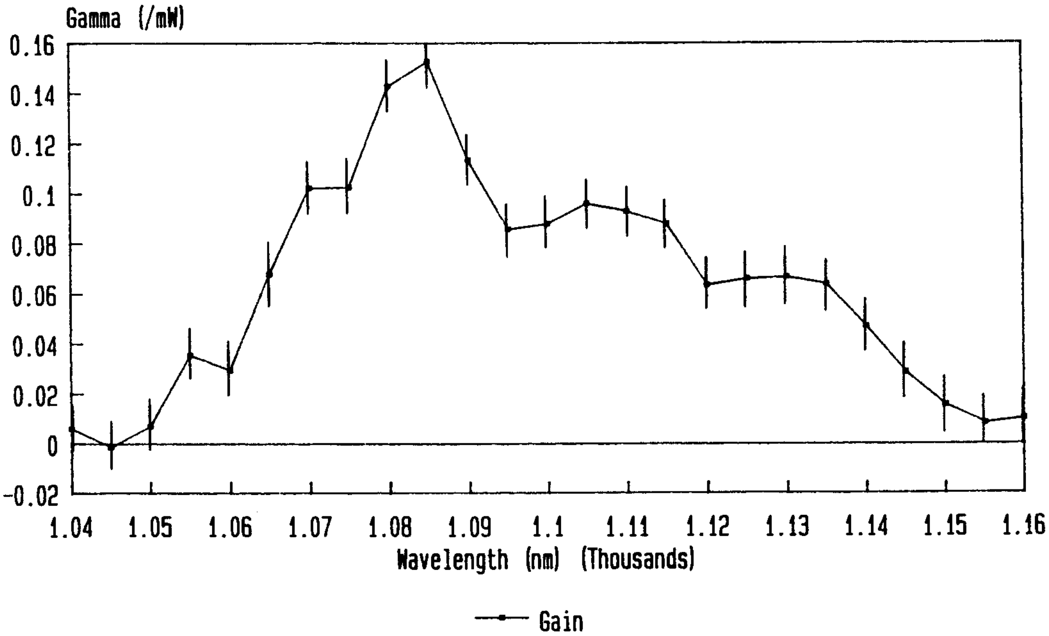

Figure 19. Experimental plot of small signal gain coefficient against wavelength around 1088nm.

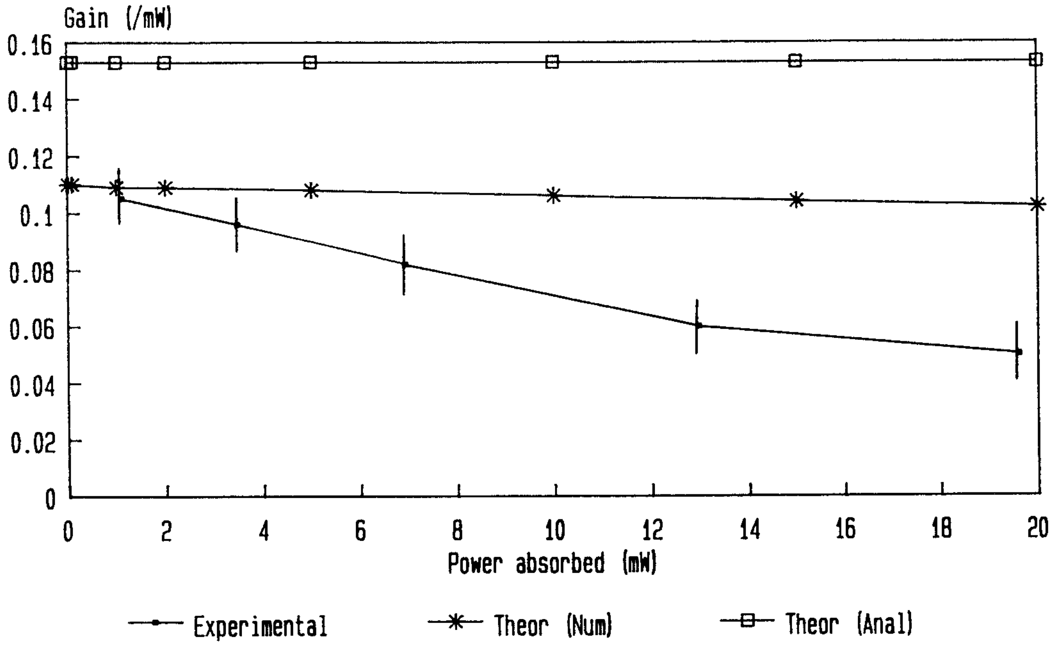

Figure 20. Experimental and theoretical small signal gain coefficient against pump power.

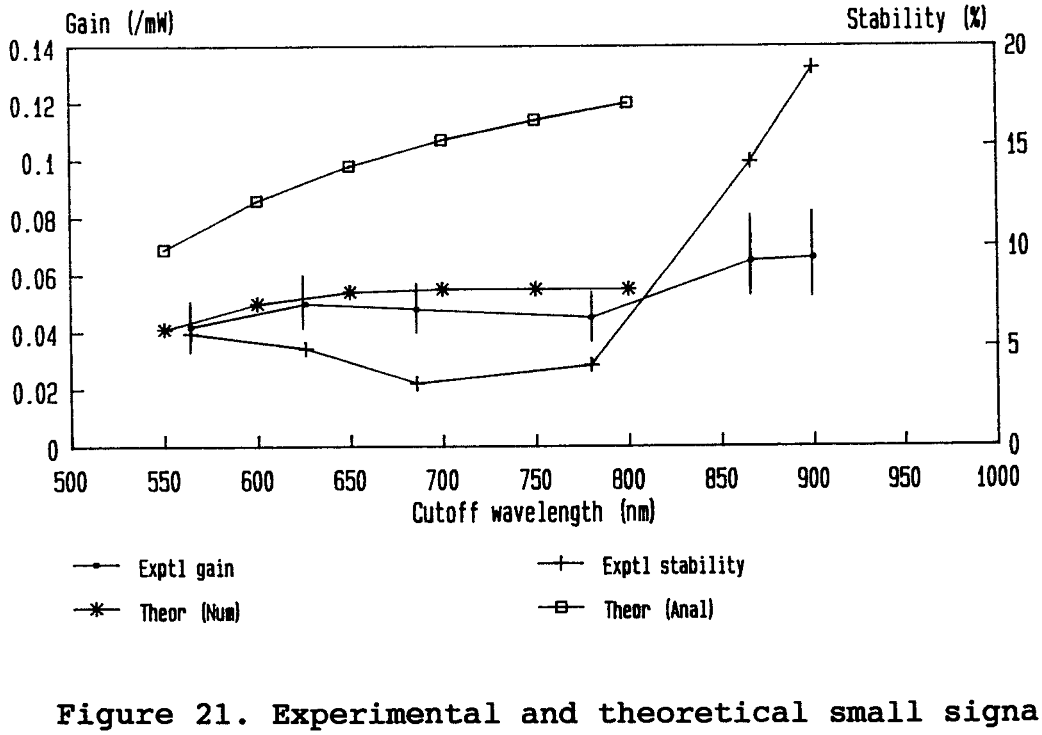

Figure 21. Experimental and theoretical small signal gain coefficient against cut-off wavelength.

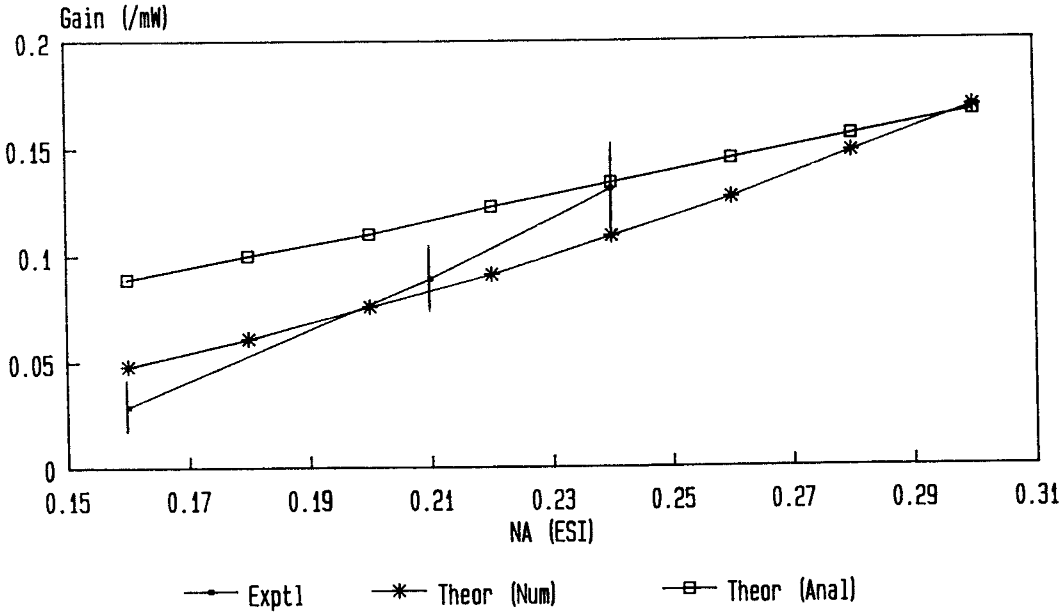

Figure 22. Experimental and theoretical small signal gain coefficient against N.A.

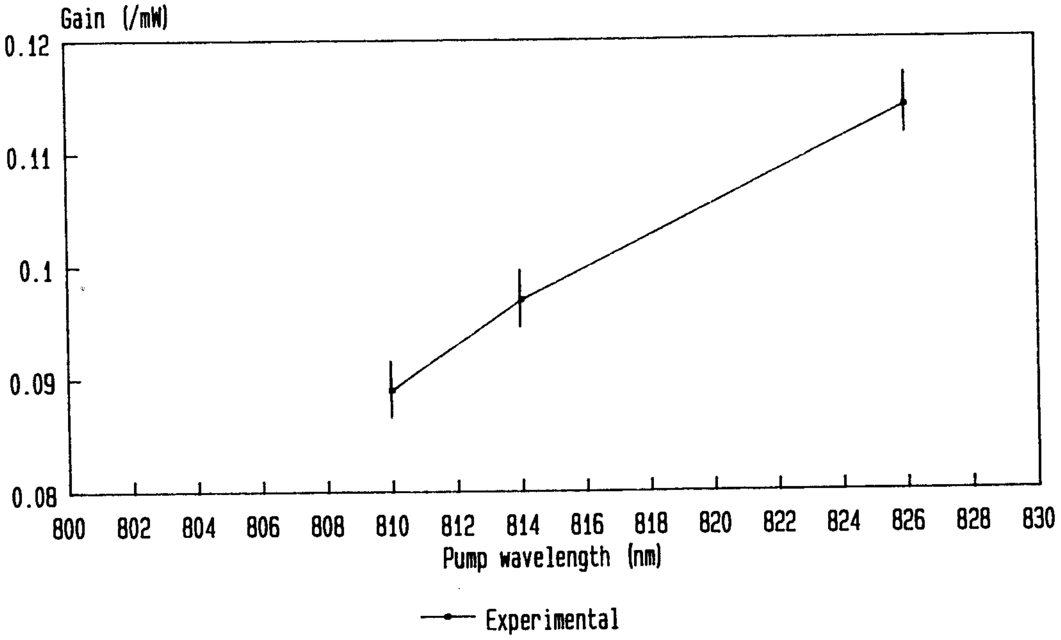

Figure 23. Experimental small signal gain coefficient against pump wavelength.

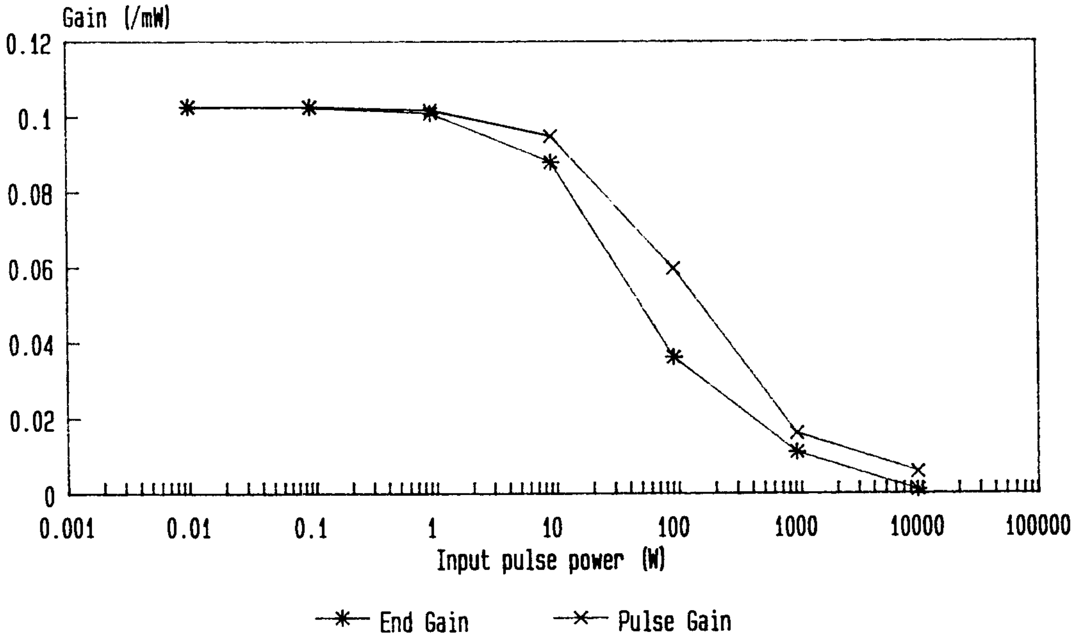

Figure 24. Theoretical gain coefficient against input power for large input signals.

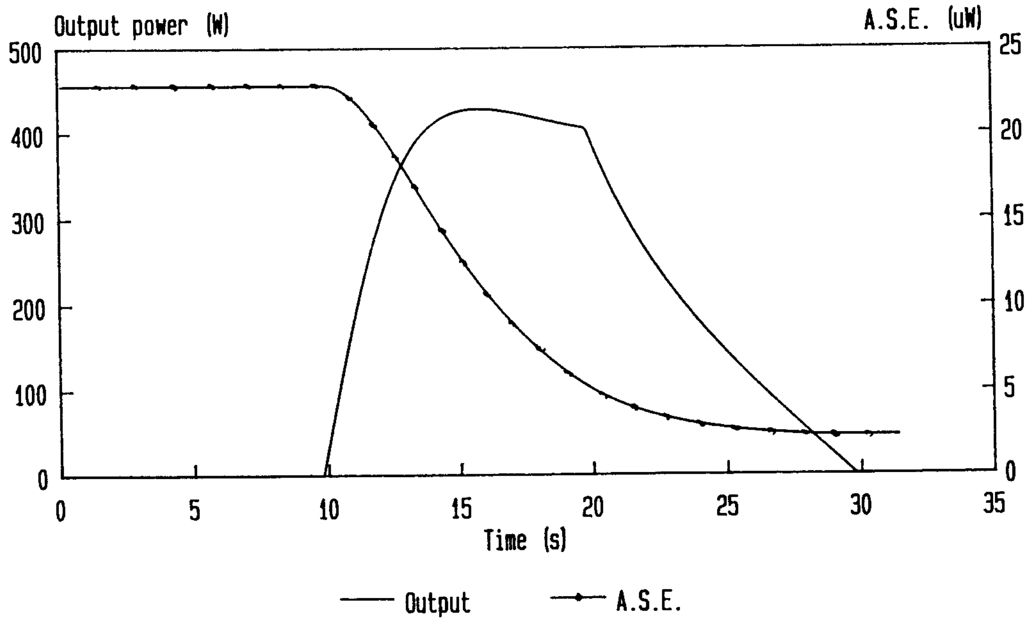

Figure 25. Theoretical distorted output profile from large triangular input pulse and fibre amplifier.

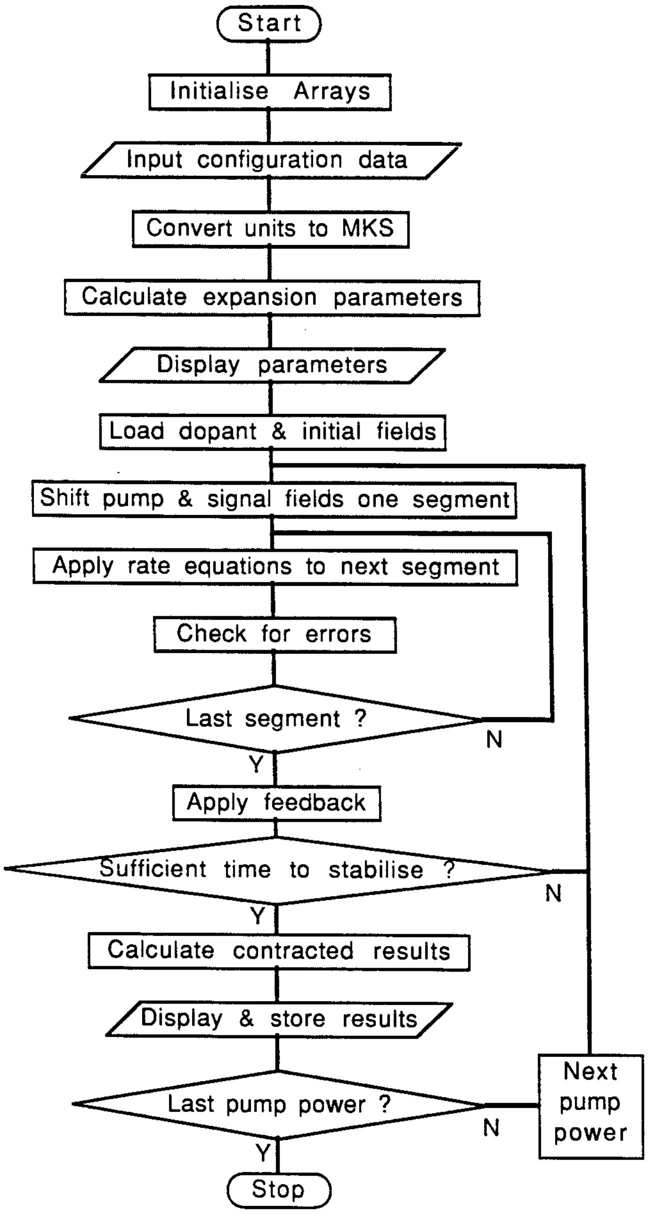

Figure 26. FORTRAN program CW2.F77 flow chart.

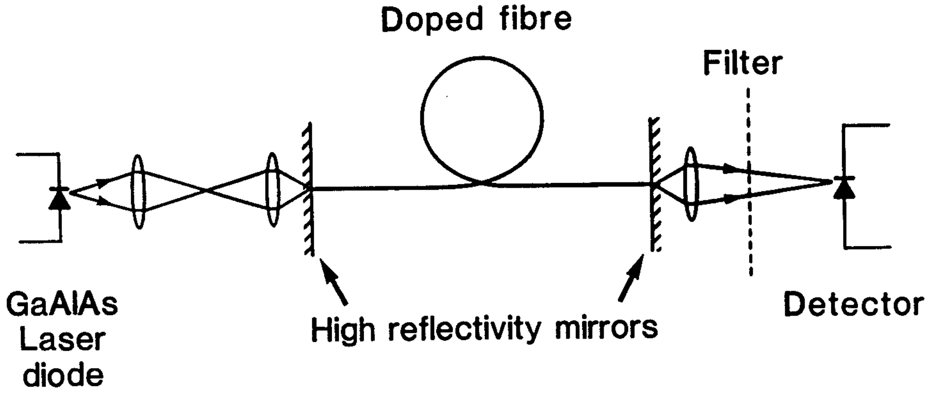

Figure 27. Experimental setup employed to characterise CW fibre lasers.

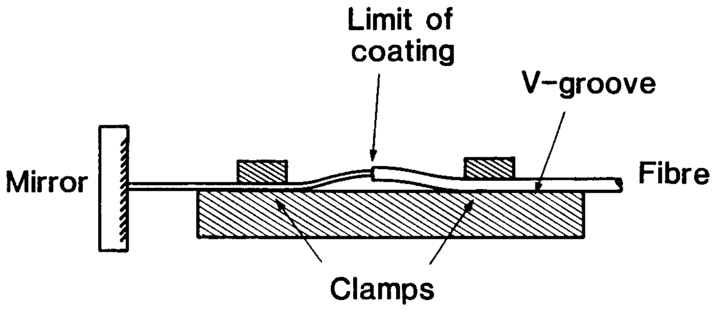

Figure 28. Detail of experimental arrangement employed to butt fibre to dielectric mirror.

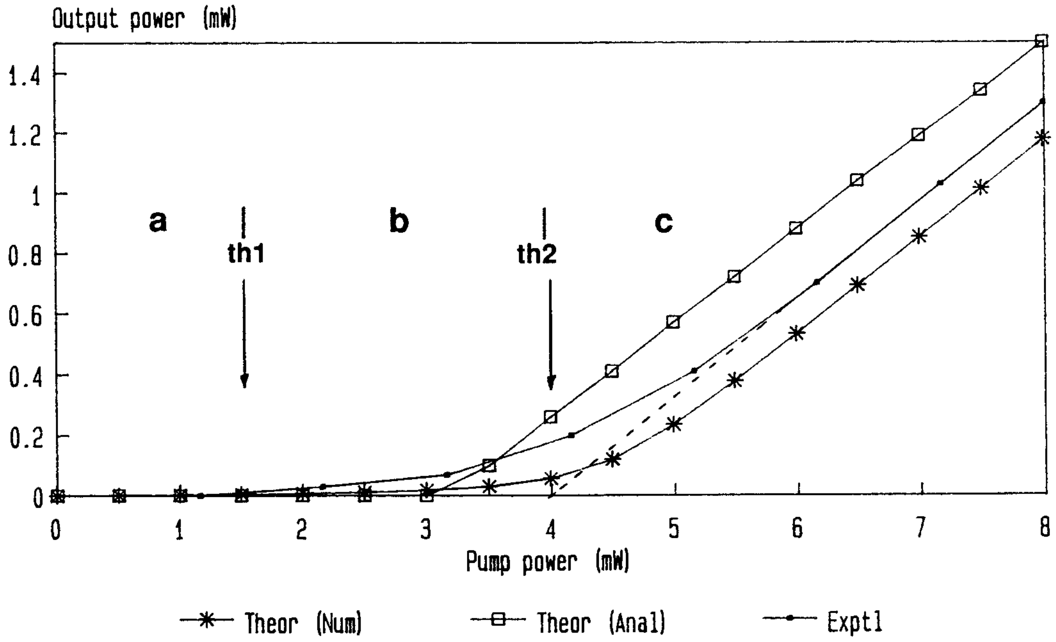

Figure 29. Typical CW lasing characteristic.

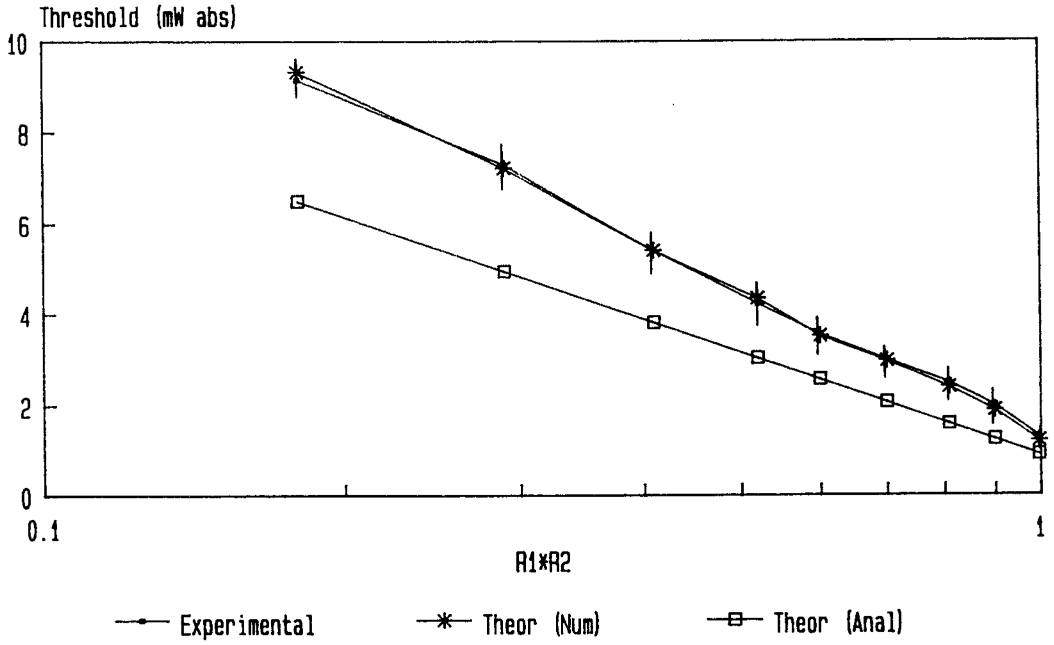

Figure 30. Experimental and theoretical CW fibre laser threshold against output mirror reflectivity.

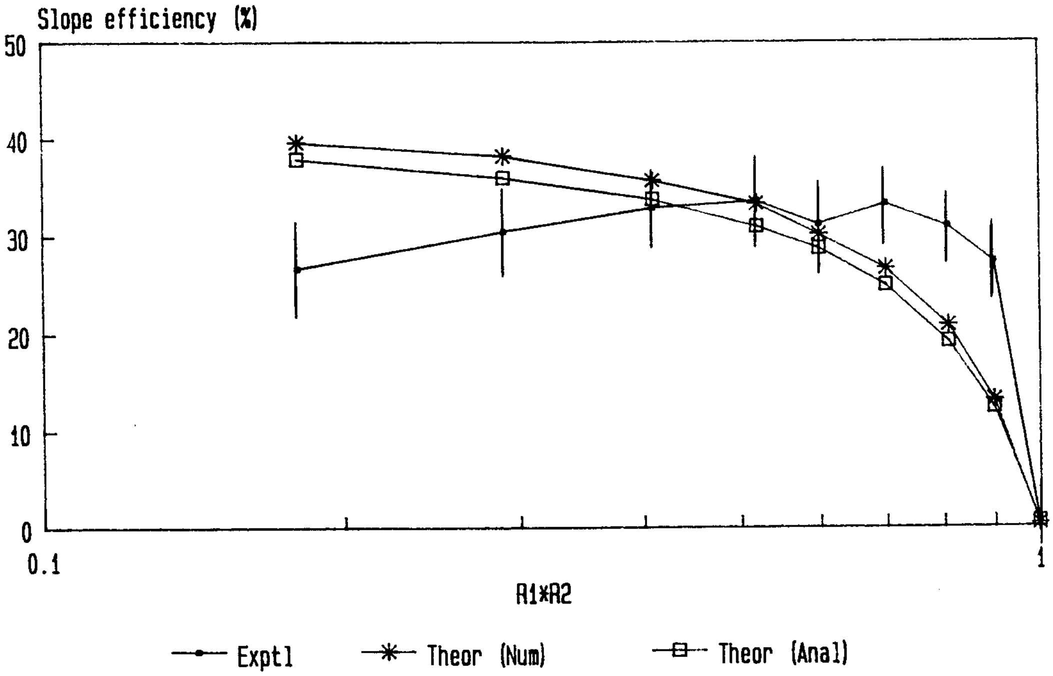

Figure 31. Experimental and theoretical CW fibre laser slope efficiency against output mirror reflectivity.

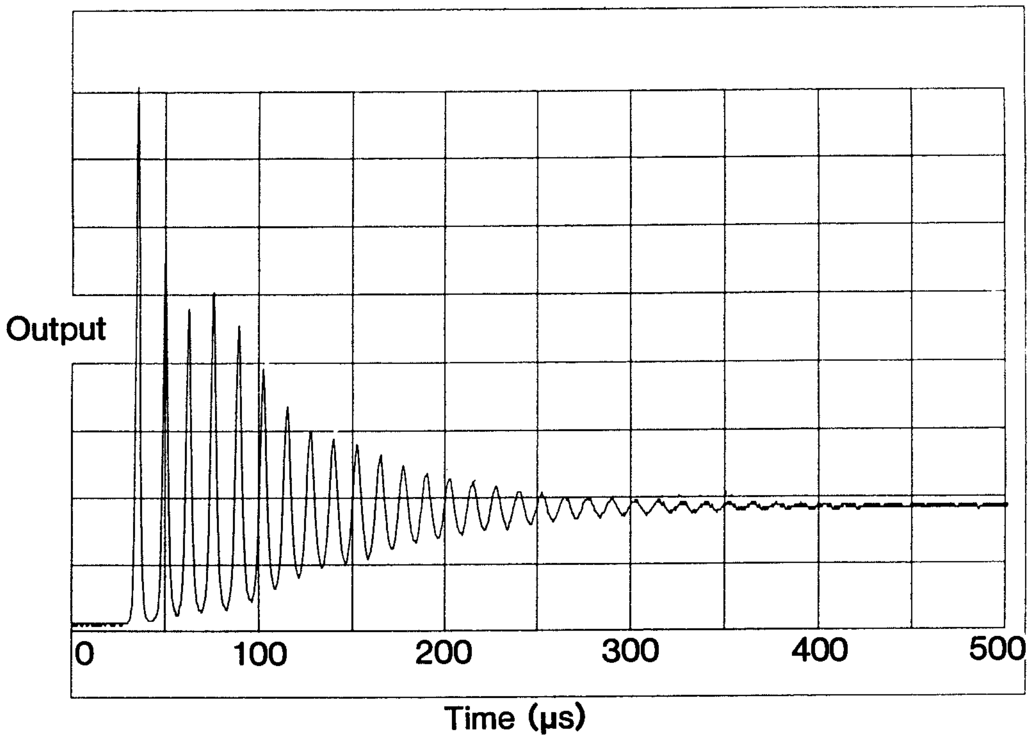

Figure 32. Experimental relaxation oscillation against time.

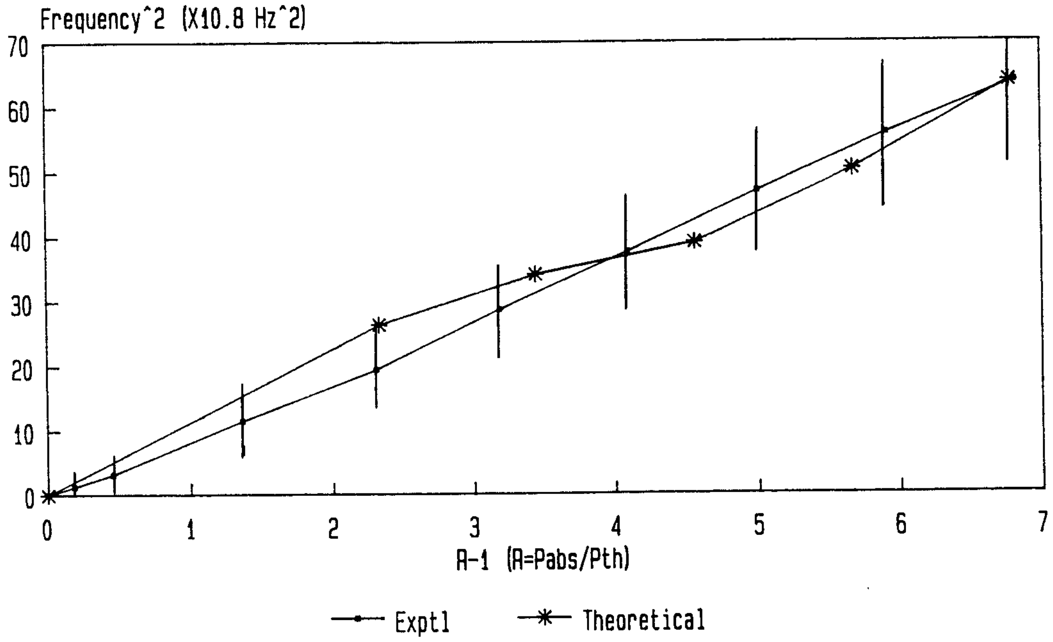

Figure 33. Experimental and theoretical relaxation oscillation frequency against pump power.

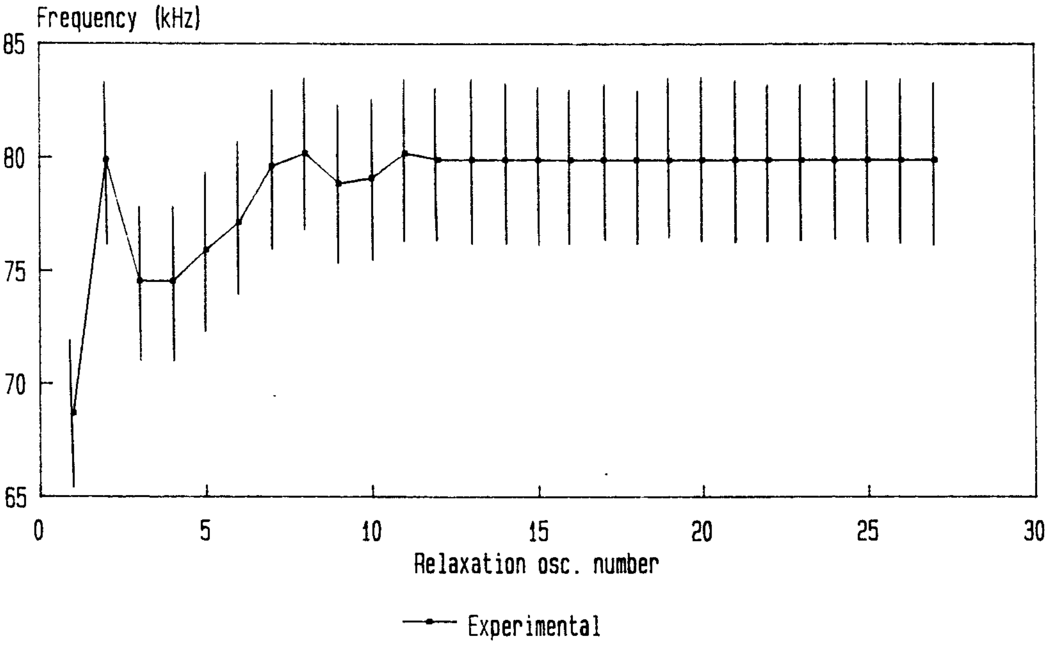

Figure 34. Experimental relaxation oscillation frequency against oscillation number.

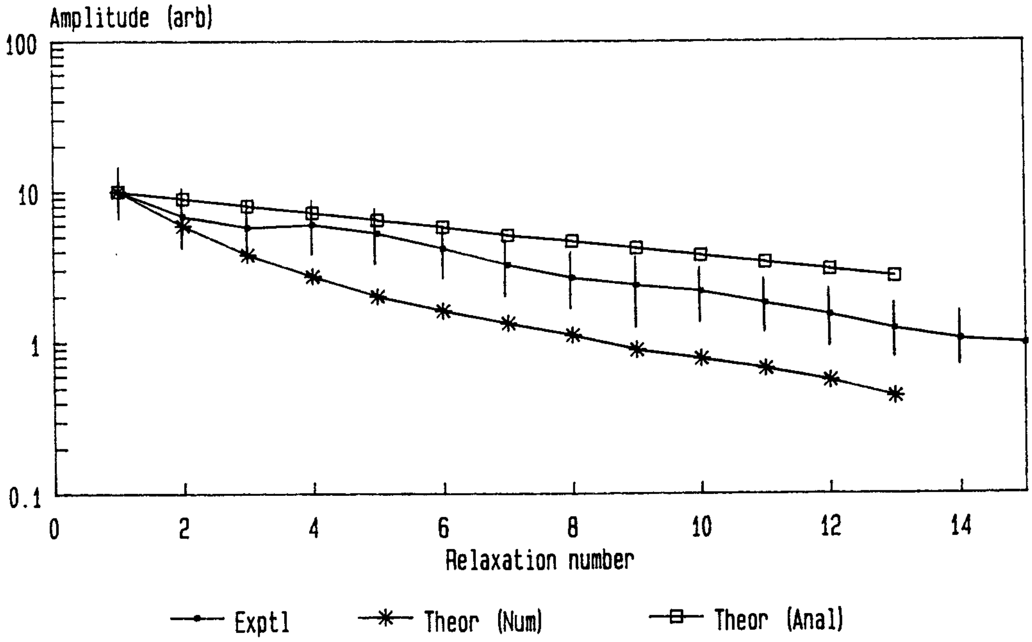

Figure 35. Experimental and theoretical relaxation oscillation magnitude against oscillation number.

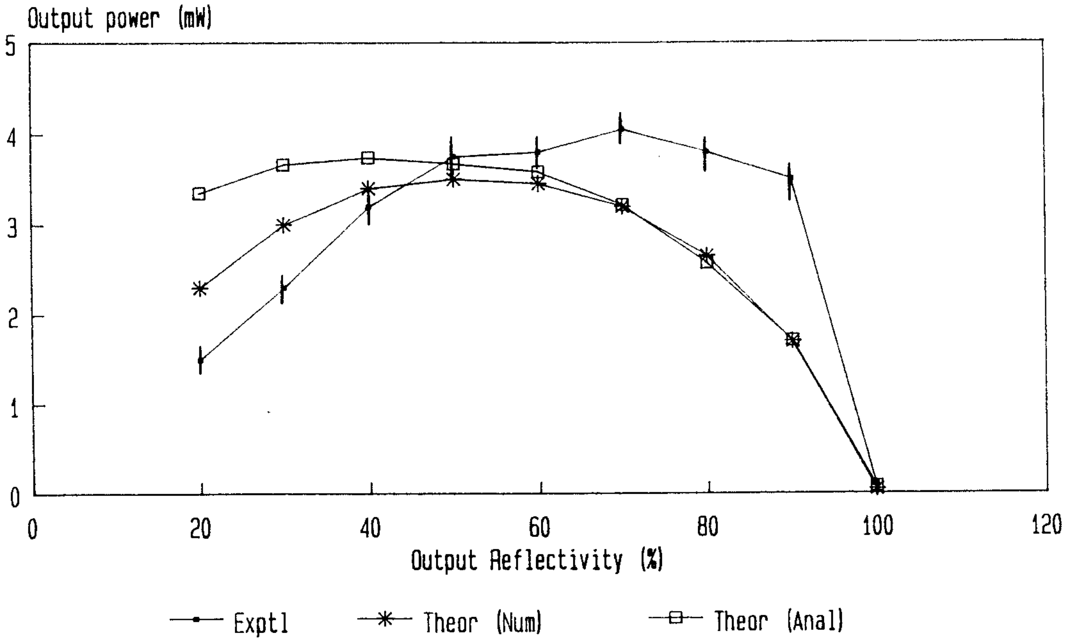

Figure 36. Theoretical and experimental CW output power against output mirror reflectivity for 15mW launched pump power, showing the concept of optimum output coupling.

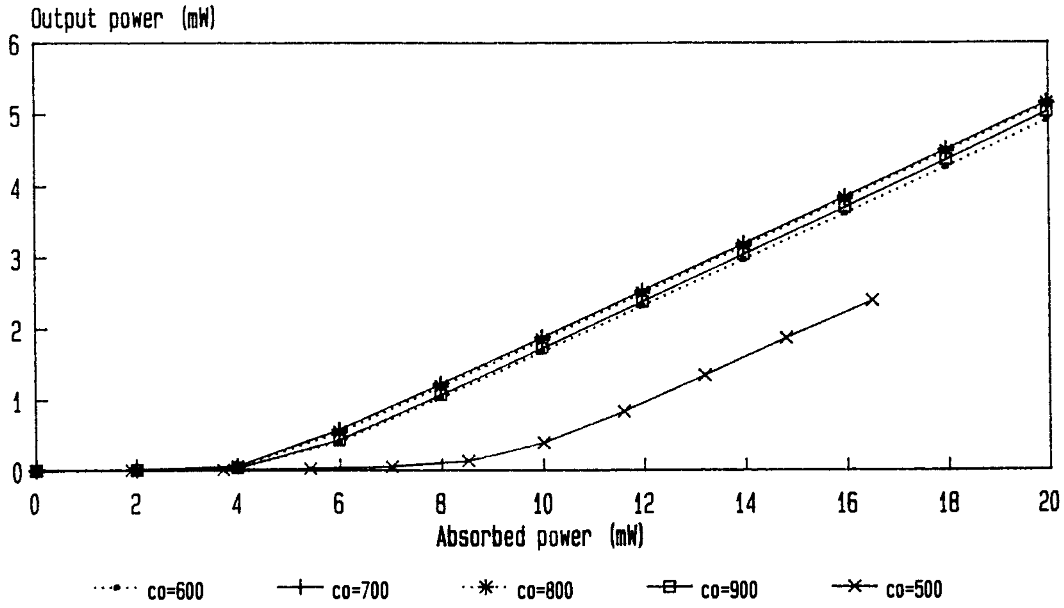

Figure 37. Theoretical CW lasing characteristic against fibre cut-off wavelength.

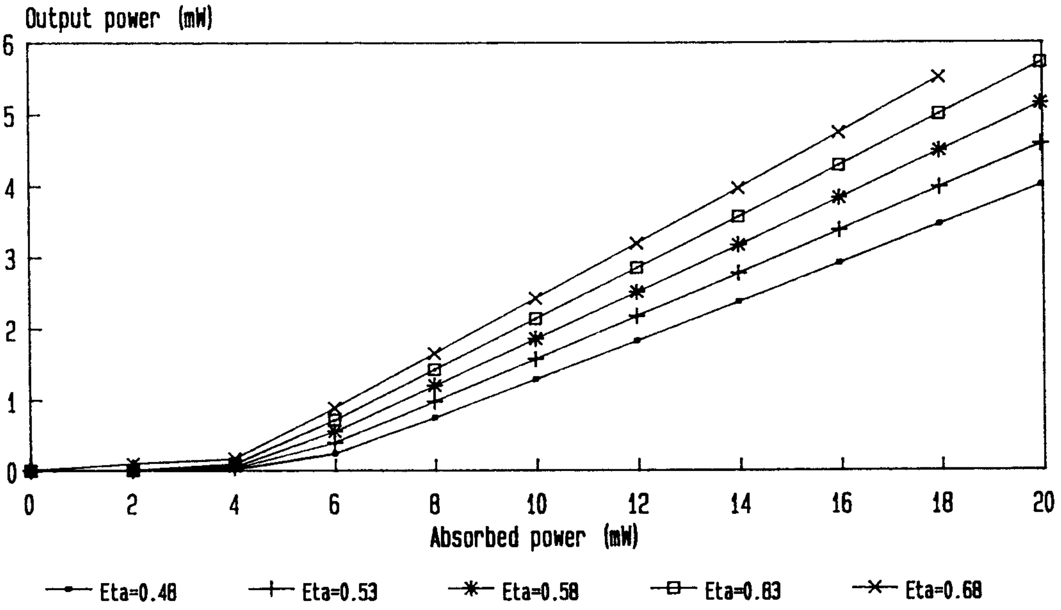

Figure 38. Theoretical CW lasing characteristic against eta.

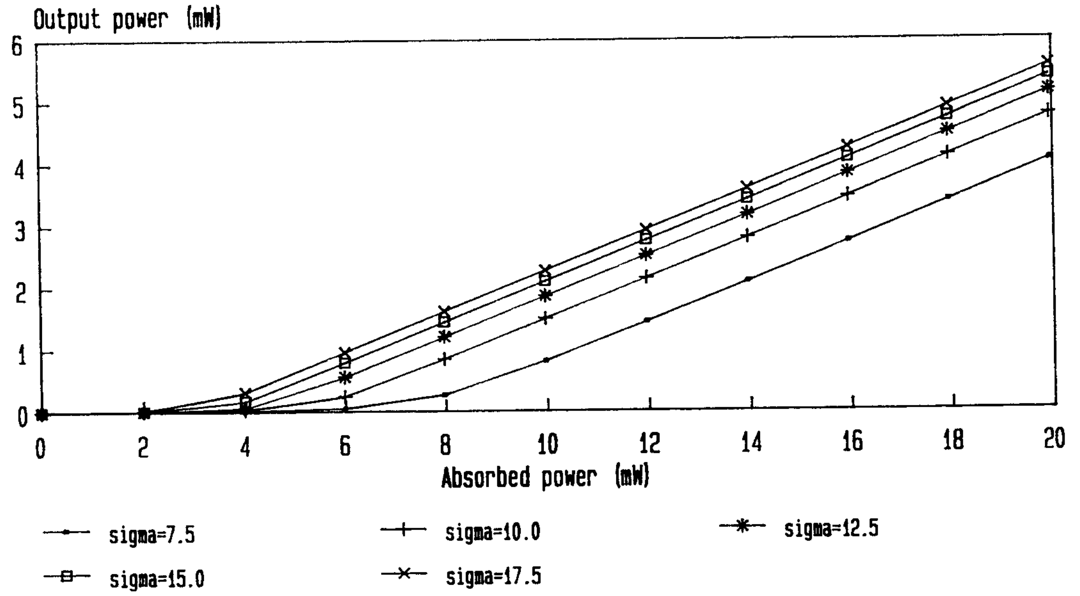

Figure 39. Theoretical CW lasing characteristic against stimulated emission cross section.

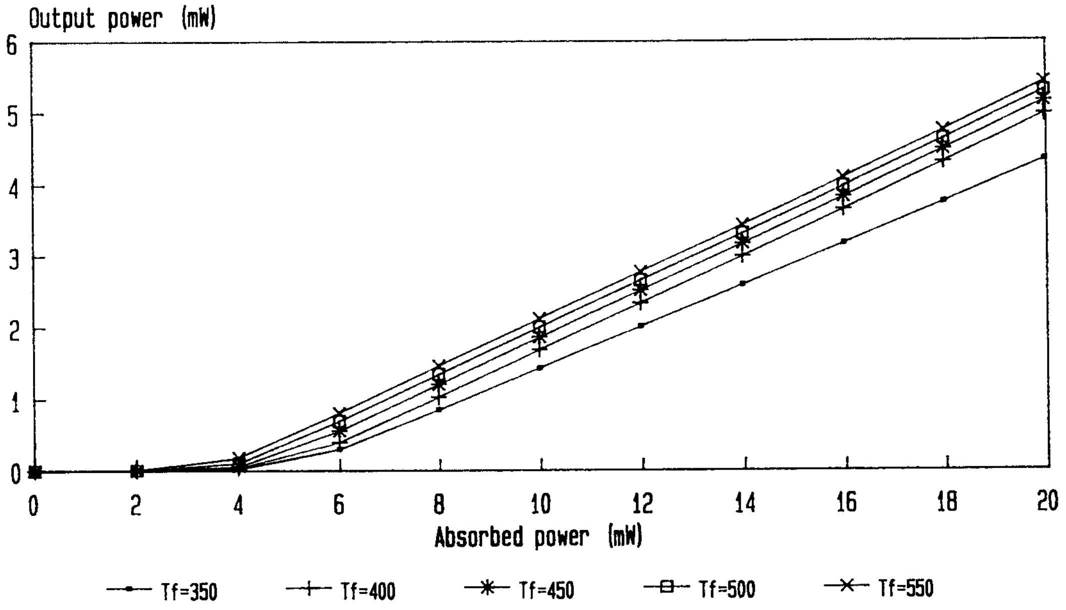

Figure 40. Theoretical CW lasing characteristic against fluorescence decay time.

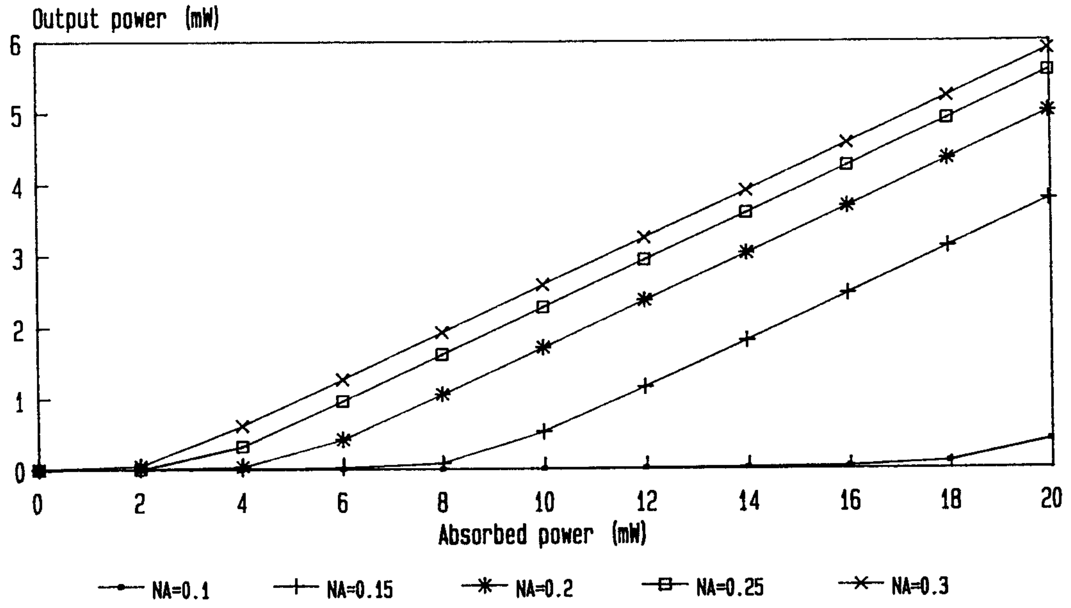

Figure 41. Theoretical CW lasing characteristic against fibre N.A.

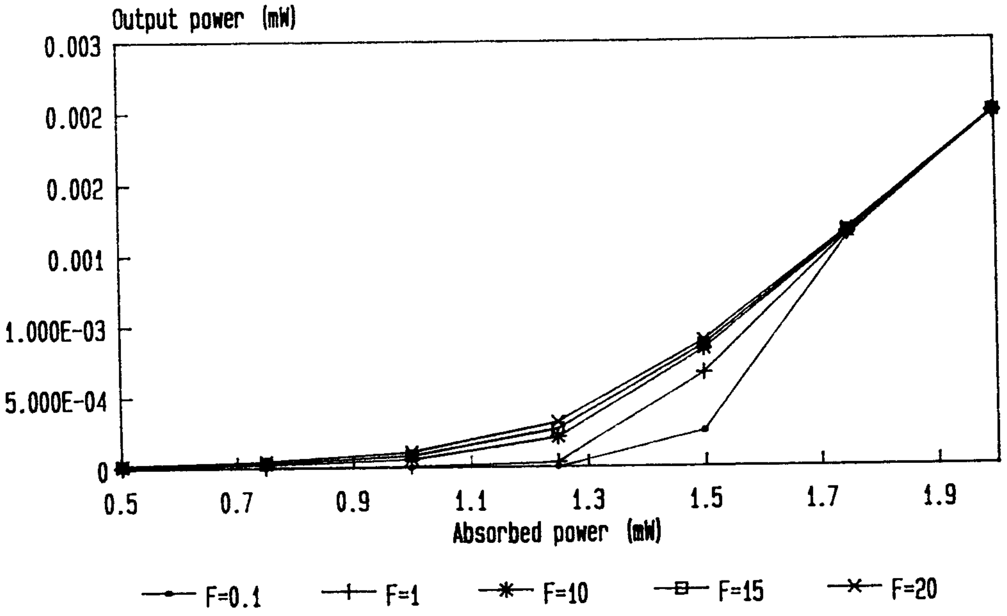

Figure 42. Theoretical CW lasing characteristic against capture fraction multiplier for a typical cavity.

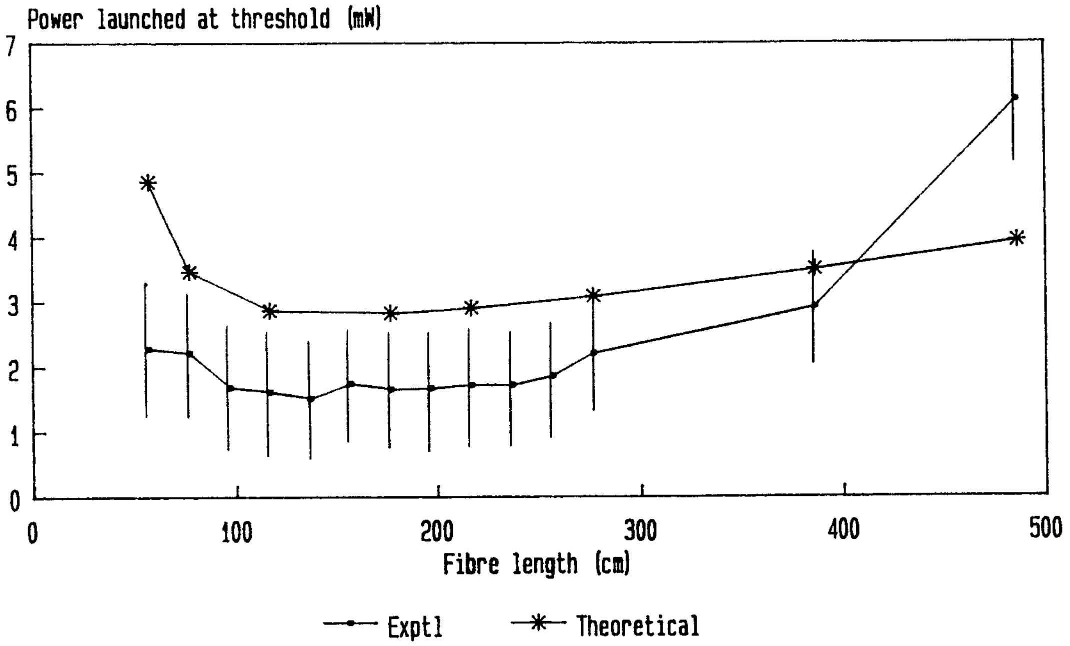

Figure 43. Experimental and theoretical threshold against fibre length for 3-level operation at 935nm.

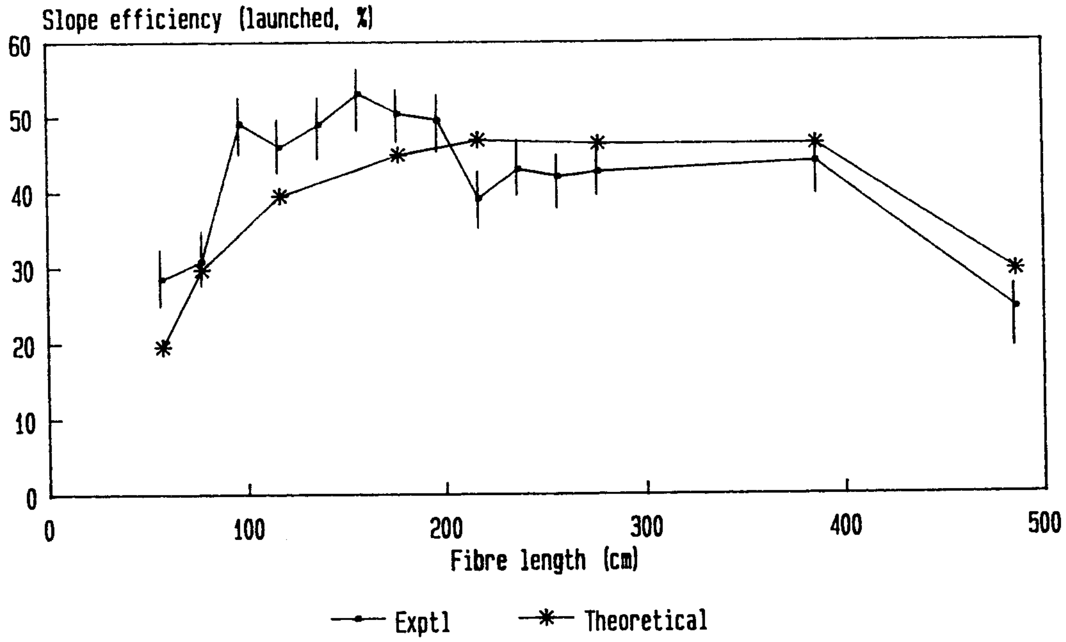

Figure 44. Experimental and theoretical CW slope efficiency against fibre length for 3-level operation at 935nm.

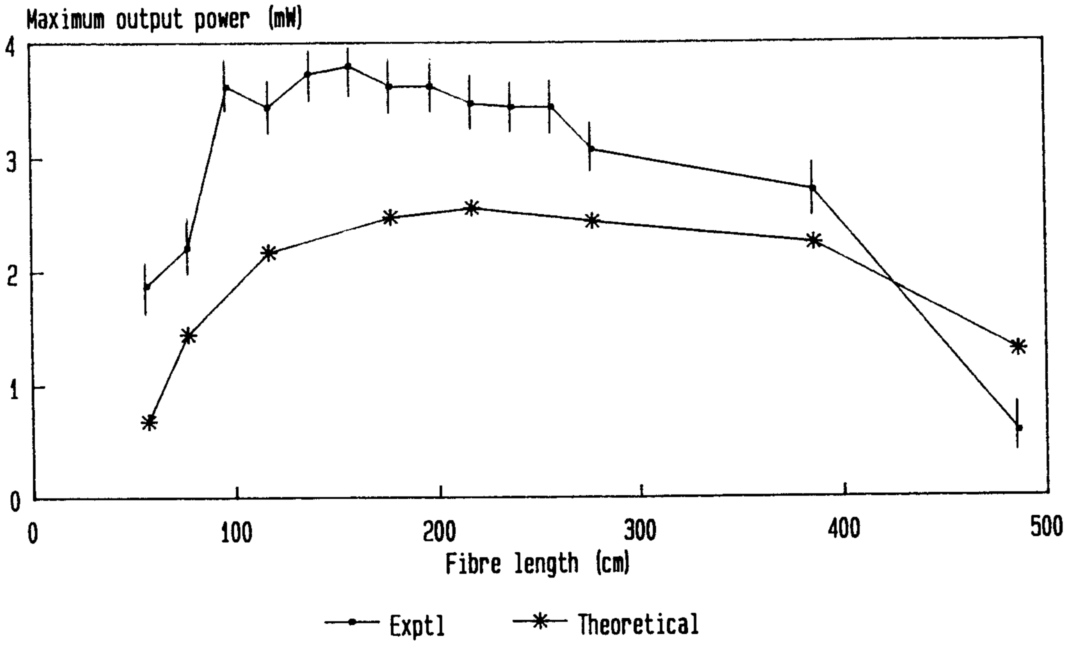

Figure 45. Experimental and theoretical CW output power against fibre length for 3-level operation at 935nm and 8.4mW launch pump power.

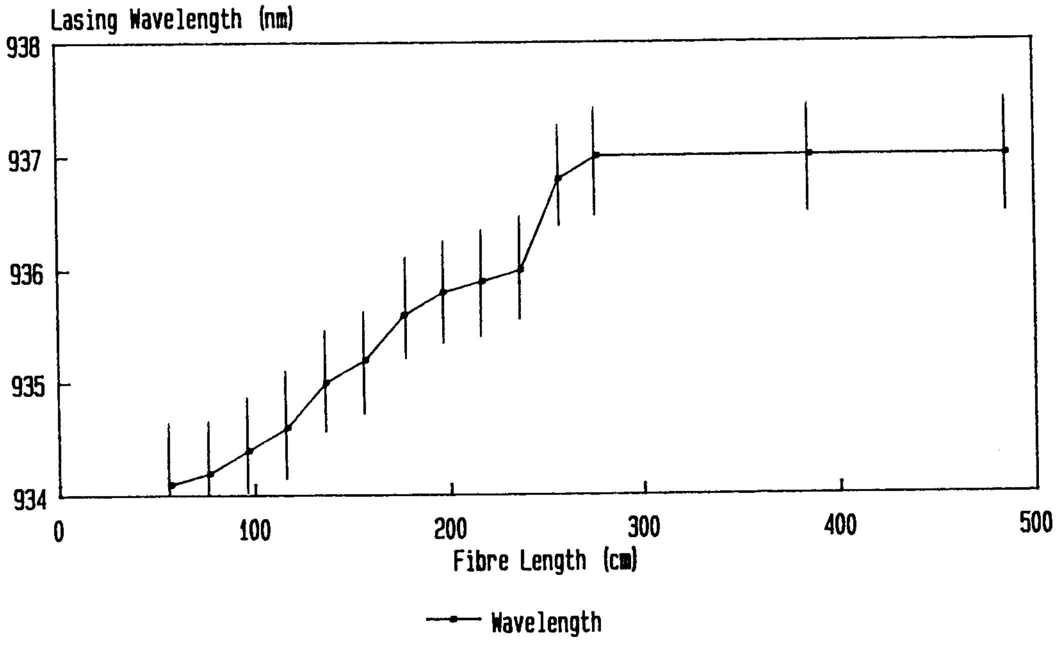

Figure 46. Experimental CW output wavelength against fibre length for 3-level operation around 935nm.

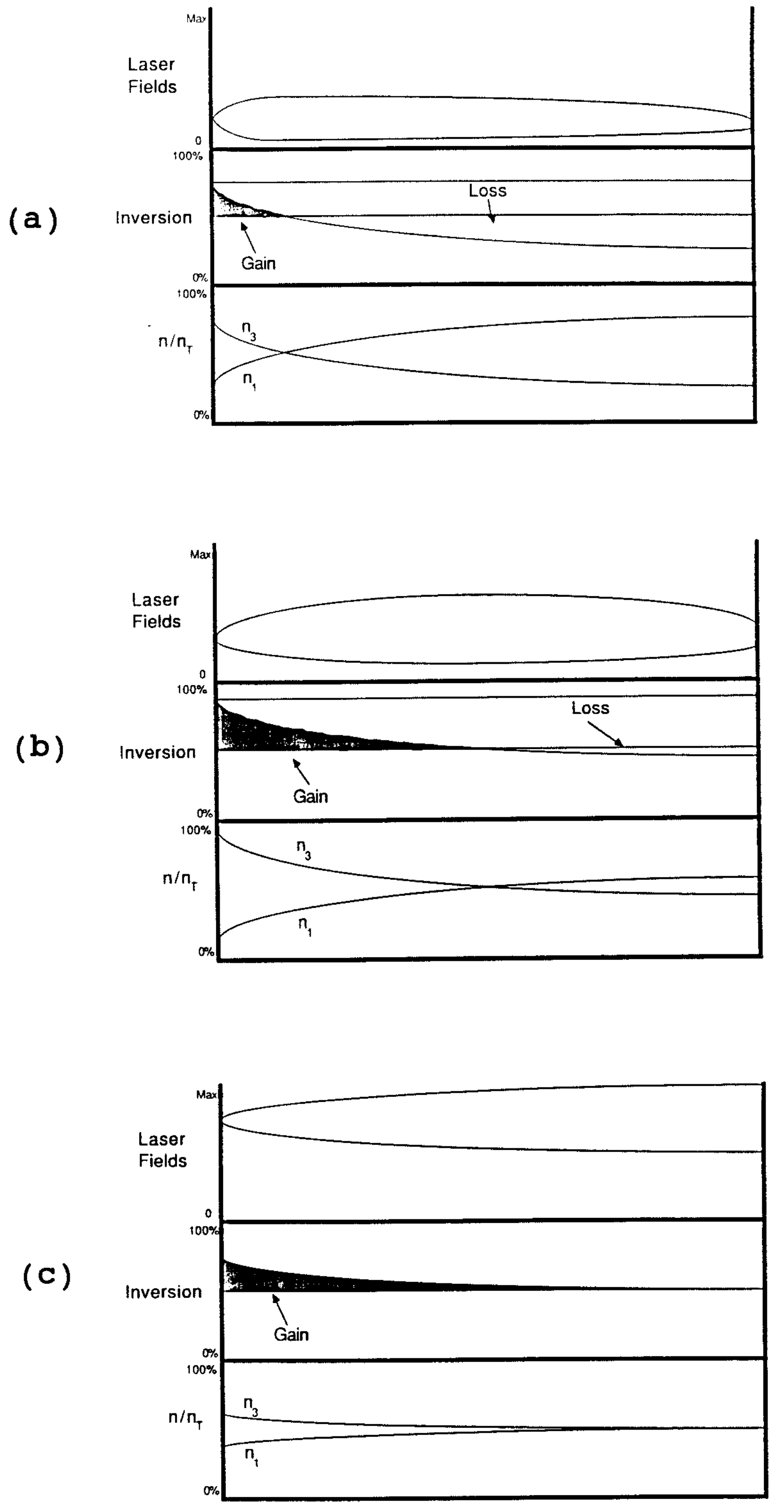

Figure 47. Theoretical plots of population densities and laser fields along fibre length for various pump powers around threshold.

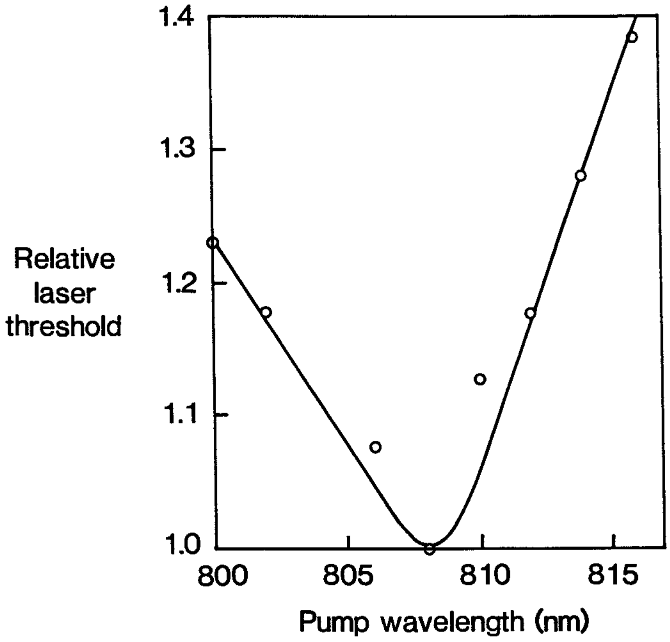

Figure 48. Experimental CW threshold against pump wavelength for Erbium-doped fibre operating around 1600nm.

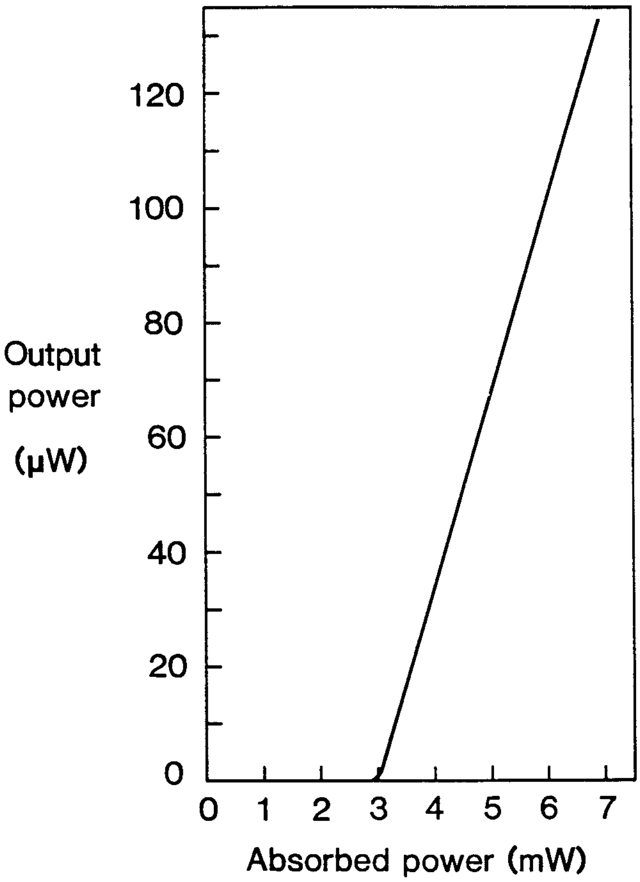

Figure 49. Experimental CW lasing characteristic for Erbium-doped fibre laser.

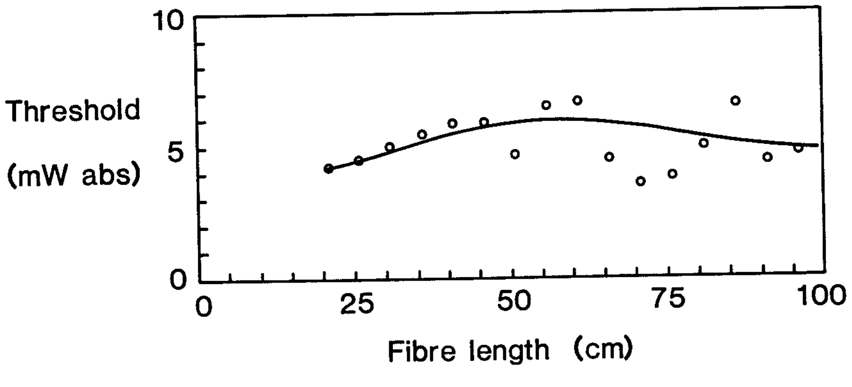

Figure 50. Experimental CW lasing threshold against fibre length for Erbium-doped fibre.

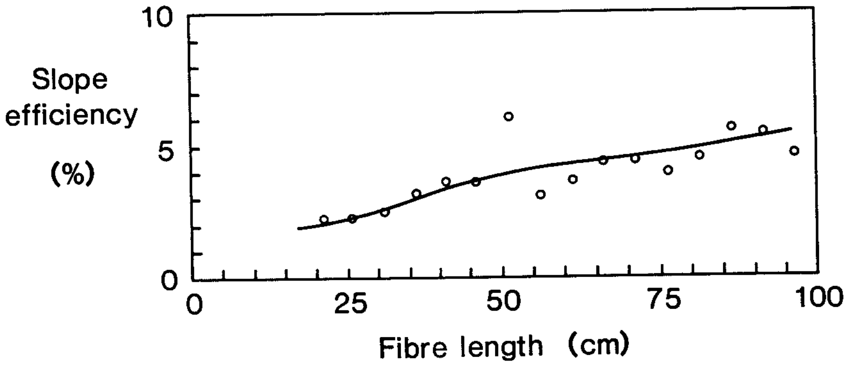

Figure 51. Experimental CW lasing slope efficiency against fibre length for Erbium-doped fibre.

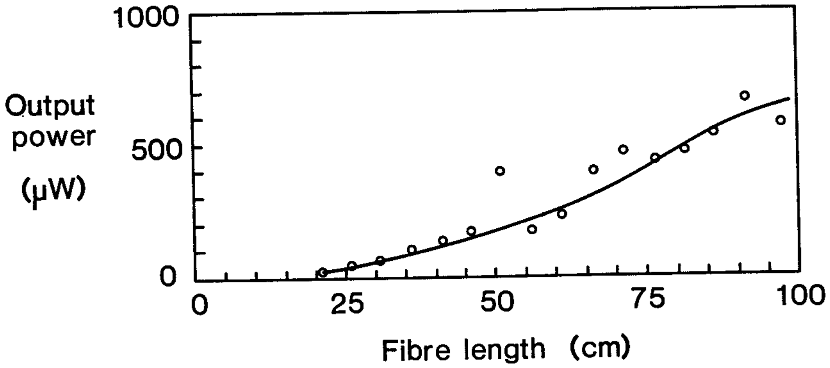

Figure 52. Experimental CW maximum output power against fibre length for Erbium-doped fibre laser and 26mW pump.

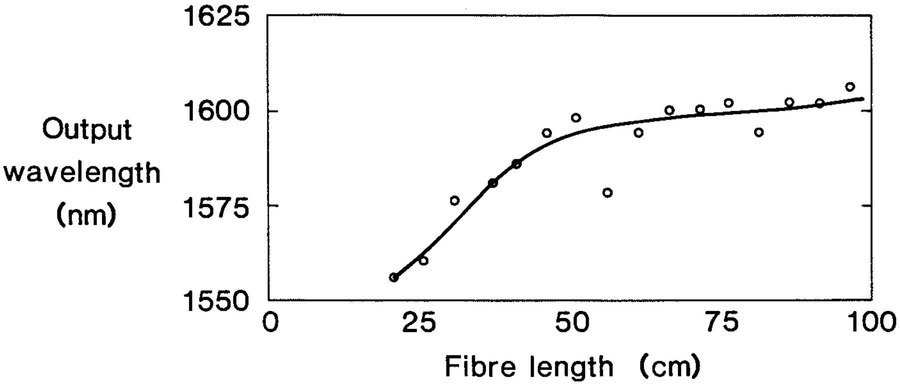

Figure 53. Experimental CW output wavelength against fibre length for Erbium-doped fibre laser.

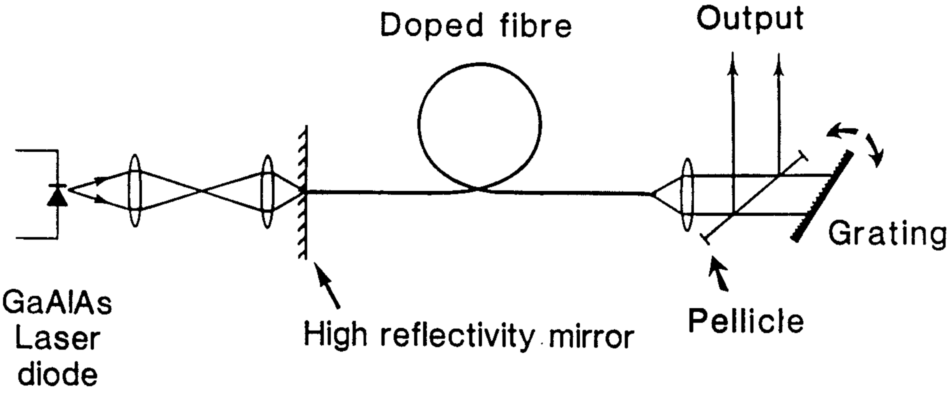

Figure 54. Experimental set up employed to construct a tunable fibre laser.

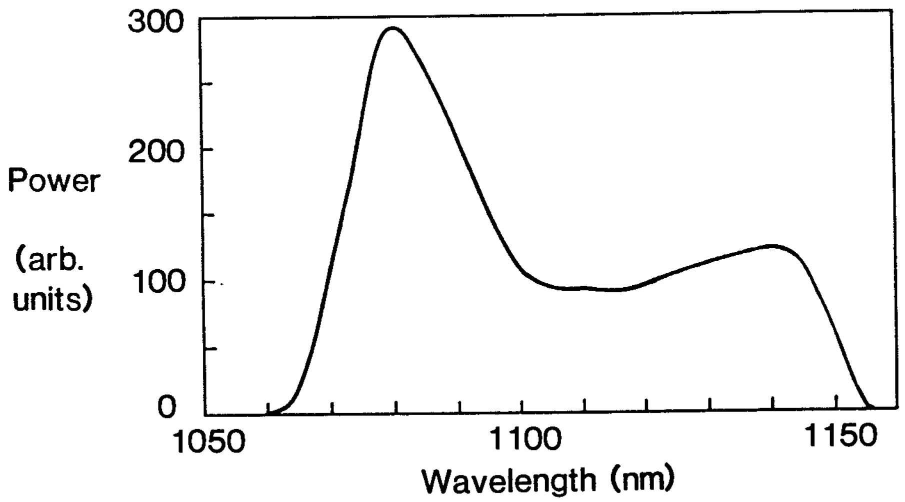

Figure 55. Experimental output tuning spectrum for Neodymium-doped fibre laser operating around 1088nm.

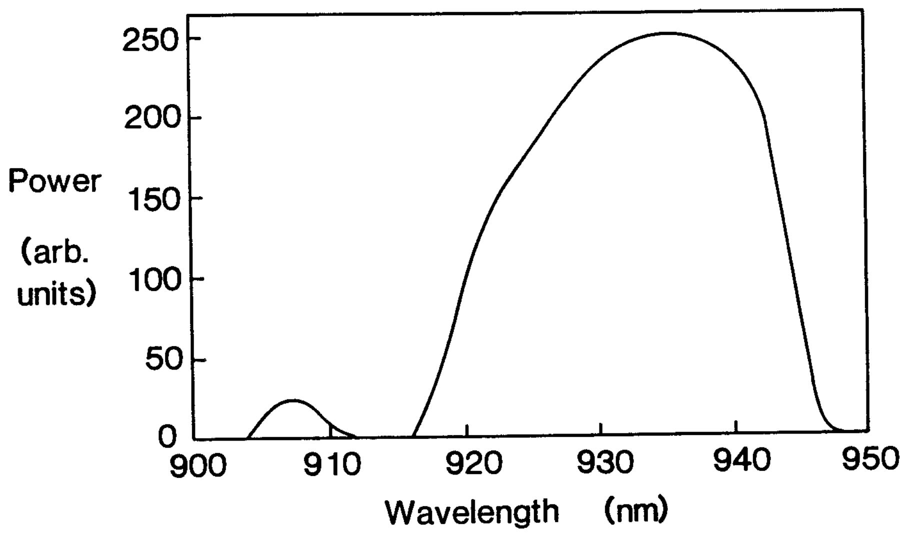

Figure 56. Experimental output tuning spectrum for Neodymium-doped fibre laser operating around 935nm.

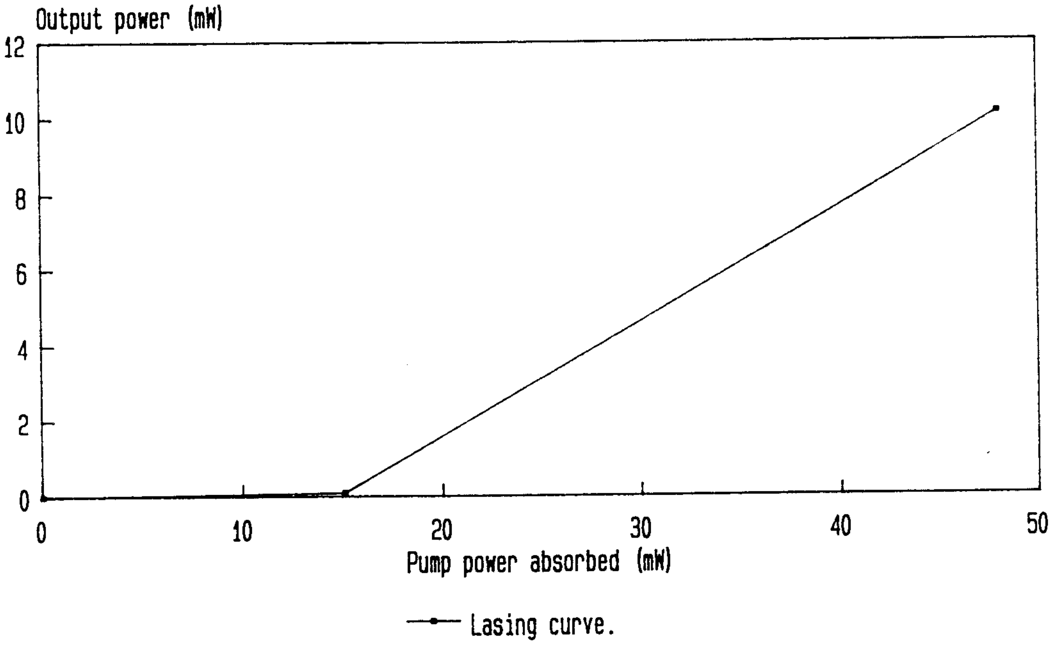

Figure 57. Experimental CW lasing characteristic for Neodymium-doped offset core fibre laser.

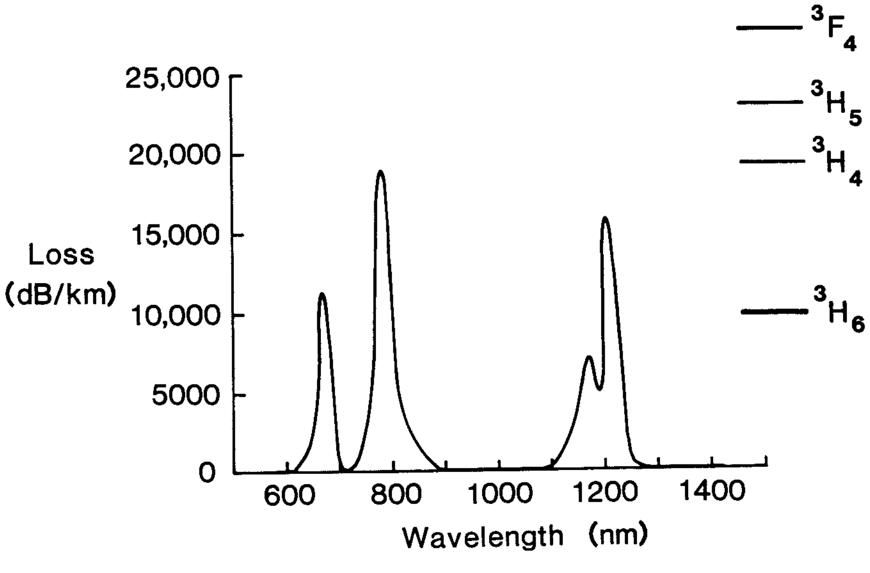

Figure 58. Experimental attenuation spectrum for Thulium-doped fibre.

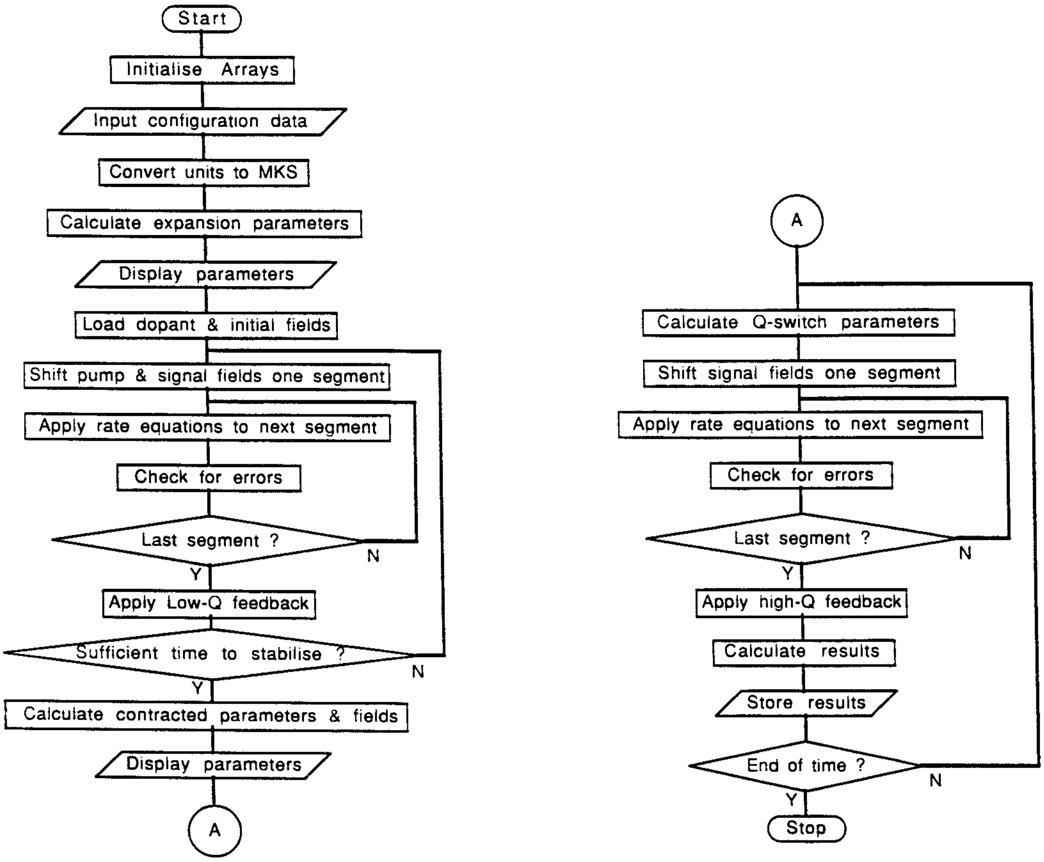

Figure 59. FORTRAN program QSW2.F77 flow chart.

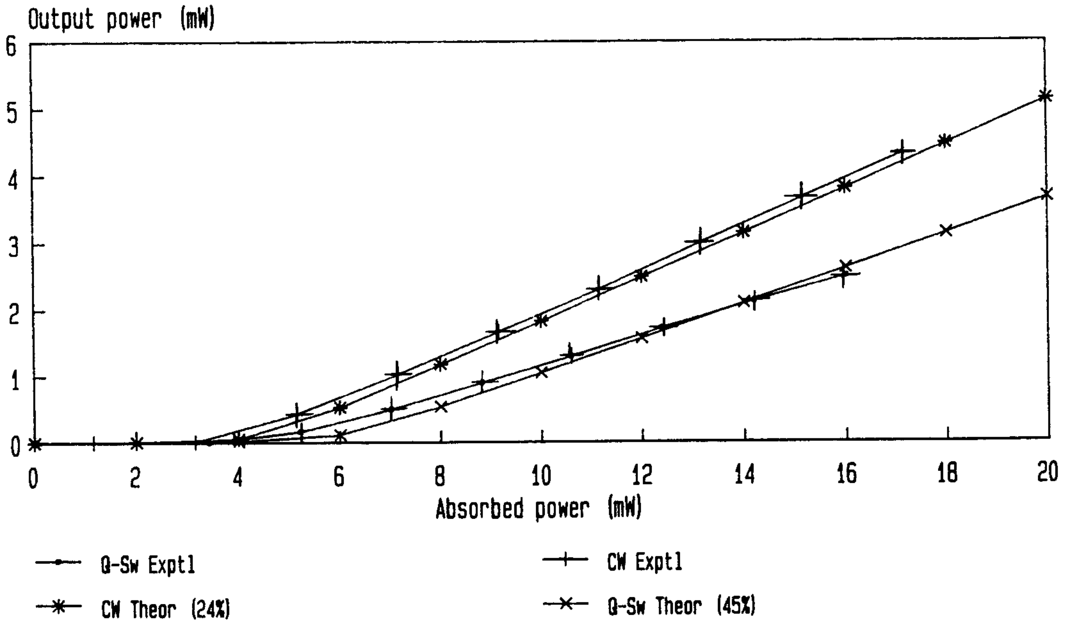

Figure 60. Experimental and theoretical CW laser characteristics employed to determine insertion loss of various A.O.D.'s.

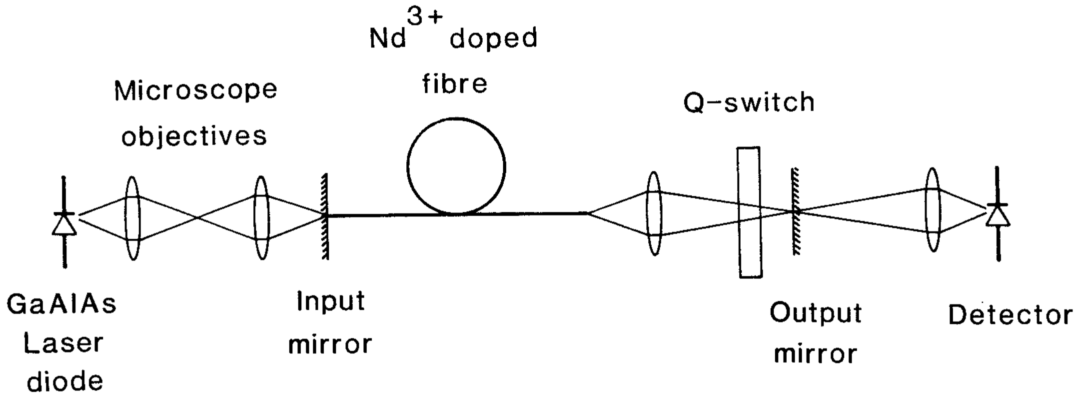

Figure 61. Experimental setup employed to investigate Q-switched fibre laser behaviour.

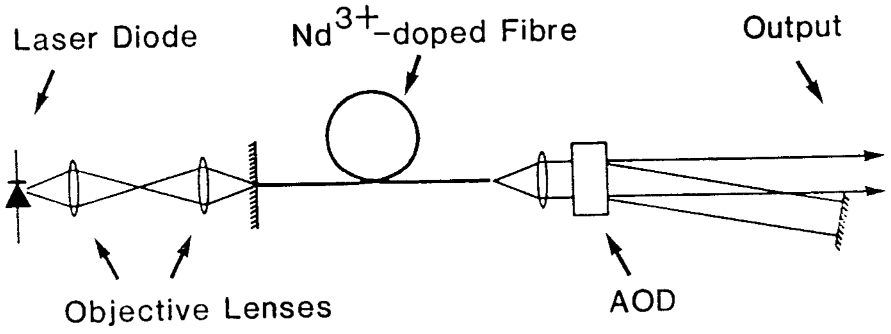

Figure 62. Alternative experimental setup employed to investigate Q-switched fibre laser behaviour.

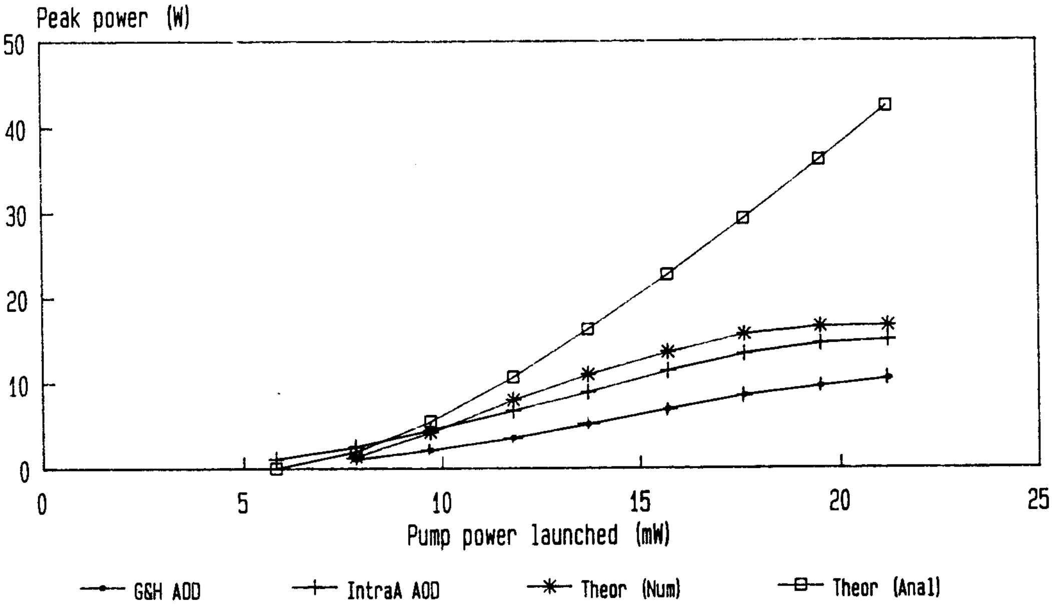

Figure 63. Experimental and theoretical Q-switched pulse peak power against pump power.

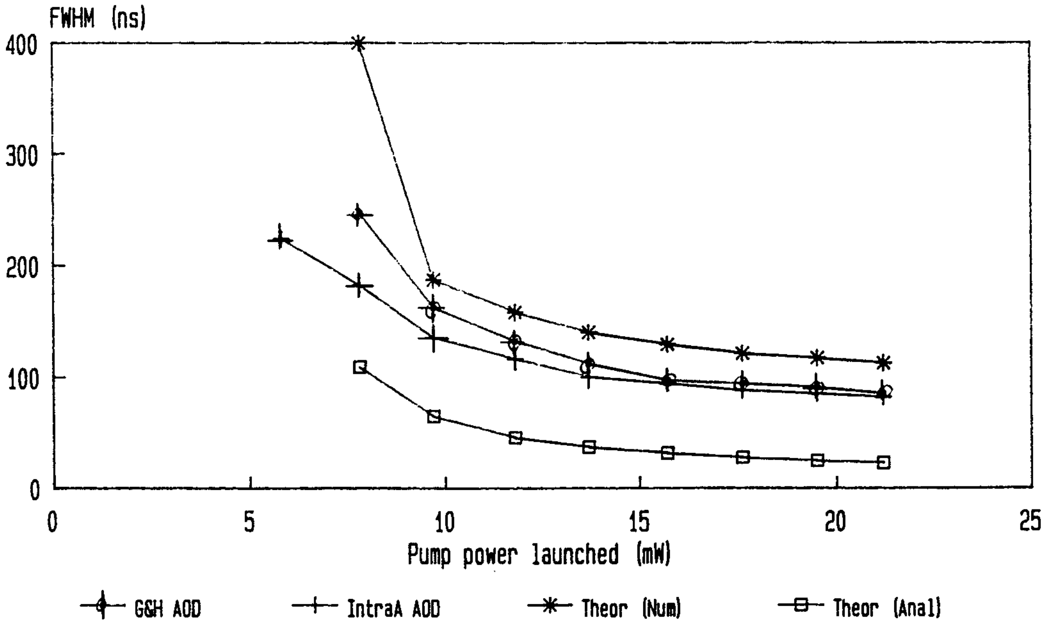

Figure 64. Experimental and theoretical Q-switched pulse FWHM against pump power.

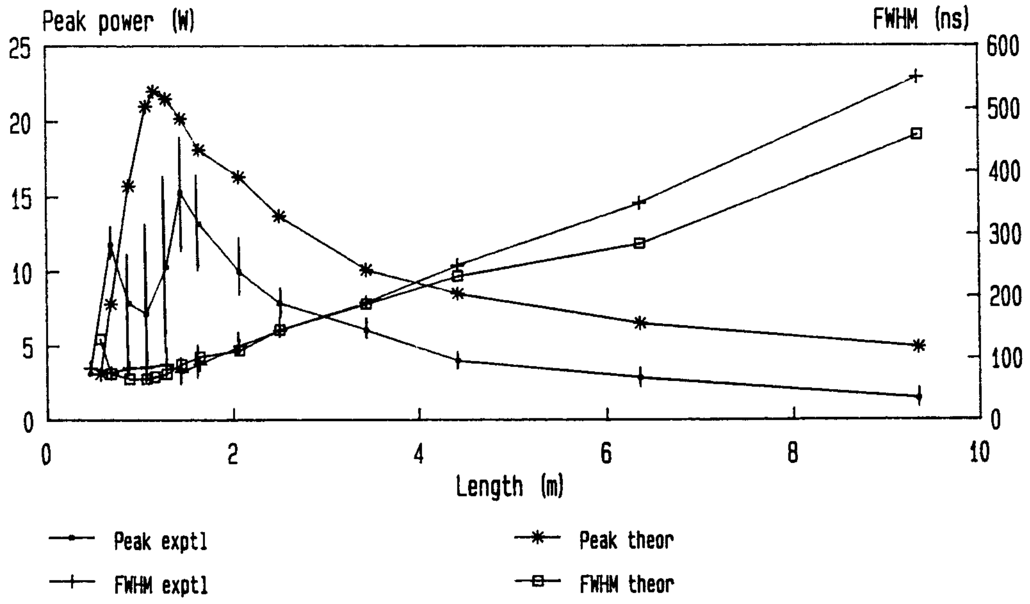

Figure 65. Experimental and theoretical Q-switched pulse characteristics against fibre length.

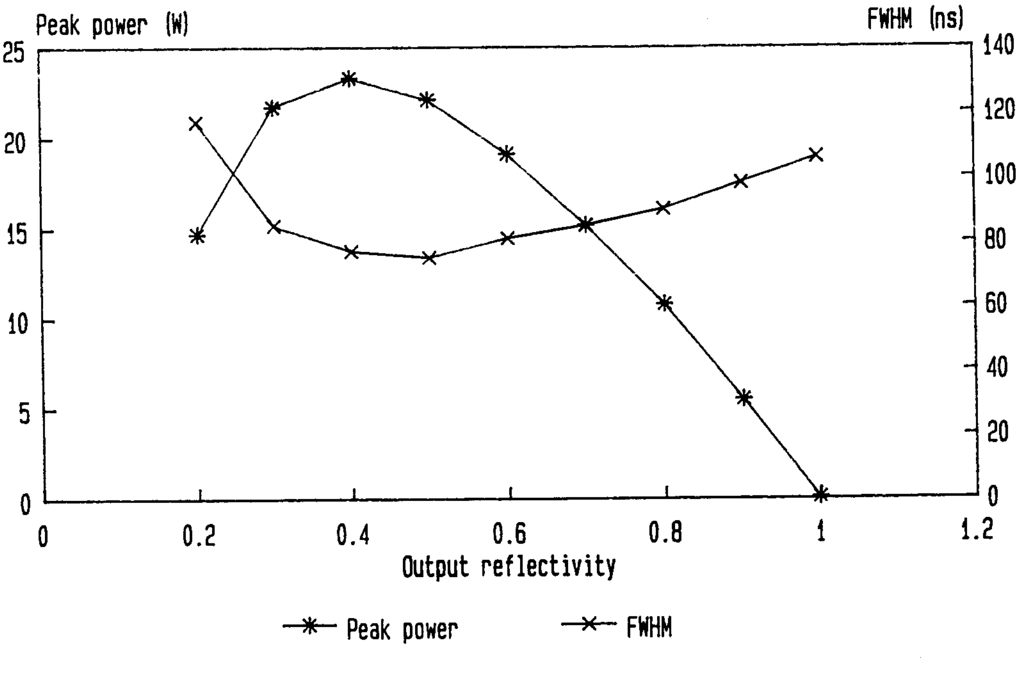

Figure 66. Theoretical Q-switched pulse characteristics against output mirror reflectivity.

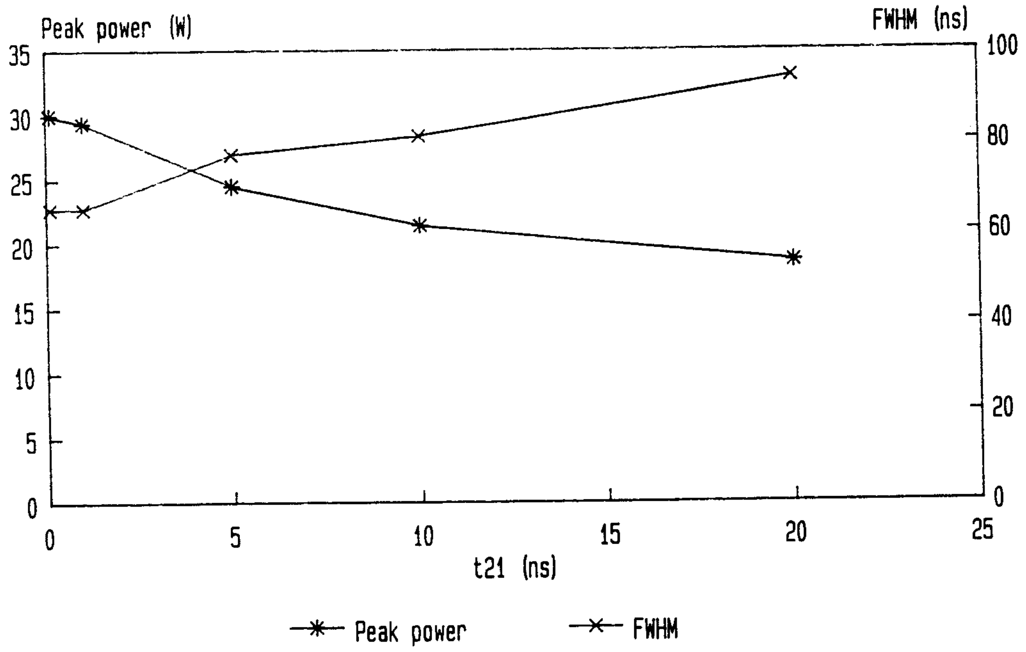

Figure 67. Theoretical Q-switched pulse characteristics against lower laser level decay time.

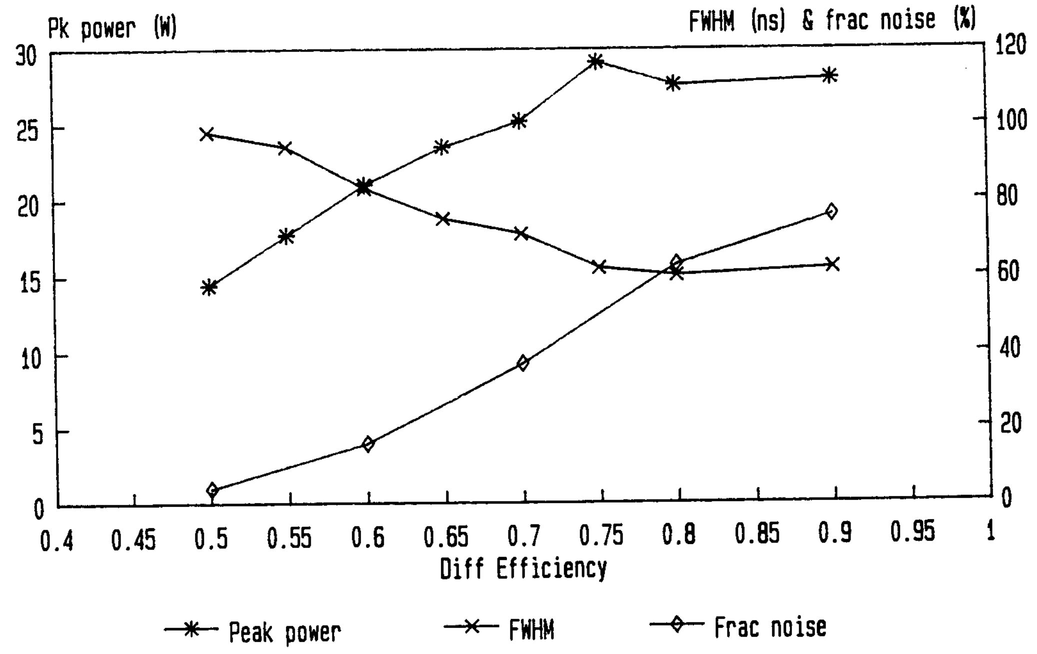

Figure 68. Theoretical Q-switched pulse characteristics against AOD diffraction efficiency, including relative noise spike magnitude.

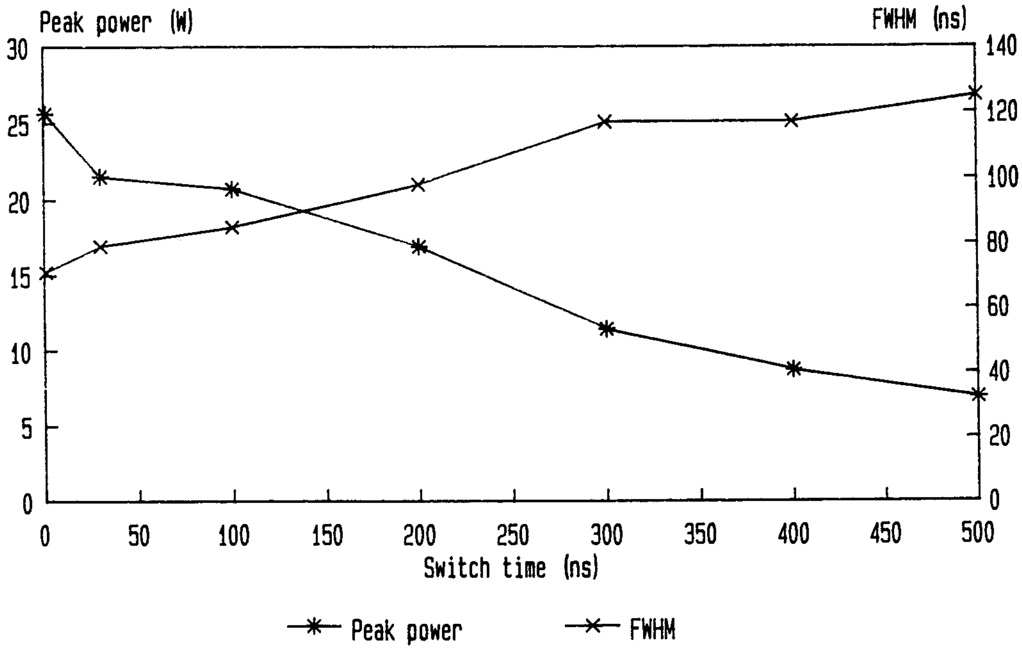

Figure 69. Theoretical Q-switched pulse characteristics against AOD switching time.

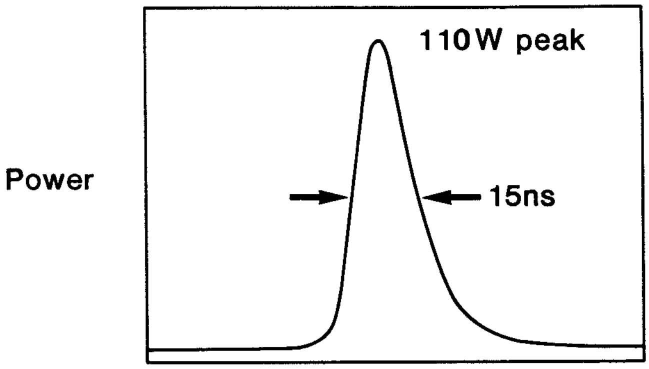

Fibre length: 17cm
Pump power: 17mW

Figure 70. Experimental Q-switched pulse showing 110W peak power.

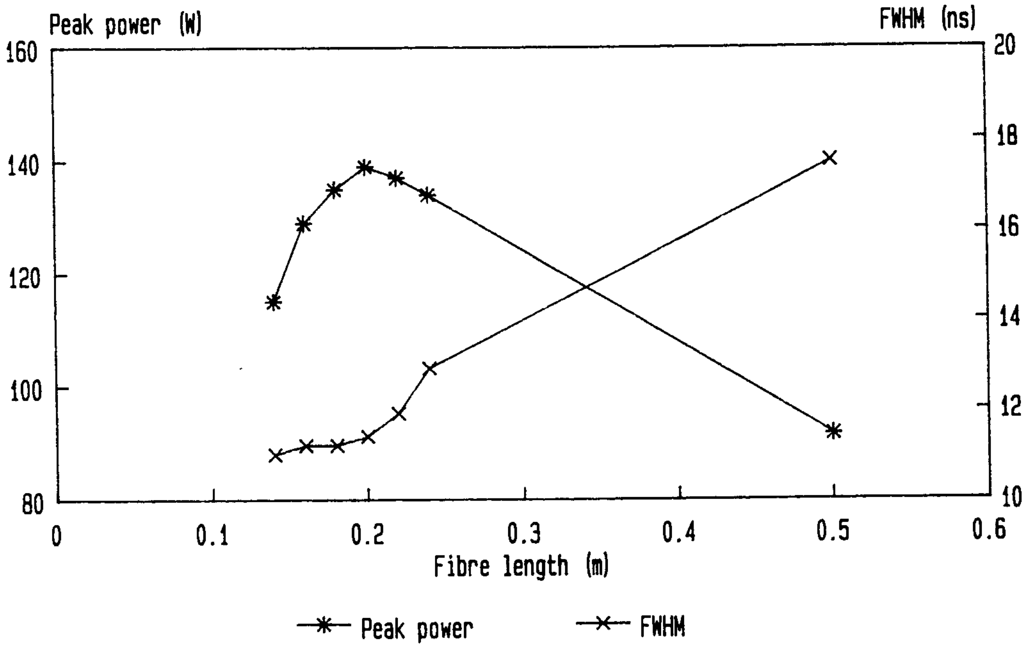

Figure 71. Theoretical Q-switched pulse characteristics against fibre length for alumina co-doped fibre.

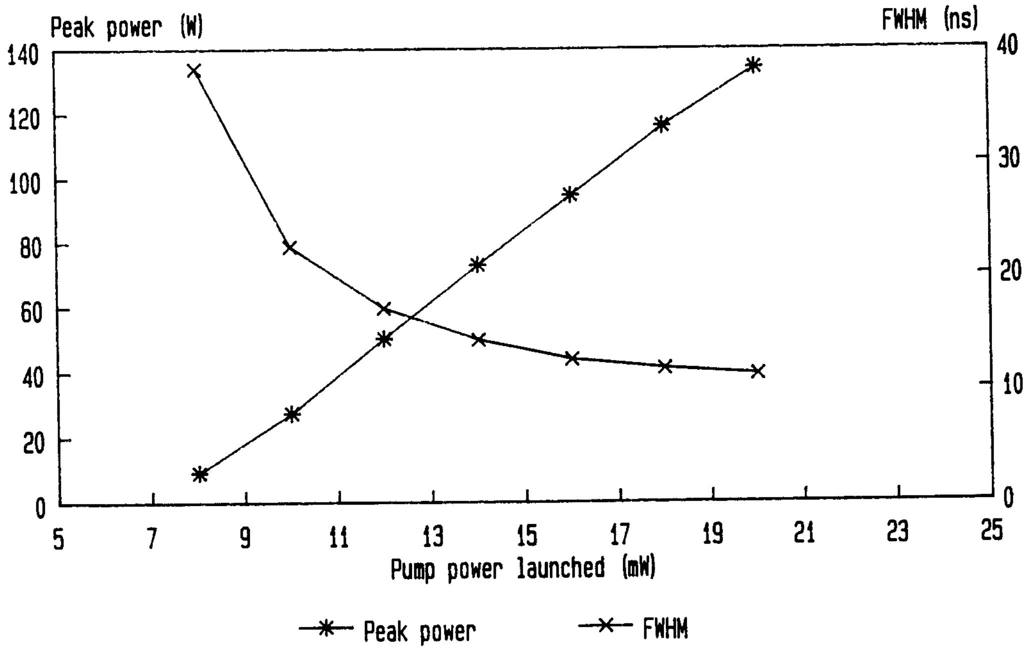

Figure 72. Theoretical Q-switched pulse characteristics against pump power for alumina co-doped fibre.

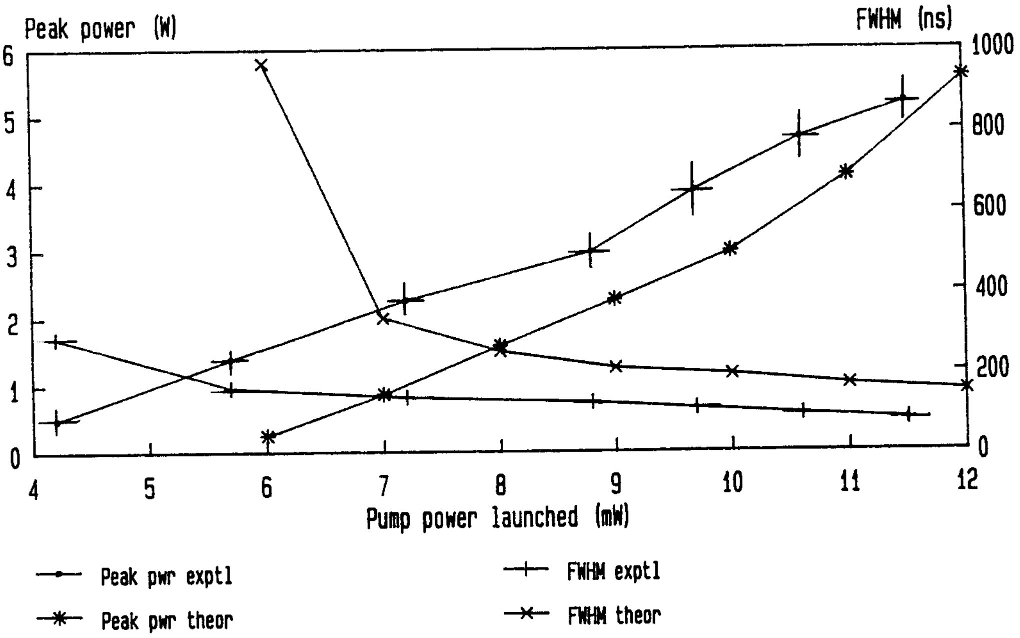

Figure 73. Experimental and theoretical Q-switched pulse characteristics against pump power for 3-level operation around 935nm.

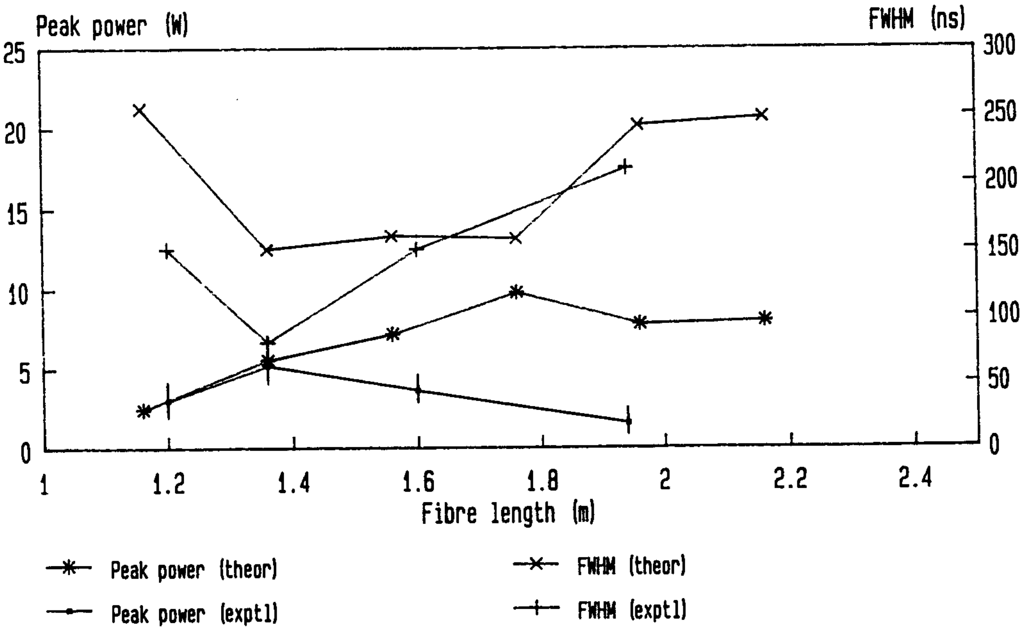

Figure 74. Experimental and theoretical Q-switched pulse characteristics against fibre length for 3-level operation around 935nm.

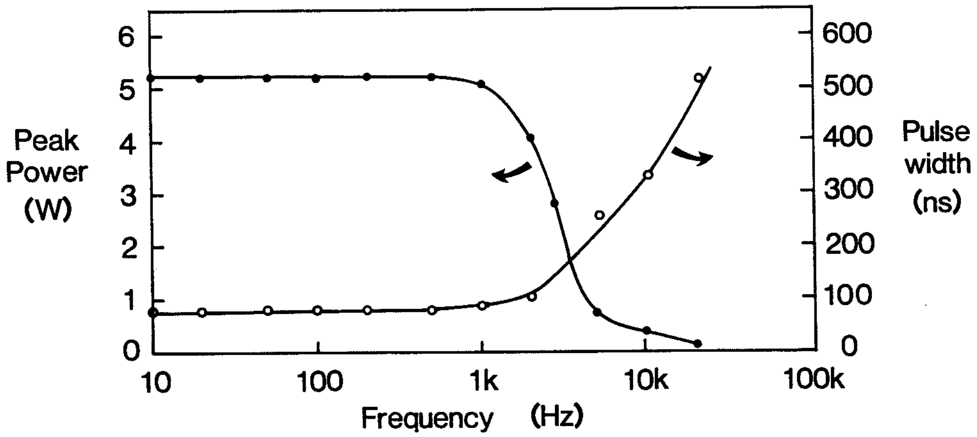

Figure 75. Experimental Q-switched pulse characteristics against repetition frequency for 3-level operation around 935nm.

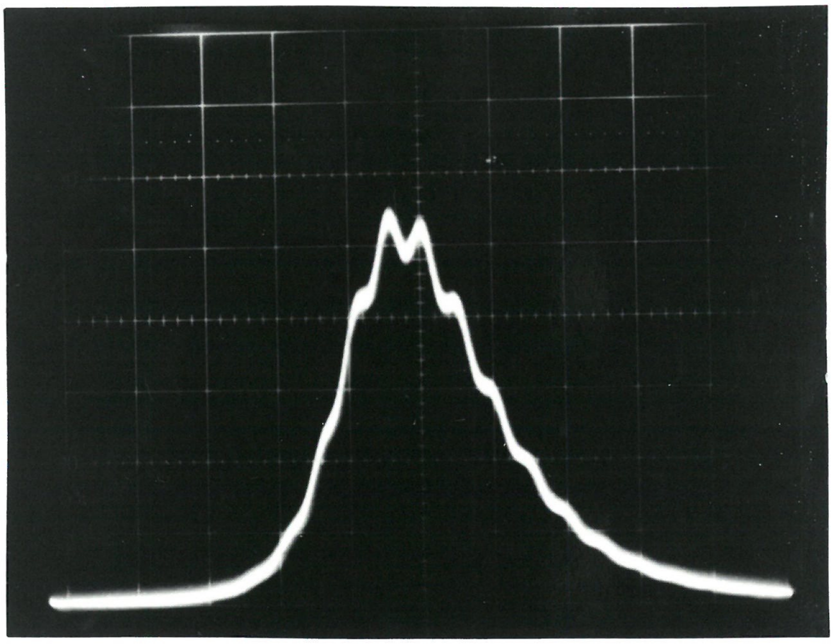

Fig.76 Experimental Q-switched pulse showing distinctive noise spikes.

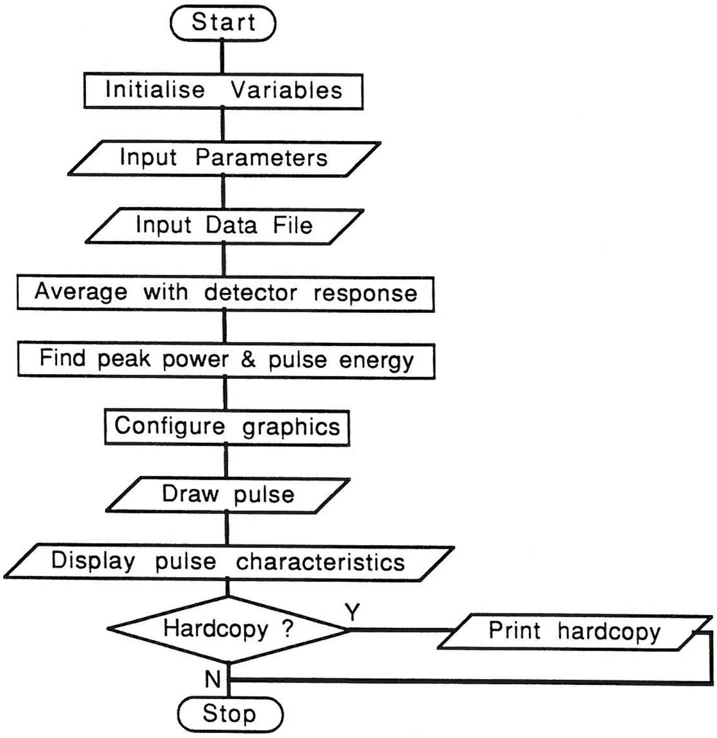

Figure 77. PASCAL program PLOT1.PAS flow chart.

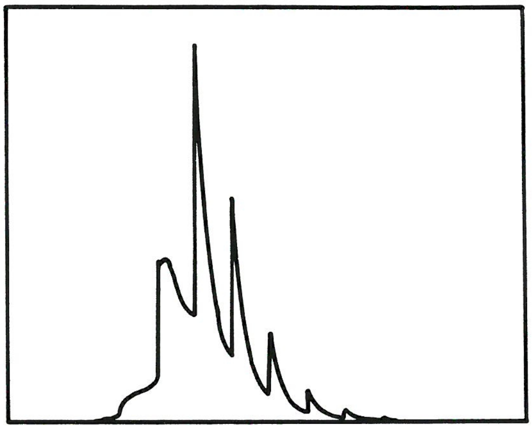

(a) Response time = 0.3ns

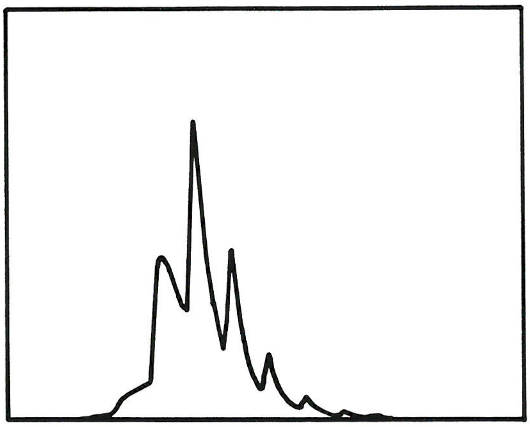

(b) Response time = 2ns

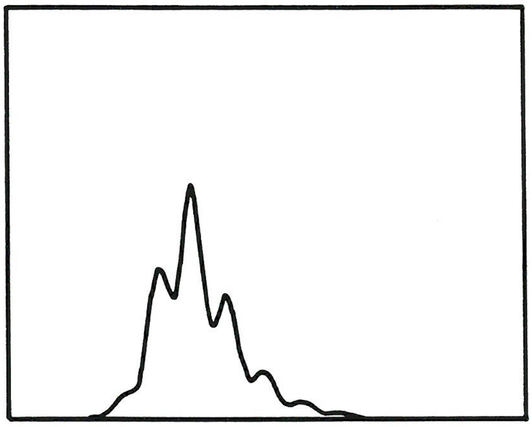

(c) Response time = 5ns

Figure 78. Theoretical Q-switched pulse profiles for various detector response times. These plots can be compared to Figure 76.

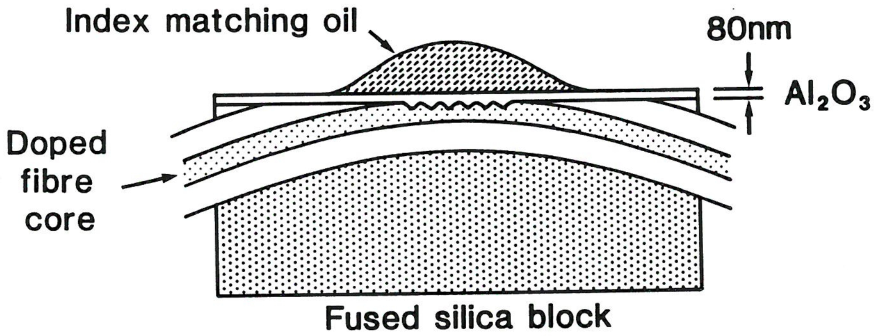

Figure 79. Structure of all-fibre Bragg grating reflector.

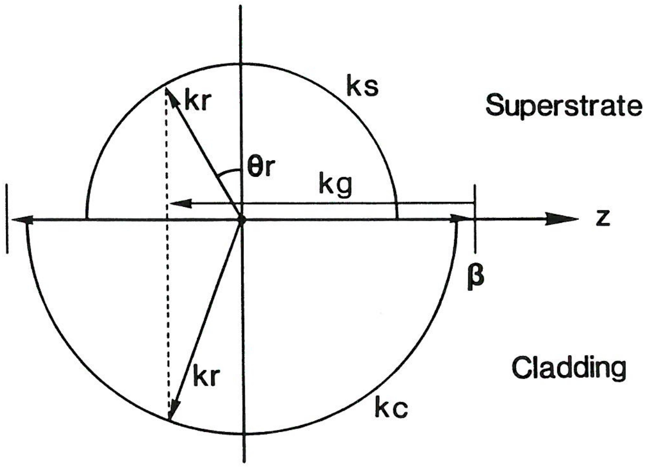

Figure 80. Vector diagram of grating operation showing radiated fields.

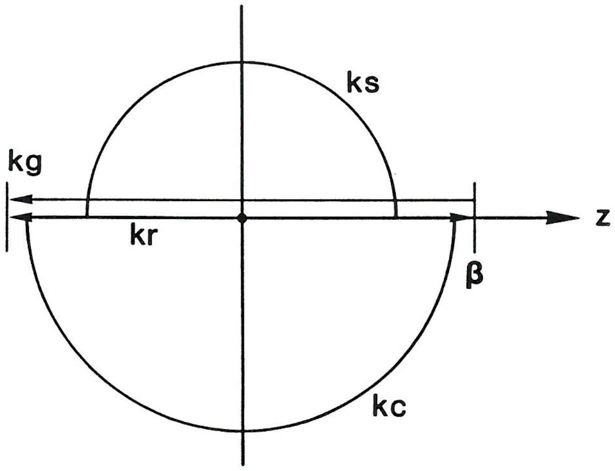

Figure 81. Vector diagram of grating operation showing reflected fields.

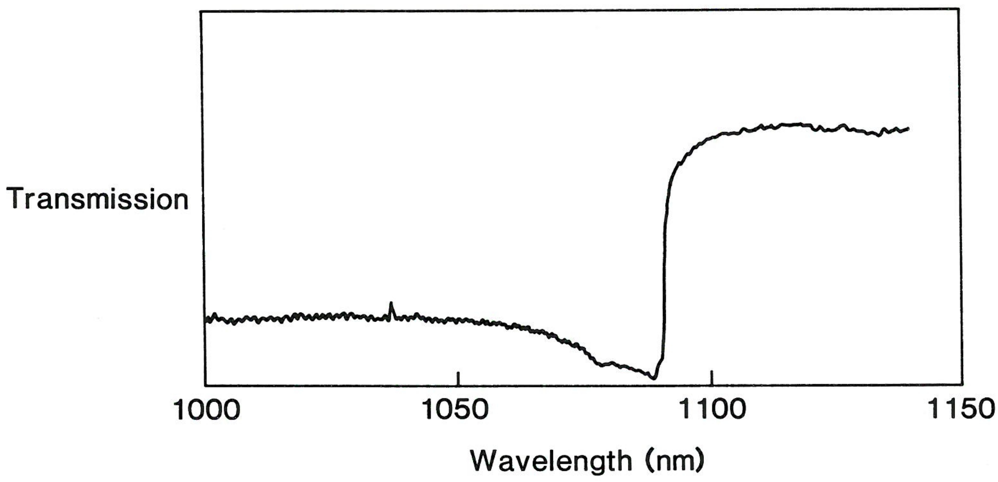

Figure 82. Experimental grating transmission spectrum for grating X3.

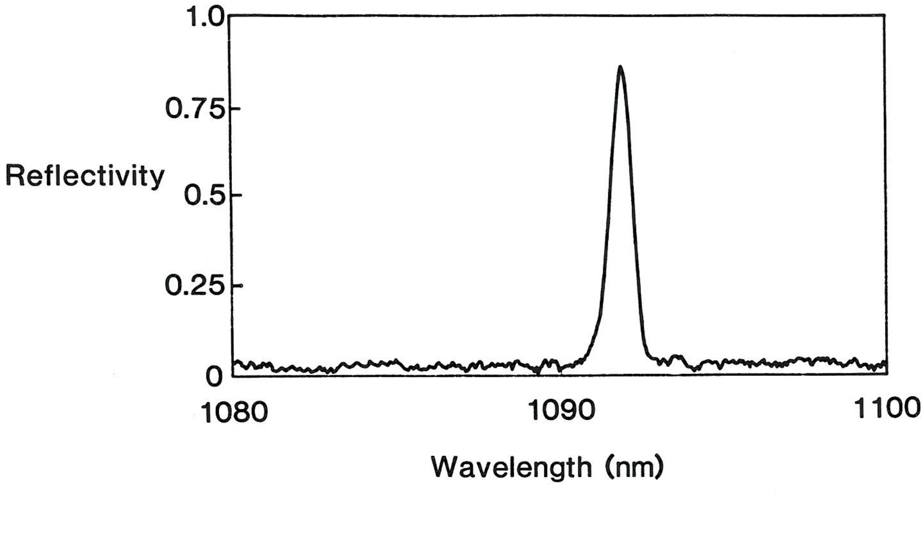

Figure 83. Experimental grating reflectivity spectrum for grating X3.

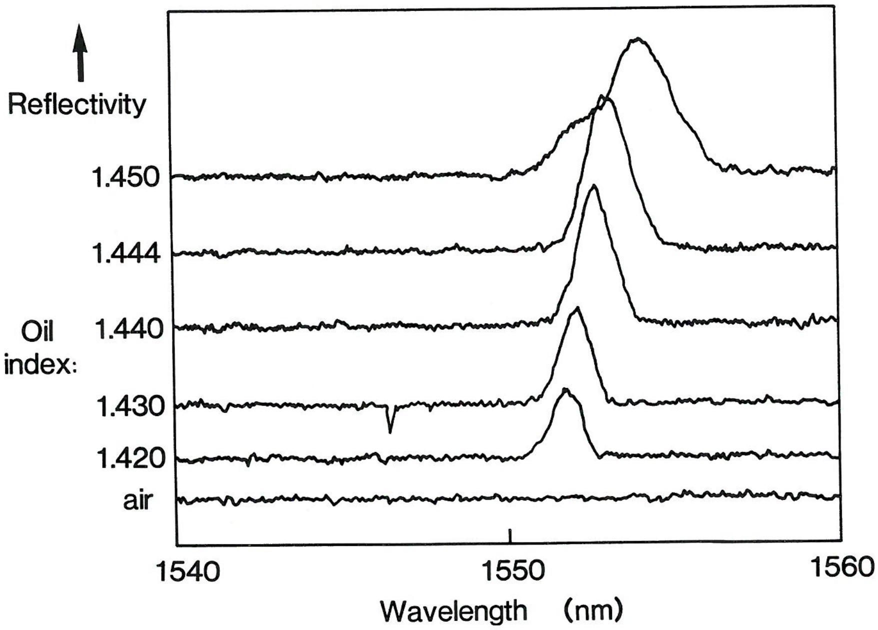

Figure 84. Experimental grating reflectivity spectra for various oils showing the effect of changing oil refractive index.

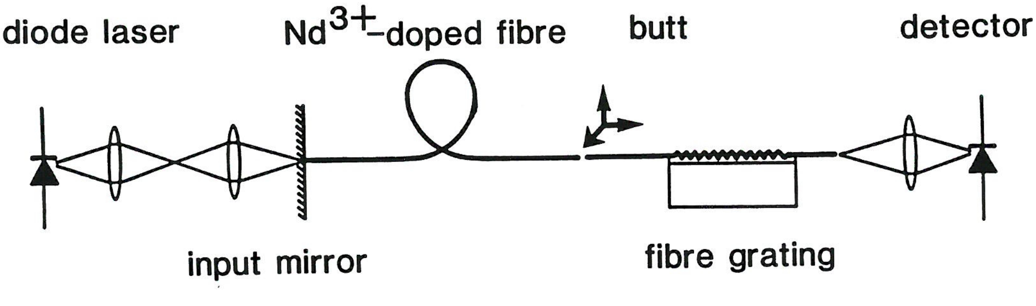

Figure 85. Experimental setup employed to incorporate fibre gratings into CW fibre lasers.

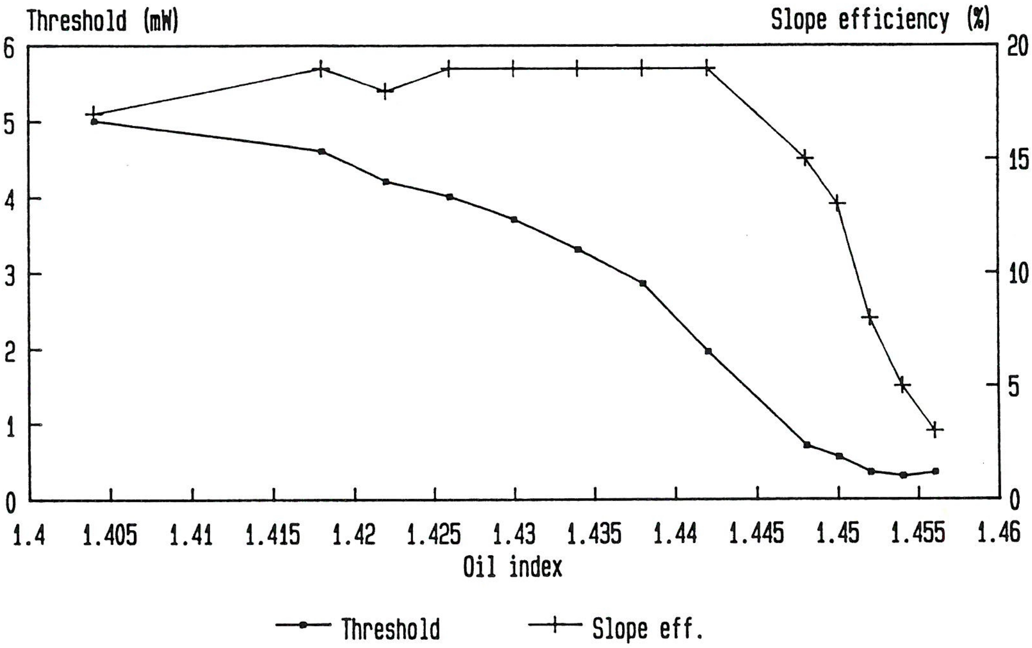

Figure 86. Experimental CW lasing threshold and slope efficiency for oils of various refractive indices, showing optimum output coupling.

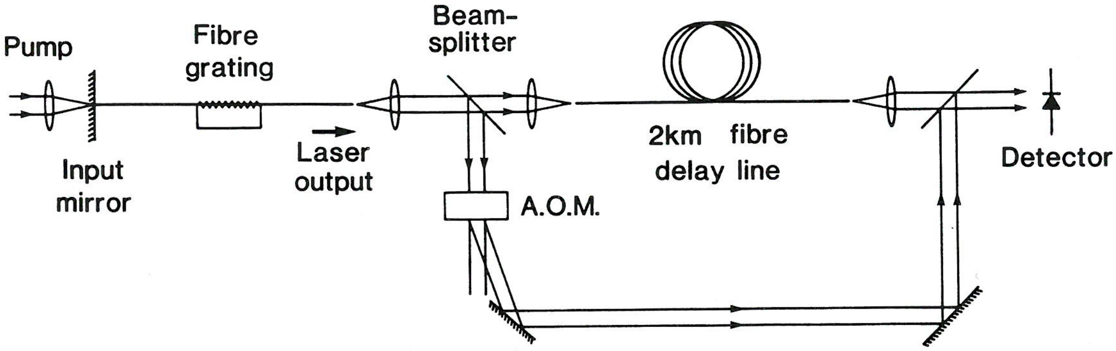

Figure 87. Experimental setup employed to achieve single longitudinal mode operation. Also shown is the self-heterodyne interferometer used to determine the fibre laser output bandwidth.

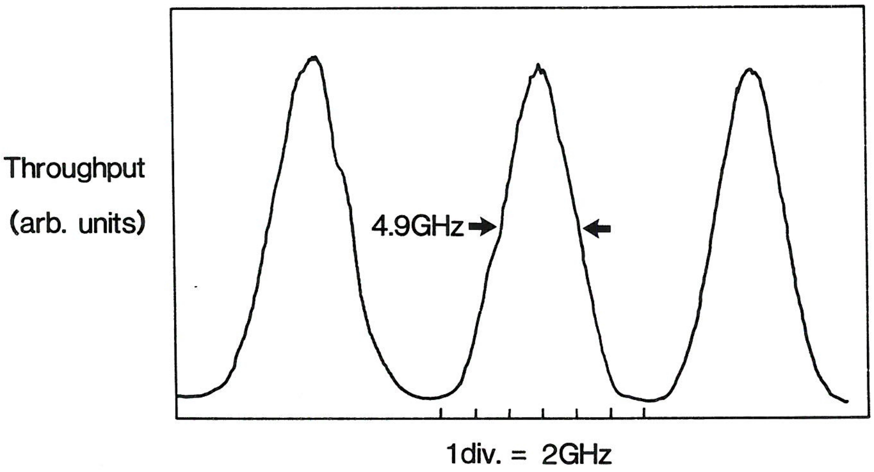

Figure 88. Scanning Fabry Perot traces showing output spectrum of narrow-linewidth fibre laser operating at 1550nm.

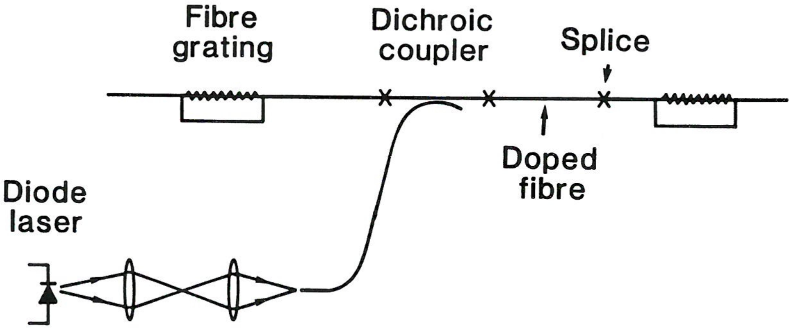

Figure 89. Experimental setup constructed to employ fibre gratings as both the input and output couplers.

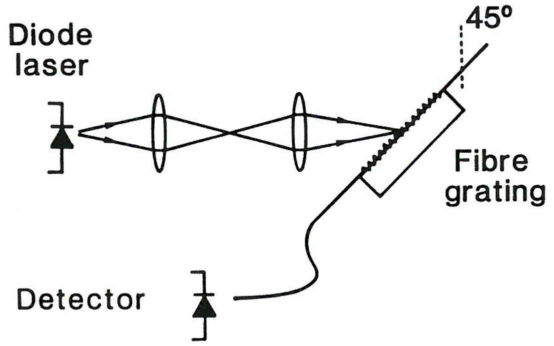

Figure 90. Experimental setup employed to launch pump light into a fibre grating.

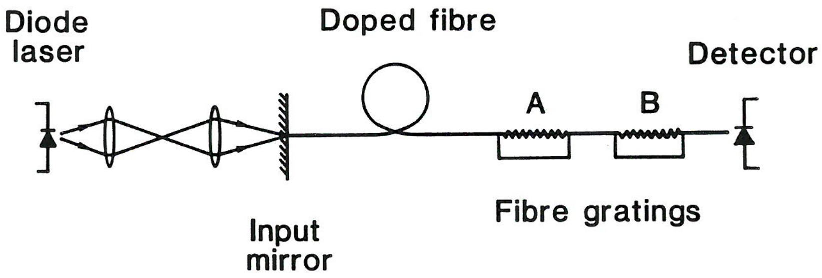

Figure 91. Experimental setup employed to achieve dual wavelength operation of a fibre laser.

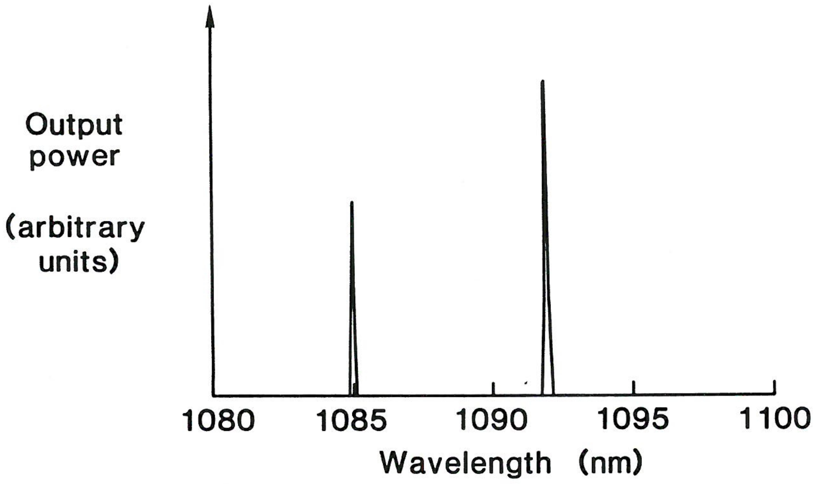

Figure 92. Output spectrum from dual wavelength fibre laser.

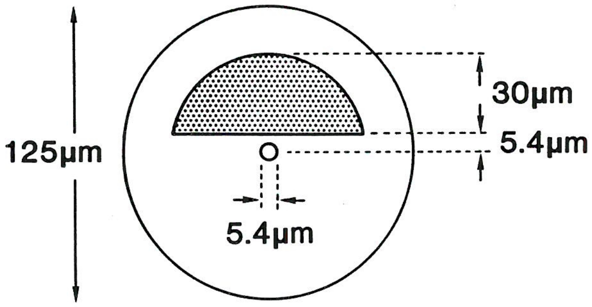

Figure 93. Dimensions of ideal D-fibre.

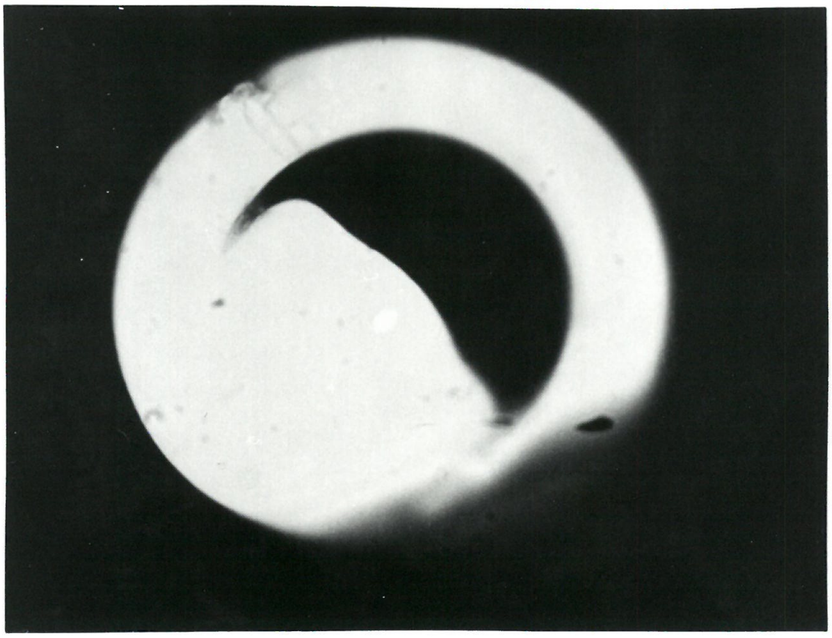

Fig.94 Photograph of brittle D-fibre showing stress centres.

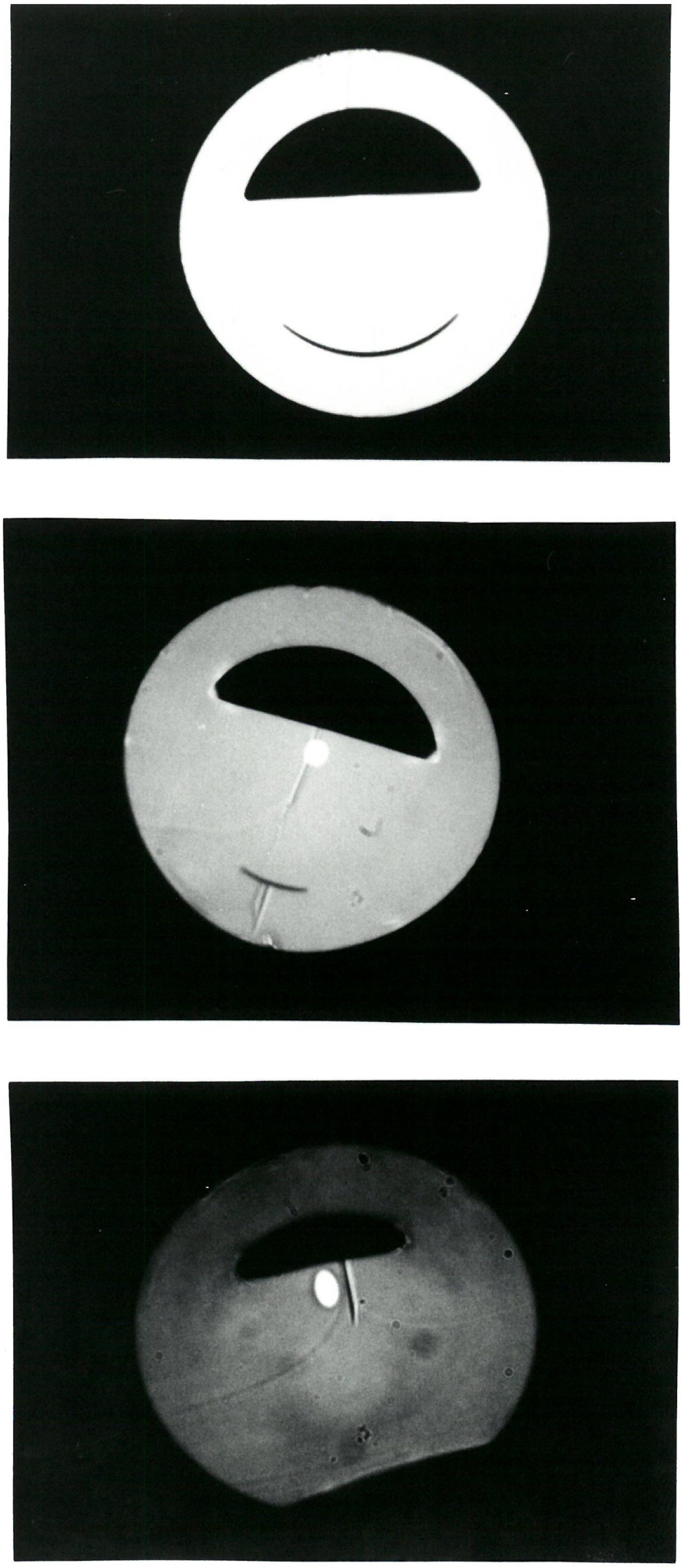

2000°C

2020°C

2050°C

Fig.95 Photographs of D-fibres pulled at various temperatures.

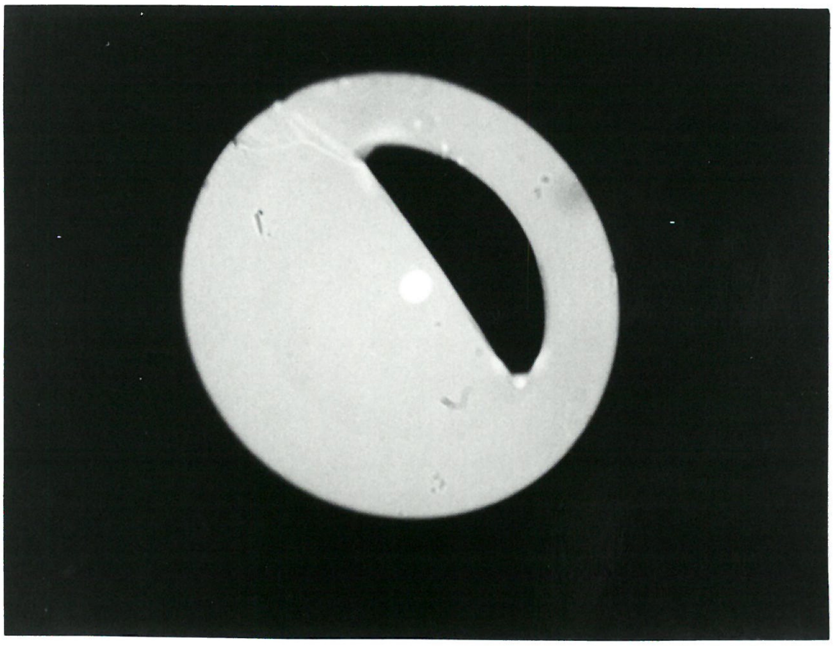

Fig.96   Photograph of successful D-fibre.

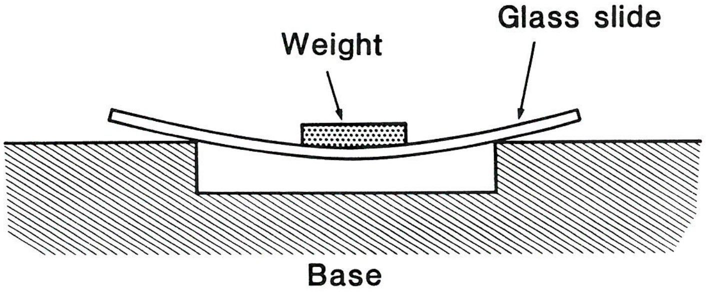

Figure 97. Experimental configuration of scheme employed to produce curved, grooved slides.

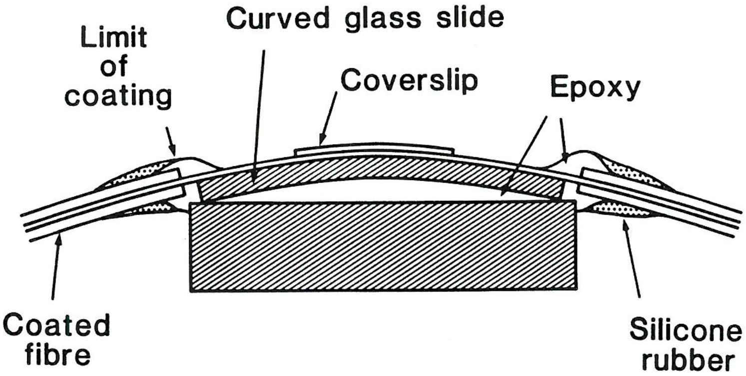

Figure 98. Structure of completed long interaction length grating.

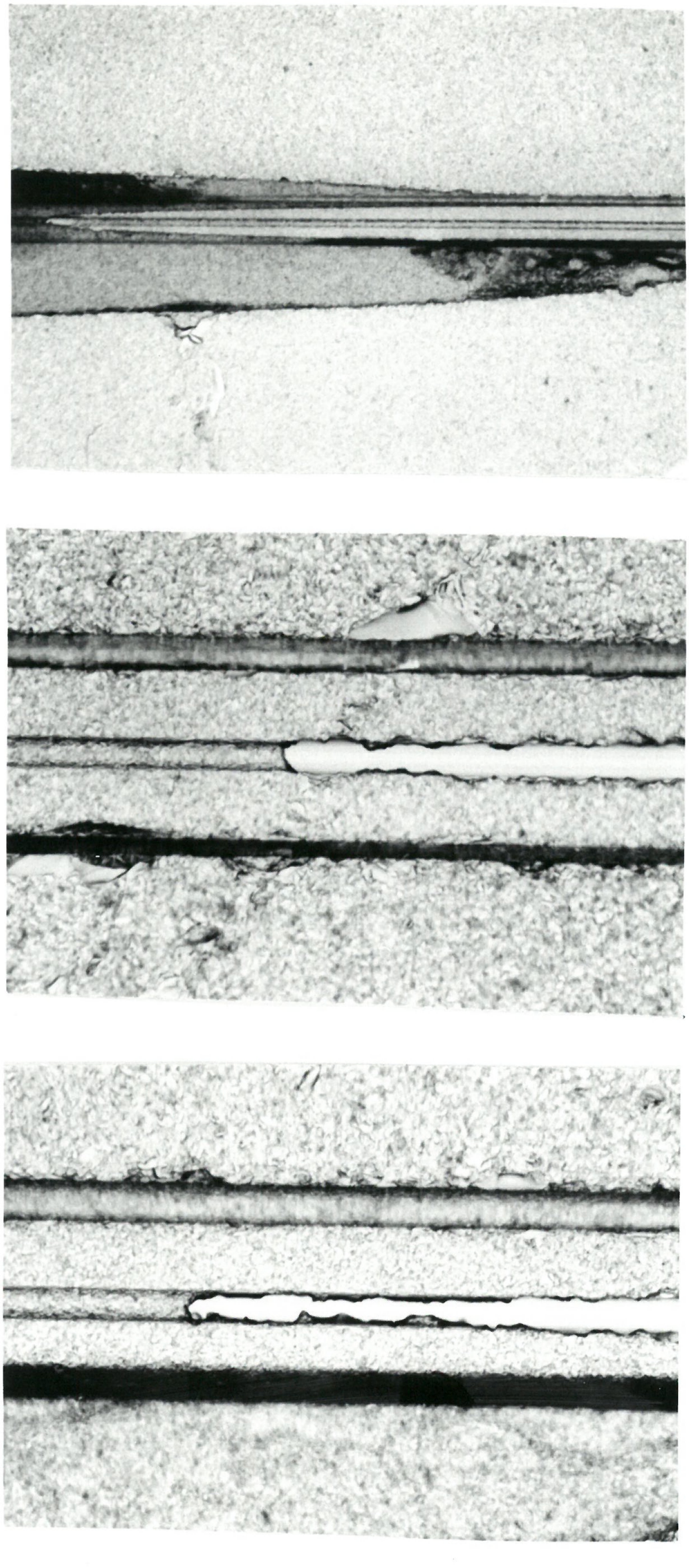

Fig.99 Photographs of end of uncovered region of D-fibre device.

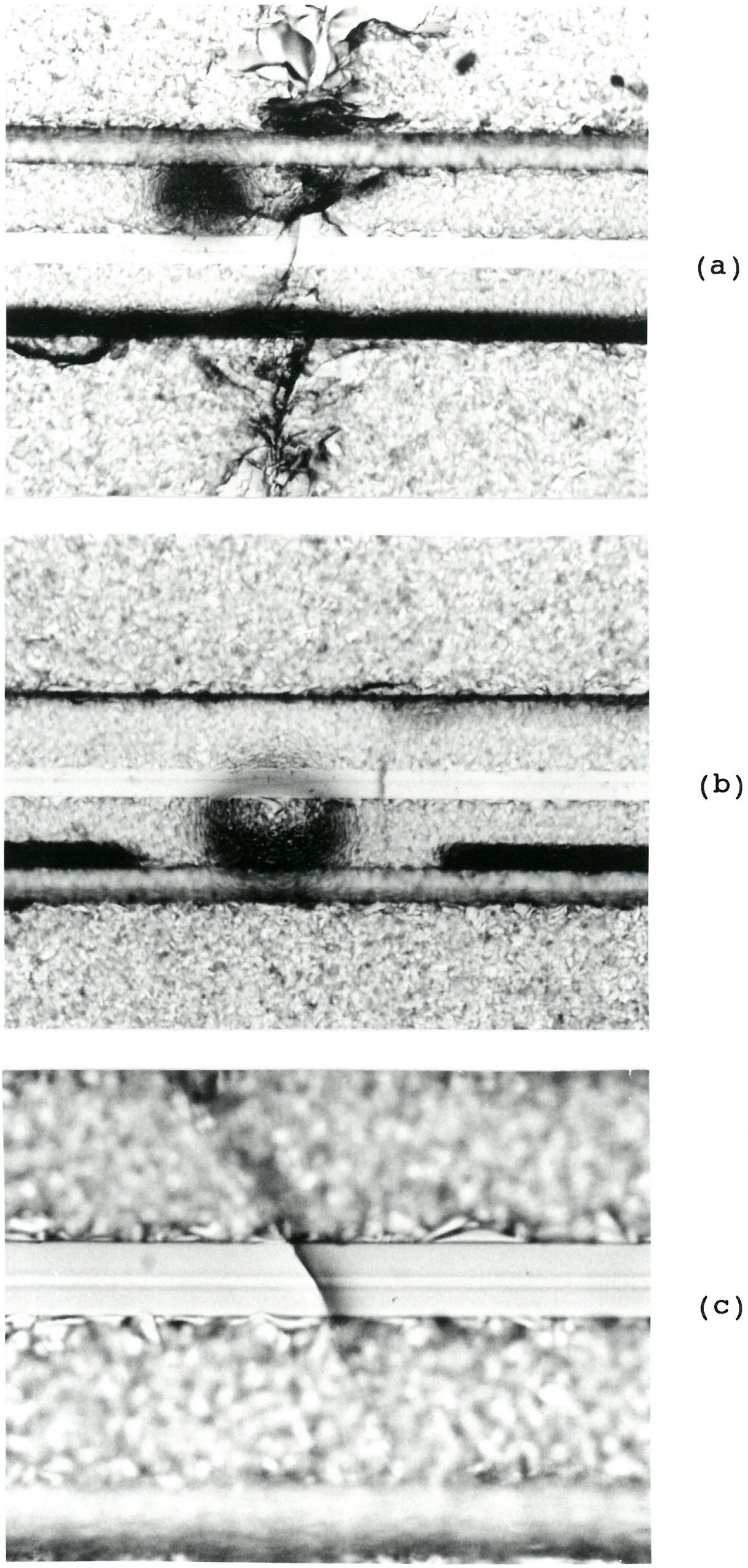

Fig.100 Photographs of breaks in D-fibre from various causes.

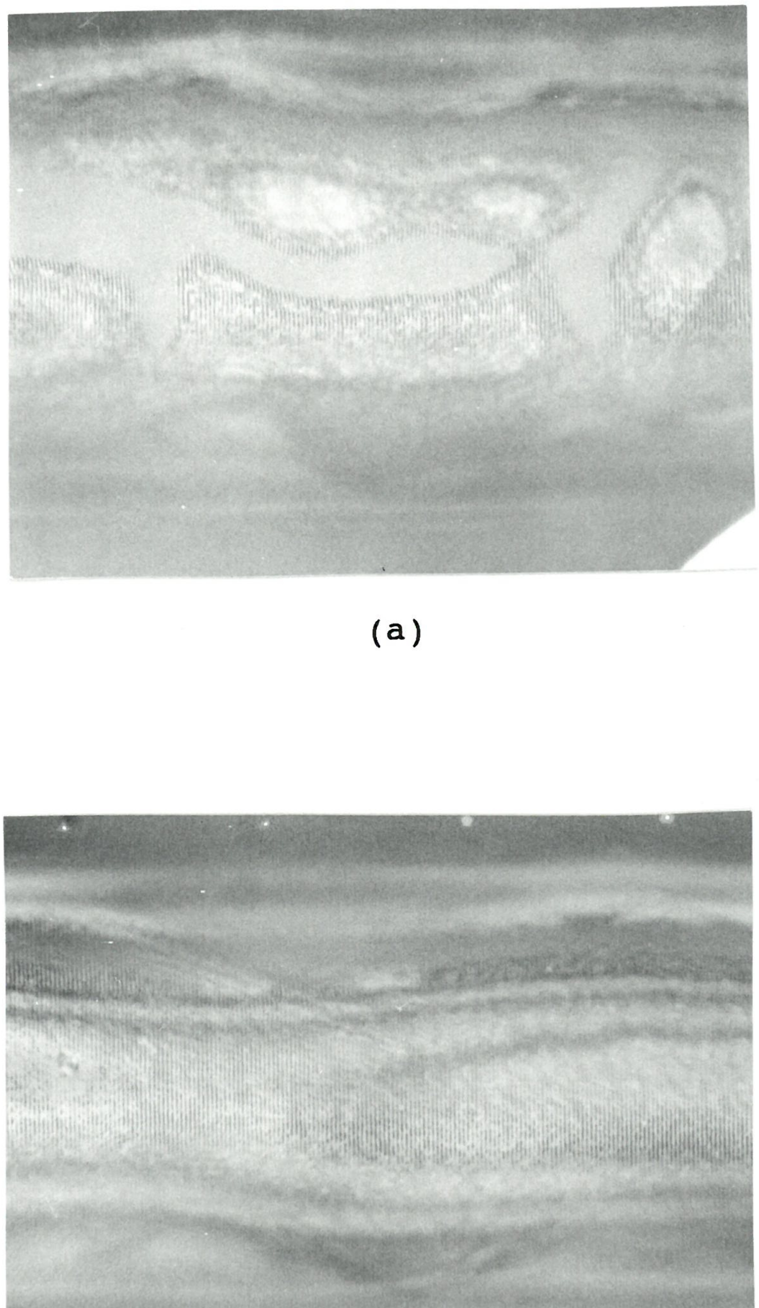

(a)

(b)

Fig.101 Photographs of resist patterns on D-fibre devices.

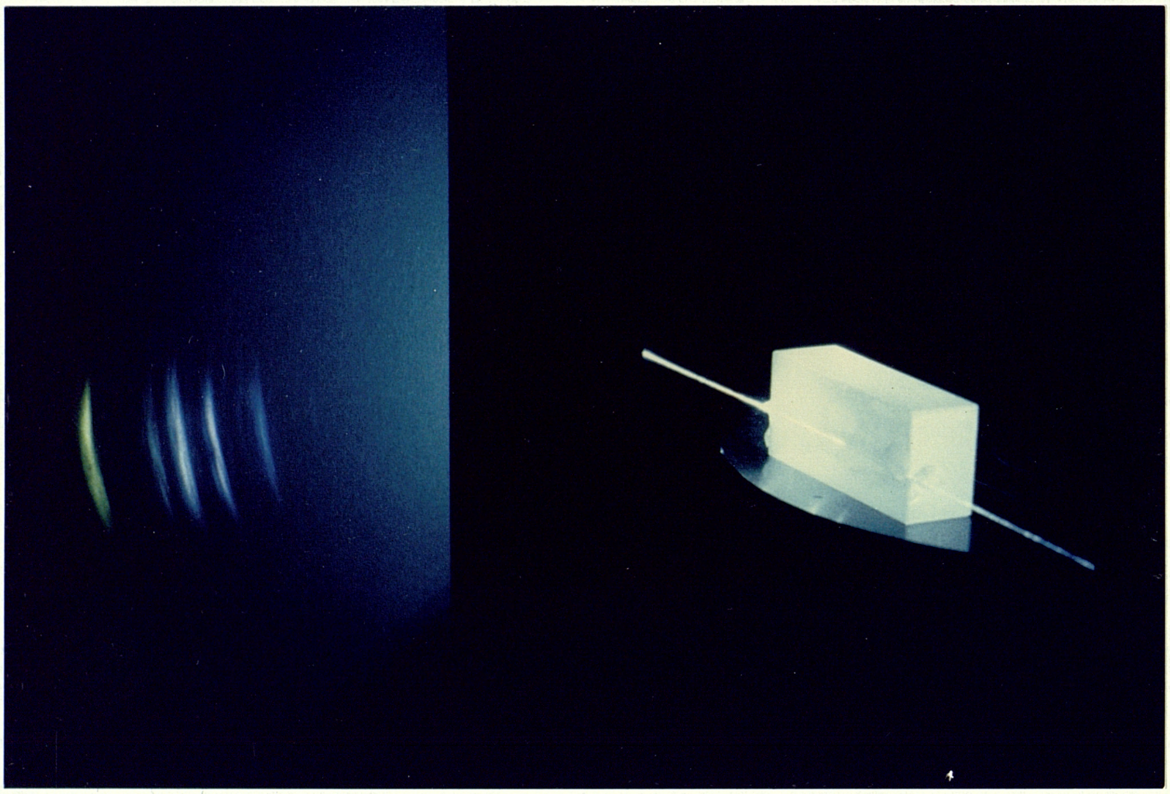

Figure 102. Photograph of D-fibre device with all lines argon-ion laser as pump source, showing spectrum splitting ability of device.